

EFFECTS OF PHOTON NOISE ON UNCONSTRAINED
MINIMIZATION TECHNIQUES FOR ITERATIVE
BLIND DECONVOLUTION

THESIS

Derek Kendall Davis
Captain, USAF

AFIT/GSO/ENP/94D-01

This document is approved
for release by the AFIT
Copyright 1994

DEPARTMENT OF THE AIR FORCE
AIR UNIVERSITY

AIR FORCE INSTITUTE OF TECHNOLOGY

Wright-Patterson Air Force Base, Ohio

19941228 024

AFIT/GSO/ENP/94D-01

EFFECTS OF PHOTON NOISE ON UNCONSTRAINED
MINIMIZATION TECHNIQUES FOR ITERATIVE
BLIND DECONVOLUTION

Accession For

NTIS OPA-AM ☒

DTIC TAB ☐

Unannounced ☐

Justification

Sig

Dist Number

A-1

THESIS

Derek Kendall Davis
Captain, USAF

AFIT/GSO/ENP/94D-01

DATE QUALITY INSPECTED 2

Approved for public release; distribution unlimited

AFIT/GSO/ENP/94D-01

EFFECTS OF PHOTON NOISE ON UNCONSTRAINED
MINIMIZATION TECHNIQUES FOR ITERATIVE
BLIND DECONVOLUTION

THESIS

Presented to the Faculty of the School of Engineering
of the Air Force Institute of Technology
Air University

In Partial Fulfillment of the
Requirements for the Degree of
Master of Science in Space Operations

Derek Kendall Davis, B.S.A.E.
Captain, USAF

December 1994

Approved for public release; distribution unlimited

Acknowledgements

I must begin by thanking Major Michael Roggemann and Dr. Byron Welsh for their patience in working with a former aeronautical engineer in a field requiring an electrical engineering or optical physics background. Hopefully, this thesis adequately reflects the countless hours Major Roggemann and Dr. Welsh dedicated to me and this effort. Special thanks must be given to Stuart Jefferies and Julian Christou for allowing the use of their Iterative Deconvolution Algorithm code in this thesis. They also provided many helpful hints via phone and electronic mail regarding the application of their program to this work. Thanks also to Dr. Yupu Chan for giving an Operations Research oriented perspective to this thesis.

In search of Isaac Newton's reference to "tremors in the atmosphere," I discovered I share a common goal with Sir Isaac Newton in my love for science. Isaac Newton concludes his book, *Optics*, with the following statement about "natural Philosophy" which we call "science."

And if natural Philosophy in all its Parts, by pursuing this Method, shall at length be perfected, the Bounds of Moral Philosophy will be also enlarged. For so far as we can know by natural Philosophy what is the first Cause, what Power He has over us, and Benefits we receive from Him, so far our Duty towards Him, as well as that towards one another, will appear to us by the Light of Nature (16).

I know the work I completed for this thesis has brought me to a better understanding of the creator of the universe. His absolute laws of nature reveal a more complete knowledge of His moral absolutes. It is only with His help that I finished this work.

Finally, I cannot say enough about my wife. Beth stuck with me all the way. She prayed for me, kept me in line when my priorities went awry, rejoiced me when things went well and encouraged with me when things did not. Thanks Honey, I'm on my way home.

Derek Kendall Davis

Table of Contents

	Page
Acknowledgements	ii
List of Figures	viii
List of Tables	xii
Abstract	xiii
I. Introduction	1-1
1.1 Motivation	1-1
1.2 Problem Statement	1-3
1.3 Approach	1-3
1.4 Scope	1-4
1.5 Summary of Key Results	1-5
1.6 Chapter Outlines	1-5
1.6.1 Chapter Two	1-6
1.6.2 Chapter Three	1-6
1.6.3 Chapter Four	1-6
1.6.4 Chapter Five	1-6
1.6.5 Appendix A	1-6
1.6.6 Appendix B	1-6
1.6.7 Appendix C	1-6
1.6.8 Appendix D	1-7
1.6.9 Appendix E	1-7

	Page
II. Background	2-1
2.1 Introduction	2-1
2.2 Atmospheric Turbulence	2-1
2.3 Adaptive Optics	2-3
2.4 Post-processing Techniques	2-4
2.5 Survey of Blind Deconvolution Techniques	2-5
2.5.1 Ayers-Dainty method	2-5
2.5.2 Maximum-likelihood estimation	2-9
2.5.3 Unconstrained Minimization	2-11
2.6 Summary	2-15
III. Methodology	3-1
3.1 Introduction	3-1
3.2 Terminology	3-1
3.2.1 Object	3-2
3.2.2 Point Spread Function (PSF)	3-2
3.2.3 Image	3-3
3.2.4 Positivity	3-3
3.2.5 Support	3-3
3.2.6 Error Metric	3-3
3.3 Computer Simulation of the Problem	3-4
3.4 Experimental Objectives	3-5
3.5 Constraint Driven Phenomena	3-6
3.5.1 Minimization	3-7
3.5.2 Image Error	3-7
3.5.3 Convolution Error	3-8
3.5.4 Band-Limit Error	3-8
3.6 Defining Comparison Metrics	3-9

	Page
3.7 Independent Variables	3-11
3.7.1 Objects and Image Measurements	3-11
3.7.2 Support Size	3-12
3.7.3 Average Photo Events, \bar{K}	3-12
3.8 Constants	3-15
3.8.1 Optical Transfer Function	3-15
3.8.2 Initial Guesses	3-15
3.9 Summary	3-16
IV. Results and Analysis	4-1
4.1 Introduction	4-1
4.2 Experiment One	4-1
4.2.1 Simulation Parameters	4-1
4.2.2 Simulation Results	4-3
4.2.3 Conclusions	4-7
4.3 Experiment Two	4-10
4.3.1 Simulation Parameters	4-11
4.3.2 Simulation Results	4-11
4.3.3 Conclusions	4-15
4.4 Experiment Three	4-18
4.4.1 Simulation Parameters	4-18
4.4.2 Simulation Results	4-21
4.4.3 Conclusions	4-21
4.5 Summary	4-25
V. Conclusion and Recommendations	5-1
5.1 Introduction	5-1
5.2 Conclusions	5-2
5.3 Recommendations for Further Research	5-3

	Page
Appendix A. Iterative Deconvolution Algorithm Tutorial	A-1
A.1 Introduction	A-1
A.2 How IDA works	A-1
A.3 Required Input	A-2
A.3.1 Convolution Image	A-2
A.3.2 Object Estimate	A-3
A.3.3 PSF Estimate	A-3
A.3.4 Object and PSF Support Arrays	A-3
A.3.5 Output Log File	A-3
A.3.6 Maximum Iterations	A-3
A.4 Available Options	A-4
A.4.1 Basic Lane Method	A-4
A.4.2 Band-limit Mask	A-4
A.4.3 Band-limit Error Term	A-5
A.4.4 Fourier Modulus Error	A-5
A.5 Modifications and Recompilation	A-6
A.5.1 Number of PSFs	A-6
A.5.2 Number of Pixels	A-6
A.5.3 Number of Variables	A-7
A.5.4 Tolerance	A-7
A.6 Summary	A-7
Appendix B. Simulated Images	B-1
B.1 True Objects and Noise-Free Images	B-1
B.2 True Point Spread Function	B-6
B.3 Photon Limited Images	B-7
Appendix C. Experiment 1 Results	C-1

	Page
Appendix D. Experiment 2 Results	D-1
Appendix E. Experiment 3 Results	E-1
Bibliography	BIB-1
Vita	VITA-1

List of Figures

Figure	Page
2.1. Ayers and Dainty Algorithm	2-6
3.1. Object Support Region	3-13
3.2. True Point Spread Function	3-16
4.1. Slice through the PSF	4-3
4.2. Noise-free Image D	4-4
4.3. Image D after Deconvolution	4-5
4.4. Exp 1: Image A Reconstructed Object Spectra	4-7
4.5. Exp 1: Image B Reconstructed Object Spectra	4-8
4.6. Exp 1: Image C Reconstructed Object Spectra	4-8
4.7. Exp 1: Image D Reconstructed Object Spectra	4-9
4.8. Exp 2: Image A: Band-limit mask vs. No mask	4-13
4.9. Exp 2: Image B: Band-limit mask vs. No mask	4-14
4.10. Exp 2: Image C: Band-limit mask vs. No mask	4-14
4.11. Exp 2: Image D: Band-limit mask vs. No mask	4-15
4.12. Exp 2: Photon noise results for Image A	4-16
4.13. Exp 2: Photon noise results for Image B	4-16
4.14. Exp 2: Photon noise results for Image C	4-17
4.15. Exp 2: Photon noise results for Image D	4-17
4.16. Exp 3: PSF estimate utilizing band-limit error term	4-20
4.17. Exp 3: Image B estimate utilizing band-limit error term	4-20
4.18. Exp 3: Image A object spectra with and without band-limit error	4-22
4.19. Exp 3: Image B object spectra with and without band-limit error	4-22
4.20. Exp 3: Image C object spectra with and without band-limit error	4-23

Figure	Page
4.21. Exp 3: Image D object spectra with and without band-limit error	4-23
B.1. Object A	B-2
B.2. Image A	B-2
B.3. Object B	B-3
B.4. Image B	B-3
B.5. Object C	B-4
B.6. Image C	B-4
B.7. Object D	B-5
B.8. Image D	B-5
B.9. True Point Spread Function	B-6
B.10. Image A with 100,000 photo events	B-7
B.11. Image A with 10,000 photo events	B-8
B.12. Image A with 5,000 photo events	B-8
B.13. Image B with 100,000 photo events	B-9
B.14. Image B with 10,000 photo events	B-9
B.15. Image B with 5,000 photo events	B-10
B.16. Image C with 100,000 photo events	B-10
B.17. Image C with 10,000 photo events	B-11
B.18. Image C with 5,000 photo events	B-11
B.19. Image D with 100,000 photo events	B-12
B.20. Image D with 10,000 photo events	B-12
B.21. Image D with 5,000 photo events	B-13
C.1. Object and PSF estimate for Image A, Support 1	C-2
C.2. Object and PSF estimate for Image A, Support 2	C-3
C.3. Object and PSF estimate for Image A, Support 3	C-4
C.4. Object and PSF estimate for Image B, Support 1	C-5

Figure	Page
C.5. Object and PSF estimate for Image B, Support 2	C-6
C.6. Object and PSF estimate for Image B, Support 3	C-7
C.7. Object and PSF estimate for Image C, Support 1	C-8
C.8. Object and PSF estimate for Image C, Support 2	C-9
C.9. Object and PSF estimate for Image C, Support 3	C-10
C.10. Object and PSF estimate for Image D, Support 1	C-11
C.11. Object and PSF estimate for Image D, Support 2	C-12
C.12. Object and PSF estimate for Image D, Support 3	C-13
D.1. Object estimate for Image A ($\bar{K} = 10^5$) using the Lane method .	D-2
D.2. Object estimate for Image A ($\bar{K} = 10^5$) using a band-limit mask	D-2
D.3. Object estimate for Image B ($\bar{K} = 10^5$) using the Lane method .	D-3
D.4. Object estimate for Image B ($\bar{K} = 10^5$) using a band-limit mask	D-3
D.5. Object estimate for Image C ($\bar{K} = 10^5$) using the Lane method .	D-4
D.6. Object estimate for Image C ($\bar{K} = 10^5$) using a band-limit mask	D-4
D.7. Object estimate for Image D ($\bar{K} = 10^5$) using the Lane method .	D-5
D.8. Object estimate for Image D ($\bar{K} = 10^5$) using a band-limit mask	D-5
D.9. PSF estimates for Images A and D ($\bar{K} = 10^5$) using a band-limit mask	D-6
D.10. Object estimate for Image A ($\bar{K} = 10^4$)	D-7
D.11. Object estimate for Image A ($\bar{K} = 5,000$)	D-7
D.12. Object estimate for Image B ($\bar{K} = 10^4$)	D-8
D.13. Object estimate for Image B ($\bar{K} = 5,000$)	D-8
D.14. Object estimate for Image C ($\bar{K} = 10^4$)	D-9
D.15. Object estimate for Image C ($\bar{K} = 5,000$)	D-9
D.16. Object estimate for Image D ($\bar{K} = 10^4$)	D-10
D.17. Object estimate for Image D ($\bar{K} = 5,000$)	D-10
E.1. Object estimate for Image A (noise-free)	E-2

Figure	Page
E.2. Object estimate for Image A ($\bar{K} = 10^5$)	E-2
E.3. Object estimate for Image A ($\bar{K} = 10^4$)	E-3
E.4. Object estimate for Image B (noise-free)	E-3
E.5. Object estimate for Image B ($\bar{K} = 10^5$)	E-4
E.6. Object estimate for Image B ($\bar{K} = 10^4$)	E-4
E.7. Object estimate for Image C (noise-free)	E-5
E.8. Object estimate for Image C ($\bar{K} = 10^5$)	E-5
E.9. Object estimate for Image C ($\bar{K} = 10^4$)	E-6
E.10. Object estimate for Image D (noise-free)	E-6
E.11. Object estimate for Image D ($\bar{K} = 10^5$)	E-7
E.12. Object estimate for Image D ($\bar{K} = 10^4$)	E-7

List of Tables

Table	Page
3.1. Photo events for Common Sky Objects	3-14
4.1. Experiment 1 Results Summary	4-6
4.2. Experiment 2 Results Summary	4-12
4.3. Experiment 3 Results Summary	4-24

Abstract

In recent years, imaging through atmospheric turbulence has interested military scientists seeking to improve optical surveillance of satellites for intelligence gathering purposes. Adaptive optics was a step toward achieving diffraction-limited resolution from ground-based telescopes. Unfortunately, adaptive optics only partially compensate for atmospheric blurring, therefore post-processing of images is required. Processing methods in use today require knowledge of the impulse response of the optical system to reconstruct imagery, but this information is seldom known. This thesis looks at a new method of processing compensated imagery, called blind deconvolution, which assumes very little or no *a priori* information about the impulse response. In particular, this investigation analyzes the performance of Lane's unconstrained minimization method of blind deconvolution as modified by Jefferies and Christou. The unconstrained minimization technique is applied to simulated single and binary star images corrupted by photon noise. Results reveal that prior knowledge of the cutoff frequency of the system greatly enhances the ability of the algorithm to achieve accurate estimates of the object when measurements contain relatively few photo events. Additionally, this study discovered that estimates are highly dependent upon the choice of the support region. Analysis also shows that the algorithm produces estimates containing frequency content above the diffraction-limit. The presence of this high-frequency information may invalidate this method as a useful means to reconstruct imagery.

EFFECTS OF PHOTON NOISE ON UNCONSTRAINED MINIMIZATION TECHNIQUES FOR ITERATIVE BLIND DECONVOLUTION

I. Introduction

1.1 Motivation

For centuries, scientists and philosophers alike have looked to the stars for numerous purposes: for meaning in life as well as a better understanding of our universe and our planet. The invention of the telescope permitted man a closer look at the stars, but many soon realized that the starlight they beheld was distorted by the atmosphere. Isaac Newton surmised in 1704 that better observations might be made on the peaks of high mountains to mitigate "the confusion of the rays which arises from tremors of the atmosphere" (16).

Today, the telescope has uses far beyond what Newton and his contemporaries dreamed. The launch of Sputnik in 1957 threw the United States into a flurry of activity to respond in kind while apprehension over the Soviet's ability to place an object in orbit created an entirely new endeavor—space surveillance. The Air Force met this new mission requirement by first employing the Baker-Nunn satellite tracking camera at five locations around the world (15). The Baker-Nunn camera used a modified Schmidt telescope with excellent resolution to photograph and identify objects in space. Since the early 1960's, the space surveillance mission has shifted from visual optics to radar which is not limited to operations at night. However, optical surveillance maintains a key role in accomplishing the space surveillance mission. The ground-based electro-optical deep space surveillance system (GEODSS) sensors are responsible for collecting over 65 percent of the tracking data for deep space ob-

jects (15). According to the Air Force's *Space Handbook*, space surveillance includes "the ability to surveil and monitor continuously all significant military activities in space" (15). Today, Air Force leaders not only want to know the satellite and its owner, but also what missions it performs and what equipment it carries. This requires much more resolution than current GEODSS telescopes or even phased-array radar can provide.

Research toward improving this resolution is accomplished at the U. S. Air Force Maui Optical Station (AMOS). AMOS houses one of the most advanced telescopes in the world for the purpose of imaging objects in space. It's 1.6 meter telescope obtains short-exposure, high resolution imagery through the use of an adaptive optics system. Since adaptive optics only partially compensates for the turbulence-induced aberrations, AMOS also relies on post-processing techniques to improve overall image quality (23).

Much work has gone into developing algorithms and techniques which can improve the quality of blurred images. Most techniques require an understanding of the impulse response, also called the point spread function (PSF), and some knowledge of the statistical nature of the noise inherent in the optical system. Adaptive optics images result from the actual object and the compensated PSF, which includes effects from atmospheric turbulence not corrected by the adaptive optics system. To alleviate the problem of the unknown PSF, one image processing method, blind deconvolution, makes successive guesses at both the object and point spread function such that they converge on the "true" object and PSF.

Blind deconvolution provides the ability to make estimates of both an object and a PSF without *a priori* knowledge of the blurring function. Though several papers have been written on the topic of blind deconvolution, the work completed by R. G. Lane (13) can most readily be applied to short exposure compensated imagery. The Lane method as modified by S. M. Jefferies and J. C. Christou allows for great flexibility since it makes estimates of both the object and the PSF given

any amount of information available on the impulse response—from no information to complete knowledge of the optical system (12).

Since the adaptive optics system at AMOS takes short-exposure images containing very little light, any post-processing technique must have the ability to reconstruct images in the presence of photon noise. Jefferies and Christou only addressed the issue of additive noise. Thus, before recommending this technique to the operational users on Maui, the question should be asked: How well does the unconstrained minimization algorithm perform for photon limited images?

1.2 Problem Statement

This thesis seeks to document the ability of the iterative deconvolution algorithm to reconstruct images in the presence of photon noise. The algorithm's performance is evaluated as a function of differing light levels and differing amounts of prior information concerning the blurring function and the noise.

1.3 Approach

To accomplish the task of evaluating the unconstrained minimization technique, several things were put in order. First, S. M. Jefferies and J. C. Christou gave permission to use their FORTRAN code which implements the unconstrained minimization technique through their iterative deconvolution algorithm (IDA) as discussed in their 1993 paper (12). Second, a model had to be developed which would isolate photon noise from all other noise and blurring effects. Finally, experimentation was designed around answering the following questions.

1. How can photon noise be modeled for computer simulation?
2. At what light level can IDA no longer improve the measured image?
3. Do the modifications made by Jefferies and Christou provide significant improvement over the Lane method for reconstructing photon limited imagery?

4. How can prior information regarding the point spread function's cutoff frequency best be utilized in the reconstruction?

As a result, computer simulation was selected as the best means of both creating photon limited images and testing the blind deconvolution algorithm.

1.4 Scope

This thesis seeks to simulate post-processing of images of exo-atmospheric objects obtained through an adaptive optics system and specifically analyze the effects of photon noise in the measured images. The single simulated images are limited to point sources of differing intensity and separation. These images are directly analogous to single and binary star images. Multiple or composite images and extended objects, such as satellites, are not addressed within this study.

Jefferies and Christou modified the Lane method by adding band-limit and Fourier modulus error terms to the objective function for minimization. Since the IDA code allows selective use of both of these error metrics, only the band-limit metric was tested. The following analysis does not include use of the Fourier modulus error metric, since its application requires Fourier modulus information obtained through speckle interferometry (13). One goal of this paper is to reveal the utility of pure blind deconvolution, thus as little additional information as possible is used in the reconstruction process.

Additionally, this thesis limits its scope to post-processing of detected images only. It does not discuss design of an adaptive optics system. Optical design issues such as properties of optical materials or detector array functions are not addressed here. Finally, this paper does not consider real-time processing of images nor does it specifically cite the computational hardware necessary to process images.

1.5 Summary of Key Results

Several results were obtained in this analysis which weigh heavily on the future study of this algorithm to process images of extended objects. Proof that the unconstrained minimization technique will work for extended objects is absolutely necessary before any proposal can be made regarding its operational use at AMOS. The key results obtained by this study are as follows:

1. Support size and shape greatly affect the reconstruction. Incorporating knowledge of the shape and especially the location of the first ring of the actual point spread function in the support arrays produces object estimates much closer to the "true" object.

2. Information regarding the diffraction-limited spatial frequency cutoff, or band-limit, of the measured image is necessary to reconstruct any photon limited image, even when the amount of light present is relatively high. Without the band-limit input, the noise in the measured image is multiplied in the estimates produced by IDA similar to noise effects in an inverse filter.

3. The IDA code performs well for very high light levels. As the light level is reduced, Poisson noise effects due to the random arrival of photo-events become so strong that single images at low light levels are almost impossible to restore correctly.

4. Unconstrained minimization techniques allow for the creation of information above the cutoff frequency—an attempt at super-resolution. The high frequency content in the estimated object spectrum and optical transfer function (OTF) leads one to question the validity of the iterative deconvolution algorithm, especially since the point spread function is band-limited due to the physical nature of the optics.

1.6 Chapter Outlines

A brief synopsis of the remainder of the thesis follows.

1.6.1 Chapter Two. Chapter 2 reviews some earlier work in the area of blind deconvolution and outlines the algorithm derived by Lane and modified by Jefferies and Christou.

1.6.2 Chapter Three. Chapter 3 lays down the terminology, the comparison metrics and the objectives which allow for computer simulation of the iterative deconvolution algorithm.

1.6.3 Chapter Four. Chapter 4 details three experiments designed to test the blind deconvolution technique and analyzes the results of the experimentation with the main focus on the effects of photon noise.

1.6.4 Chapter Five. Chapter 5 summarizes the important results uncovered throughout this thesis effort and concludes with recommendations for further study on extended objects.

1.6.5 Appendix A. Appendix A documents the iterative deconvolution algorithm (IDA) code as modified for this thesis. This appendix provides considerable detail on the use of the FORTRAN code provided by S. M. Jefferies and J. C. Christou which performs blind deconvolution through unconstrained minimization. Included in the appendix are the appropriate inputs used by the program and the proper format for the different data files. This appendix also contains some helpful hints regarding modification of the code for future study.

1.6.6 Appendix B. Appendix B contains a compilation of the simulated input images utilized in three experiments.

1.6.7 Appendix C. Appendix C consists of estimates produced by the Lane method in Experiment 1 for noise-free images.

1.6.8 Appendix D. Appendix D compiles the object estimates made during Experiment 2 for photon limited images using both the strict Lane method and the modified algorithm of Jefferies and Christou.

1.6.9 Appendix E. Appendix E lists the output estimates found in Experiment 3 utilizing the band-limit error term in unconstrained minimization.

II. Background

2.1 Introduction

This chapter presents the basic framework necessary to understand the fundamental problem of atmospheric turbulence, its relation to adaptive optics, and why post-processing of images is necessary after adaptive optics correction. In addition to the fundamentals of atmospheric imaging, background material is presented on a particular post-processing technique called blind deconvolution. After a brief survey of various blind deconvolution algorithms, this chapter concludes with a detailed look at the unconstrained minimization method derived by R. G. Lane and modified by S. M. Jefferies and J. C. Christou.

2.2 Atmospheric Turbulence

The resolution of images formed by large optical telescopes is directly attributable to atmospheric turbulence. According to the "turbulent eddy" model, this degradation is due to random inhomogeneities in the refractive index of air (8). Differential heating of the Earth's surface creates this phenomenon, producing large scale temperature gradients. Convection and turbulent wind flow break up these large scale inhomogeneities into smaller scale "eddies". Each turbulent eddy has a unique refractive index, which modulates the amplitude and phase of a propagating wavefront both temporally and spatially. Amplitude modulation results in scintillation as observed in the twinkling of stars, whereas phase modulation results in random image motion (known as tilt) and phase aberration. For the case of ground-based imaging of exo-atmospheric objects, the effects of phase modulation are generally more severe than amplitude modulation (5).

Astronomers concerned with the propagation of light waves through turbulence have developed various parameters for characterizing the severity of image degradation due to turbulence. Astronomers typically use such parameters to compare the

relative seeing quality of candidate sites for new observatories. One of the most convenient and widely used measures of seeing quality was introduced by Fried (6) and is denoted r_0 . It is defined as the effective diameter of a telescope for which the Strehl resolution of the telescope is equal to the Strehl resolution associated with the atmospheric optical transfer function (OTF) (18). r_0 is a function of the zenith angle of the path of propagation, the wavelength, and the turbulence strength (18). Since the effects of turbulence on optical propagation are random in nature, r_0 is also random. Typical values for r_0 at a good observatory range from 5 cm for moderately poor seeing to 20 cm for exceptional seeing (8). In addition to its practical use as a measure of relative seeing quality, r_0 is widely used in expressions for the atmospheric OTF (8). Since it acts as an effective telescope diameter, r_0 simplifies the form of the OTF, and aids in understanding the effect of the atmosphere relative to the true diameter of the optics.

Since the atmospheric turbulence changes randomly as a function of both time and space, no two images taken through the atmosphere can have the same atmospheric OTF unless they are imaged through the same part of the atmosphere at the exact same time. The usual method of modeling the imaging process is by assuming the process is linear and shift invariant (2). Given an object, $f(x, y)$, and a point spread function (PSF), $h(x, y)$, where (x, y) is a position vector locating an arbitrary point in image space, the measured image, $g(x, y)$, is given by

$$g(x, y) = f(x, y) * h(x, y), \quad (2.1)$$

and by the convolution theorem,

$$g(x, y) \leftrightarrow G(u, v) = F(u, v)H(u, v), \quad (2.2)$$

where "*" denotes the two-dimensional convolution of the two functions, the capital letters represent the Fourier transforms of the respective lowercase functions and the

" \leftrightarrow " identifies a Fourier transform pair. Points in Fourier space are given by the position vector (u, v) . Therefore,

$$f(x, y) \leftrightarrow F(u, v) = \int_{-\infty}^{+\infty} \int_{-\infty}^{+\infty} f(x, y) \exp[j2\pi(ux + vy)] dx dy, \quad (2.3)$$

where $F(u, v)$ represents the Fourier transform of $f(x, y)$.

If the object can be assumed to be stationary, then one only needs to determine under what conditions the PSF, $h(x, y)$, is shift invariant to have a linear, shift invariant system. Since the PSF is the inverse Fourier transform of the optical transfer function, $H(u, v)$, the PSF varies both spatially and temporally as well. To freeze the time-varying shift in the PSF or OTF, short-exposure images on the order of milli-seconds are required. To ensure shift invariance, each object must be viewed through a very small cone of the atmosphere. This small angle is known as the isoplanatic angle. Equation 2.1 above is valid only for short-exposures and when the object lies within the isoplanatic angle.

2.3 Adaptive Optics

Though atmospheric imaging requires short-exposures to be imaged through very small solid angles, real-time compensation of the random phase modulation due to turbulence can be achieved through the use of adaptive optics. To accomplish this, the adaptive optics system must measure these phase aberrations and compensate for them almost instantaneously using a deformable mirror. Determining the phase perturbation requires a wave-front sensor which observes a near-by natural star or a synthetic laser guide star (21). The wave-front sensor communicates the phase aberrations present in a particular isoplanatic region of the atmosphere at a specific time to the electronics which deform the mirror appropriately. In the AMOS system, a monolithic piezoelectric mirror (MPM) has 168 actuators which push or

pull on different locations around the mirror to correct for phase errors caused by atmospheric turbulence (19).

2.4 Post-processing Techniques

Unfortunately, residual phase errors still remain even after adaptive optics correction (21). Therefore, post-processing of images is required to correct for the effects of residual phase errors and to sharpen the image since high spatial frequency information is attenuated by the OTF. Sharpening of the image can be accomplished through deconvolution of the point spread function from the measured image. Quite often an ensemble of images are averaged and the average point spread function can be deconvolved from the average measured image (19). Roggemann [1992] uses both a modified inverse filter and a pseudo-Wiener filter to make estimates at an object spectrum given an ensemble of image measurements from an adaptive optics system (19).

Both methods discussed by Roggemann require some knowledge of the OTF and the noise present in the images. If $\langle G(u, v) \rangle$ represents the average spectrum of the measured images, then the object spectrum can be estimated by the inverse filter,

$$\tilde{F}(u, v) = \frac{\langle G(u, v) \rangle}{\tilde{H}(u, v)}, \quad (2.4)$$

and the pseudo-Wiener filter,

$$\tilde{F}(u, v) = \frac{\langle G(u, v) \rangle \tilde{H}^*(u, v)}{|\tilde{H}(u, v)|^2 + \left[\frac{\beta}{\text{SNR}(u, v)} \right]^2}, \quad (2.5)$$

where $\tilde{H}(u, v)$ is an estimate of the average compensated OTF, $\text{SNR}(u, v)$ is an estimate of the image spectrum signal-to-noise ratio and β is a parameter of choice (19). Errors in the object spectrum estimate, $\tilde{F}(u, v)$, occur any time $\tilde{H}(u, v)$, β , or $\text{SNR}(u, v)$ are not chosen exactly. Since $\tilde{H}(u, v)$ in particular is seldom known, new

techniques have recently been proposed which estimate both the object spectrum and the OTF.

2.5 *Survey of Blind Deconvolution Techniques*

T. G. Stockham coined the term "blind deconvolution" as signal or image recovery from a large collection of differently blurred versions of the same signal or image (22). It is interesting to note that one of Stockham's applications for blind deconvolution involved the hopeful recovery of pristine vocalizations of famous opera singers from old gramophone records (2). Today, blind deconvolution of imagery categorizes the techniques which seek to estimate an object's intensity directly, either from a single image or ensemble of images without prior knowledge of the PSF. Most techniques involve an iterative process which starts with an initial estimate at the object and PSF and converges toward the "true" object and PSF with each iteration. These methods require a vast amount of computer processing needing hundreds to thousands of iterations to complete.

The blind deconvolution problem has been approached several different ways. The first method involves an iterative process in which the object and PSF estimates are successively modified by certain image plane constraints. A second approach involves maximum-likelihood estimation using the expectation-maximization algorithm. The third method formulates the problem as an unconstrained minimization problem and uses a conjugate gradient minimization algorithm to iteratively determine the object and PSF. The proceeding sections briefly sketch each of the three approaches to the blind deconvolution problem.

2.5.1 *Ayers-Dainty method.* In 1988, G. R. Ayers and J. C. Dainty published the first paper containing a working blind deconvolution algorithm (1). The Ayers and Dainty technique, shown pictorially in Figure 2.1, requires an initial guess at the PSF and then utilizes an iterative method which subsequently constrains each

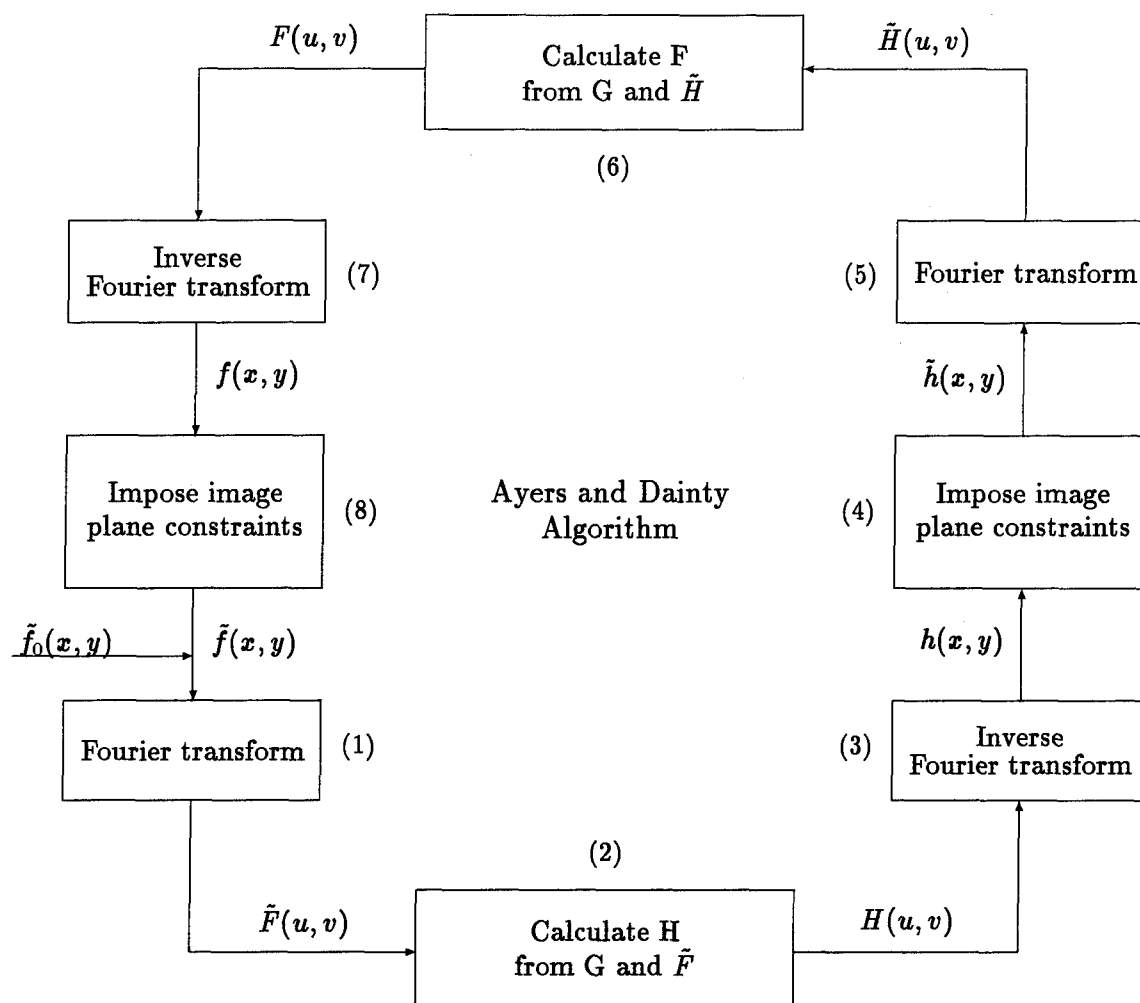


Figure 2.1 Ayers–Dainty blind deconvolution algorithm. Positivity is applied at steps 4 and 8 while the Fourier domain constraints are applied at steps 2 and 6.

object and PSF estimate in the image domain and the frequency domain. After an initial guess at the object, $\tilde{f}_0(x, y)$, is provided, the Ayers–Dainty algorithm performs the following eight steps iteratively.

1. Fourier transform the object estimate, $\tilde{f}(x, y)$, to obtain an object spectrum estimate, $\tilde{F}(u, v)$.

2. Form a new estimate of the OTF, $H(u, v)$, from the measured image spectrum, $G(u, v)$, and $\tilde{F}(u, v)$. Rather than apply a simple inverse filter, the Ayers–Dainty approach applies a Fourier domain constraint. This constraint ensures the product of both \tilde{F} and H equal G while preventing small errors in G from resulting in large errors in H where \tilde{F} is extremely small. Also, the Fourier domain constraint forms a weighted average of the previous estimate of the OTF and the inverse filtered estimate, G/\tilde{F} . The Fourier constraint applied in the Ayers–Dainty algorithm is summarized below.

If $|G(u, v)| < \text{noise level}$,

$$H_{i+1}(u, v) = \tilde{H}_i(u, v); \quad (2.6)$$

if $|\tilde{F}(u, v)| \geq |G(u, v)|$,

$$H_{i+1}(u, v) = (1 - \beta)\tilde{H}_i(u, v) + \beta \frac{G(u, v)}{\tilde{F}(u, v)}; \quad (2.7)$$

if $|\tilde{F}(u, v)| < |G(u, v)|$,

$$\frac{1}{H_{i+1}(u, v)} = \frac{(1 - \beta)}{\tilde{H}_i(u, v)} + \beta \frac{\tilde{F}(u, v)}{G(u, v)}, \quad (2.8)$$

where $0 \leq \beta \leq 1$ and β is set before algorithm is run and i and $i + 1$ represent the current iteration and next iteration, respectively.

3. Inverse Fourier transform the OTF estimate, $H(u, v)$, to obtain a PSF estimate, $h(x, y)$.

4. Impose image plane constraints on $h(x, y)$ to obtain $\tilde{h}(x, y)$. This image plane constraint forces every pixel within the estimate to be positive by setting each negative pixel to zero. The algorithm checks every pixel value at each iteration. The algorithm keeps track of the energy, or negative values, removed by summing their absolute values. Then the algorithm equally redistributes the removed energy to all pixels in the PSF estimate.

5. Fourier transform the constrained PSF estimate, $\tilde{h}(x, y)$, to obtain an OTF estimate, $\tilde{H}(u, v)$.

6. Impose the same Fourier domain constraints listed in step 2 to determine a new value for the object spectrum, $F(u, v)$, by replacing H with F and *visa versa*.

7. Inverse Fourier transform the object spectrum estimate, $F(u, v)$, to obtain an object estimate, $f(x, y)$.

8. Impose the positivity constraint on $f(x, y)$ to obtain a new object estimate, $\tilde{f}(x, y)$. If the new object estimate is not adequate, then return to step 1.

The Ayers-Dainty approach works well for images without noise corruption. However, the method requires further refinement in order to accommodate contaminated or complex images. In 1989, B. L. K. Davey, R. G. Lane, and R. H. T. Bates modified the Ayers-Dainty technique to handle small amounts of noise in the image by implementing a Wiener filter in the Fourier domain constraint to obtain each consecutive estimate of the object spectrum and the optical transfer function. In the image domain, Davey, *et al.* apply a support constraint in addition to positivity. The support constraint restricts the object and PSF estimate pixels to zero outside a specified region. This method requires the input of a binary mask which gives the extent of the object and another mask containing known extent of the PSF (4). Davey's modification of Ayers-Dainty revealed that blind deconvolution was possible for images corrupted by random additive noise.

Another modification to the Davey approach by Miura handles multiple speckle images of the same object (14). Each individual image, $g_n(x, y)$ can be modeled in the following way

$$g_n(x, y) = f(x, y) * h_n(x, y), \quad (2.9)$$

where $h_n(x, y)$ represents the n th instantaneous PSF and the asterisk, “*”, denotes two-dimensional convolution. The Miura algorithm performs blind deconvolution on each speckle image and averages the resulting object estimates after each iteration to obtain a single object estimate in which to start the next iteration. This algorithm combines the relative simplicity of the Ayers–Dainty approach with noise variance reduction through multiple image averaging. This modification to Ayers–Dainty reduces the number of iterations required while restoring noisy speckled images.

The Ayers–Dainty technique and the modifications outlined above proved that blind deconvolution was indeed possible. Unfortunately, they all had a serious drawback. Though they worked well on simulated data where the “true” object and PSF were known, none of the methods outlined above converge on the object and PSF either in a mean squared error sense or visually at consecutive iterations (13). In other words, if ϵ_n^2 represents the mean squared error at the n th iteration, then the error at a subsequent iteration is not necessarily less than the current error. Therefore, the following is possible,

$$\epsilon_{n+1}^2 > \epsilon_n^2, \quad (2.10)$$

where ϵ_{n+1}^2 contains the error at the next iteration. Two methods have been developed which converge on either a maximum or minimum point; theoretically providing better estimates with increasing iterations and improved stopping criteria for the iterative blind deconvolution process.

2.5.2 Maximum-likelihood estimation. One method has been suggested which performs iterative blind deconvolution with improved convergence properties. The goal of the maximum-likelihood estimation (MLE) technique is to find the object

intensity and the point spread function(s) that most likely created the measured data (21). T. J. Holmes recognized the need to deconvolve a signal without knowing the impulse response for confocal fluorescence microscopic imagery (11). Holmes sought to use MLE as a quantitative optimization criterion to solve the blind deconvolution problem of quantum-limited incoherent imagery.

In order to utilize the iterative method of MLE, Holmes derives a log-likelihood function to include the total photon count and the current object and PSF estimate. Each successive iteration produces a new estimate of both the object and PSF which monotonically increases the log-likelihood function. Holmes proved that since the MLE method treated the object and PSF arrays as probability density functions, each estimate was implicitly constrained to be non-negative and retain unit-volume (11). Unfortunately, the simple unconstrained MLE process did not produce any results resembling the true object and PSF. Holmes had to apply an external constraint to the iterative process.

As the first constraint, Holmes required that the impulse response estimate remain radially symmetric at every iteration since the PSF for many optical systems is symmetric. Outstanding results were obtained using the radial symmetry constraint on simulated images blurred with a circular PSF and corrupted by photon noise. As Holmes states, the drawback to the radial symmetry constraint is that the trivial solution (where the PSF becomes a delta function and the object estimate becomes the measured image) will eventually be reached given enough iterations (11).

To prevent the trivial solution, Holmes tried restricting the bandwidth of the PSF to the cutoff frequency of the optical system. At each iteration of the MLE method, this constraint extinguishes all information in the OTF estimate above a cutoff frequency determined by the optics, then inverse Fourier transforms the OTF to obtain the PSF, and sets all negative values in the PSF to zero before returning the new PSF back for the next iteration. This constraint produced outstanding results in conjunction with MLE for restoring photon-limited images. However, even though

the log-likelihood function increased monotonically using this method, a point was reached when the object and PSF estimates began to diverge from the true object and PSF (11). Thus, Holmes method has no guaranteed stopping criteria which present the best estimate of both object and PSF.

T. J. Schulz applied Holmes' maximum-likelihood estimation method to reconstruct a series of short-exposure images taken through atmospheric turbulence without the aide of a nearby point source or any knowledge of the atmospheric point spread functions (21). Schulz modified Holmes' MLE method for photon-limited images by extending the iterative process to handle a series of images of the same object. Noting that atmospheric PSFs have neither radial symmetry nor a unique band-limit, Schulz suggested two different modifications to the MLE method to overcome the problem of convergence on the trivial solution. One method utilizes a penalized maximum-likelihood function, while the other method is based on the parameterization of the PSFs by phase errors distributed over an aperture (21). Excellent results were obtained using simulated and actual photon-limited data. However, no information was given concerning the stopping criteria for the algorithm or whether the object and PSF estimates reached an optimal point then diverged from the true object and PSF.

2.5.3 Unconstrained Minimization. R. G. Lane addressed the blind deconvolution problem another way. Lane noted that the Ayers-Dainty approach "lacked stable convergence properties." By minimizing an error metric which included both the object and PSF estimate, he modeled blind deconvolution as an unconstrained minimization problem. Based on a steepest-descent search, Lane's algorithm handles additive noise and has well-defined stopping criteria (13).

Lane's method defines an error metric which quantifies how much the current estimate violates known constraints. The constraints applied in this method are similar to those used in previously mentioned blind deconvolution techniques—namely

positivity and convolution. Additionally, Lane utilizes a support constraint in image space which restricts the extent of the object and PSF estimates. The combined error function minimized in this method is shown below,

$$E_c = E_i + E_f, \quad (2.11)$$

where E_i and E_f represent the errors in the image domain and Fourier domain, respectively. With γ_f and γ_h denoting the points where $f(x, y)$ and $h(x, y)$ respectively violate their image plane constraints, Lane defines E_i as

$$E_i = \iint_{\gamma_f} |f(x, y)|^2 dx dy + \iint_{\gamma_h} |h(x, y)|^2 dx dy. \quad (2.12)$$

E_f quantifies the error in the convolution of the two estimates with respect to the measured image. E_f is given by

$$E_f = \iint |G(u, v) - F(u, v)H(u, v)|^2 du dv, \quad (2.13)$$

where $F(u, v)$ and $H(u, v)$ are the Fourier transforms of the object and PSF estimates, respectively (13).

Minimization of the combined error function is accomplished through a conjugate gradient minimization routine. The routine requires no additional constraints apart from the objective function itself. Thus, the Lane method models an unconstrained minimization problem where the pixels in the object and PSF represent the independent variables of the objective function to be minimized. The fact that this technique does not use an inverse filter to calculate either the object or PSF estimate is one of its strong points, since it is not overly sensitive when either of the convolutional components is close to zero. Another advantage of conjugate gradient minimization is that the objective function value monotonically decreases with each iteration until a local minimum is found.

The addition of a support constraint serves to prevent the occurrence of the trivial solution where $f(x, y)$ is exactly $g(x, y)$ and the PSF, $h(x, y)$, is an impulse function, $\delta(0, 0)$. Constraining the object estimate to have non-zero values in a region smaller than the array size ensures that the trivial solution has some error associated with it. Noise in the imaging process can be modeled in the following manner,

$$g(x, y) = f(x, y) * h(x, y) + c(x, y), \quad (2.14)$$

where the term, $c(x, y)$, represents additive noise. Without the support constraint, the trivial solution,

$$g(x, y) = g(x, y) * \delta(0, 0), \quad (2.15)$$

represents the global minimum to Equation 2.14 above.

Lane obtained excellent results using his method in the presence of Gaussian and Poisson noise for simulated images using the unconstrained minimization method from several different initial estimates. One problem the Lane method has is the relatively high probability of finding a local minimum instead of the global minimum depending on the initial estimates (13).

S. M. Jefferies and J. C. Christou modified the Lane algorithm (12). The Jefferies and Christou model includes not only the positivity, convolution and support constraints utilized by previous blind deconvolution algorithms but also applies band-limit, multiple image and Fourier modulus constraints. Jefferies and Christou claim their unconstrained minimization technique achieves "super-resolution" for continuous gray-scale images and low signal-to-noise ratio images by incorporating as much *a priori* information as possible in their algorithm.

The modification of the Lane algorithm seeks to minimize an error function with four terms instead of two. The error function, ϵ , is defined as

$$\epsilon \equiv E_i + E_f + E_{bl} + E_{Fm}, \quad (2.16)$$

where the four terms each represent an error defined by the current estimate of the object and PSF. The image domain error is exactly the same as Equation 2.12 in the Lane method. The convolution error,

$$E_f = \frac{1}{N^2} \iint |G(u, v) - F(u, v)H(u, v)|^2 B(u, v) du dv, \quad (2.17)$$

appears similar to Equation 2.13 with one additional term containing a low pass filter, $B(u, v)$, which eliminates the high-spatial frequency content of the noise present in the measurement. Thus, the object and PSF are loosely constrained to convolving to a low pass filtered version of the measured image, since no information is passed by the pupil for spatial frequencies greater than the cutoff frequency, D/λ , where D is the telescope diameter and λ is the optical wavelength.

The band-limit error term, E_{bl} , is utilized for the first few iterations when the trivial solution continually appears using only the first two error terms, then convergence is obtained using the image domain and convolution errors. The band-limit error,

$$E_{bl} = \frac{1}{N^2} \iint |H(u, v)|^2 B'(u, v) du dv, \quad (2.18)$$

contains a high pass filter, $B'(u, v)$, which acts to sum all frequency information in the OTF outside the cutoff frequency. Minimizing the high-frequency information in the PSF estimate ensures that the trivial solution will not be attained. Since this error metric forces high spatial frequency noise into the object estimate, it has to be relaxed before convergence.

The Fourier modulus error, E_{Fm} , utilizes Fourier modulus information obtained through speckle interferometry to constrain the estimate of the object spectrum to very near the true object spectrum modulus. As expected, this constraint proves to be a powerful tool in extracting an estimate very close to the true object from noisy data as long as the Fourier modulus information is available. When the Fourier modulus error is used, the noise in the convolution images mainly manifests itself in

the reconstructed PSF leaving an object estimate almost void of noise. See Jefferies and Christou (12) for more detailed information regarding the Fourier modulus error.

Few results were obtained using the modified Lane method without the Fourier modulus error. Those shown were compared against the excellent estimates made with the Fourier modulus error. Jefferies and Christou performed their analysis on images corrupted by zero-mean Gaussian noise. What remains to be asked are the following:

1. Can the addition of band-limit information to Lane's blind deconvolution technique perform well in the presence of photon noise?
2. Can this method be effectively used on compensated imagery from an adaptive optics system?
3. Since neither Lane nor Jefferies and Christou discuss the support constraint in detail, how does varying the support region affect the restoration of images?

2.6 Summary

This chapter reviewed fundamentals of imaging through atmospheric turbulence and presented a brief explanation of adaptive optics. Since imagery from adaptive optics still requires post-processing, the method of blind deconvolution was reviewed explicitly. Blind deconvolution involves restoration of an image or a series of images without prior knowledge of the blurring function or PSF. The Ayers-Dainty approach was the first workable algorithm toward solving the blind deconvolution problem. Due to the inability of Ayers-Dainty to converge on a "best" estimate, two other methods have been proposed. Maximum-likelihood estimation uses an iterative method which increases the likelihood that the object and PSF correctly estimate the "true" object and PSF. Results from Holmes, however, reveal that the maximum-likelihood estimation reaches an optimal estimate then diverges from the "true" object and PSF with further iterations. Lane proposed an unconstrained minimization solution to the blind deconvolution problem. Constraints are effec-

tively modeled in an error function which can be minimized through the conjugate gradient method. Further modifications to the Lane method developed by Jefferies and Christou are worthy of continued analysis. Chapter 3 discusses the modified Lane technique for experimentation on the effects of support size and photon noise on image restoration.

III. Methodology

3.1 Introduction

This chapter transitions from a basic understanding of the unconstrained minimization technique for blind deconvolution to its implementation on simulated images. In order to fully understand the approach taken, the notation for several terms are defined followed by a defense for computer simulation of this problem. The latter part of the chapter includes several key factors in the development of experimentation to analyze the Jefferies and Christou modification to the Lane method called the iterative deconvolution algorithm (IDA). First, the goals of subsequent experimentation and testing are listed. Then, a discussion of how the functions affecting the blind deconvolution algorithm is presented followed by a discussion of an error metric utilized in the comparison of different results. Finally, a listing of the variables affecting the blind deconvolution process emphasizes which ones will be altered and which ones will remain constant for the purposes of experimentation.

3.2 Terminology

As alluded to in the previous chapter, imaging is modeled as a linear, shift invariant process with the following form:

$$g(x, y) = f(x, y) * h(x, y), \quad (3.1)$$

where (x, y) represents an arbitrary point in the image domain, "*" denotes the two-dimensional convolution of the "true" object, $f(x, y)$, and the point spread function (PSF), $h(x, y)$, and $g(x, y)$ defines the measured image. Departures from the ideal convolution include noise inherent in the imaging process and assorted non-linearities (2). For short-exposure images, photon noise manifests itself in the random arrival of photons at the detector. All of these departures can be added to Equation 3.1 in

the form of a single contamination term. A new mathematical model of the imaging process follows,

$$g(x, y) = f(x, y) * h(x, y) + c(x, y), \quad (3.2)$$

where $c(x, y)$ represents the contamination term. The problem of blind deconvolution is to determine $f(x, y)$ given only the measured image, $g(x, y)$, and very little information about $h(x, y)$ and $c(x, y)$. Subsequent sections discuss each of the terms in the imaging process and how they relate to IDA using the unconstrained minimization approach.

3.2.1 Object. Obtaining a close representation of the "object" is the goal of any imaging process, though the object itself can never be fully realized. Even when one is close enough to observe an object with the unaided eye, the optical qualities of the human visual system, like the finite extent of the pupil, distort the actual object. For the purpose of analysis here, the "true" object, $f(x, y)$, is a given array of irradiance values. Simulated blurred images are created using Equation 3.2 above, and the results from IDA are analyzed for comparison purposes using the true object. The term "object estimate," hereafter designated $\tilde{f}(x, y)$, represents the best guess at the "true" object that IDA can produce. The Fourier transforms of both the true object and the object estimate are represented by the object spectra, $F(u, v)$ and $\tilde{F}(u, v)$, respectively, where (u, v) represents an arbitrary point in the spatial frequency domain.

3.2.2 Point Spread Function (PSF). Sometimes referred to as the impulse response, the true PSF, represented by $h(x, y)$, contains the blurring function for the entire optical system. This includes blurring caused by atmospheric turbulence and the optics. For adaptive optics compensated images, the PSF includes blurring from the optics and any residual phase errors uncorrected by the adaptive optics system (21). IDA estimates the PSF which will be denoted as $\tilde{h}(x, y)$. The Fourier

transform of the PSF is called the optical transfer function (OTF). The true and estimated OTFs are represented by $H(u, v)$ and $\tilde{H}(u, v)$, respectively.

3.2.3 Image. The image is equivalently referred to as the convolution image, the measured image or the measurement. The function, $g(x, y)$, represents the magnitude of the convolution plus any contamination as revealed by Equation 3.2. Its Fourier transform is called the image spectrum and is denoted by $G(u, v)$.

3.2.4 Positivity. Positivity is the assumption that both the object, $f(x, y)$, and the PSF, $h(x, y)$, have positive intensity values. One term in the algorithm's objective function constrains the object and PSF estimates to have a minimum of negative intensity values.

3.2.5 Support. Support is the only "hard" constraint utilized by the IDA method. Two arrays, representing the extent of the object and PSF, respectively, must be provided for the algorithm along with the measured image and initial estimates of the object and PSF. These arrays constrain the object and PSF estimates to have non-zero values only where the support array has a value of one. The remainder of the image plane is set to zero corresponding to the complementary region where the support array is zero. Since the pixels within the object and PSF estimates become the variables for minimization in the unconstrained minimization process, the support arrays actually reduce the number of variables IDA is required to minimize.

3.2.6 Error Metric. The error metric is a function which measures how close or how far an estimate is in relation to its true value. A separate error metric will be calculated for each object and each PSF estimate. Since this metric is calculated using the true object or PSF, it will not be useful for processing real imagery. However, using Davey's philosophy, such an error metric serves as an excellent preliminary assessment of the algorithm's performance (4).

3.3 Computer Simulation of the Problem

This investigation utilizes simulation to reconstruct computer generated images for several reasons. First, baseline data is necessary using pristine, infinite signal images to determine a maximum ability to reconstruct an object under a given set of conditions. Second, the effects of photon noise are to be studied in detail. Obtaining actual imagery where photon noise is dominant is possible, but only with simulated images can the photon level be carefully varied. Modeling photon arrivals as a Poisson process in a computer simulation allows one to analyze the performance of IDA under the strict condition where the contamination, $c(x, y)$ in Equation 3.2, contains only contributions due to photon noise. Finally, computer generated data can be processed and analyzed on the same machine which means that the complexity of data transfer is avoided.

Experimentation through computer simulation is similar to laboratory experimentation. When one approaches computer simulation using the scientific method, tangible results can be obtained. Therefore, before jumping head-first into the iterative deconvolution algorithm, several questions must be asked and answered to guide the experimental process. Five questions follow which provide a scientific approach to computer simulation testing (23).

1. What is the experimental objective?
2. What phenomena will be observed?
3. How will observations be quantified?
4. What are the independent variables affecting the phenomena?
5. What factors will be held constant in the experiments?

Subsequent discussion seeks to answer each of the above questions. The main purpose of the next several sections is to give the goals for the experimentation discussed in Chapter 4. In addition, key factors and variables in the unconstrained

minimization process are listed and defined to provide a better understanding of the results obtained as well as the assumptions that apply to those results.

3.4 *Experimental Objectives*

The overall driving concern for this study lies in answering the following question: Can unconstrained minimization effectively deconvolve an unknown object and unknown point spread function from a single measurement? Though a simple "yes" or "no" could answer the question, neither question nor answer is simple in this case. Implementation of unconstrained minimization through the IDA technique allows many different aspects of the reconstruction process to be estimated or varied. Therefore, several variables were chosen for further analysis. The objectives relating these variables are listed below.

1. *Develop a baseline for object estimates using infinite signal measurements, and determine the optimal support size necessary for reconstruction.* This first objective will allow IDA to process several noiseless, blurred images using a series of well-defined support constraints so that generalizations can be made across all the images tested.

2. *Determine the effect of photon noise on the object estimate and compare with results previously obtained by Lane.* Photon noise can be considered the origin of shot noise in detectors that emit an electron upon absorption each photon (3). Lane revealed that decreasing the light level present in the measurement significantly affects the reconstruction (13). This second objective seeks to test the modifications made by Jefferies and Christou, specifically the addition of a band-limiting mask in the convolution error shown by Equation 2.16 (12). Results using this band-limit mask can be compared with results obtained using Lane's method without the band-limit mask.

3. *Determine the utility of the band-limit error term toward improving the reconstruction process.* Jefferies and Christou define the third error term in their ob-

jective function as the band-limit error which minimizes high frequencies in the OTF estimates (12). This third objective seeks to analyze whether use of the band-limit error shown by Equation 2.18 contributes in a positive way toward the reconstruction process either in terms of reduced iterations or improved object and PSF estimates.

The enumerated objectives just listed form the main goals of the three experiments for which results are presented and analyzed in the next chapter. The purpose for those experiments will be to analyze the performance of Jefferies and Christou's IDA technique. To better understand the results, however, one first must comprehend the algorithm itself and how it achieves a best estimate of an object and PSF. Thus, time must be devoted to understanding the unconstrained minimization technique for blind deconvolution.

3.5 Constraint Driven Phenomena

Laboratory experiments are usually designed to test or reveal some physical phenomenon. Computer simulation can accomplish a similar goal if the mathematical model represents a close approximation to reality. Therefore, the phenomena revealed in the subsequent experiments result directly from the computer algorithm. Although blind deconvolution was defined and a summary of different techniques was outlined in Chapter 2, a more complete knowledge of the unconstrained minimization technique utilized in this investigation is necessary. IDA, developed by Jefferies and Christou as a modification to Lane's method, implements this proposed blind deconvolution solution and is the object for subsequent analysis. The following paragraphs seek to give insight into the Jefferies and Christou algorithm.

Since the Ayers-Dainty method had no well-defined stopping criteria, Lane sought an unconstrained minimization approach to blind deconvolution by developing an algorithm which converged on a best set of object and PSF estimates. The Lane technique formulates the same constraints applied at each iteration in the

Ayers-Dainty method into a single error function. This function is then minimized using conjugate gradient minimization.

3.5.1 Minimization. Conjugate gradient minimization (CGM) is one of a number of steepest-descent iterative search methods. CGM finds at least a local minimum for a multi-variate objective function given an initial starting point for each variable. With a first guess, the CGM method calculates the value of the objective function as well as the gradient at that location. Using this information, the method then selects a subsequent guess in a direction opposite to the gradient. Thus, the next guess traverses the steepest-descent along the complex, multidimensional function. With this new guess, a new objective function value and gradient are found. This process is repeated until the new objective function value is greater than the previous, which implies that the previous point was a local minimum.

IDA implements conjugate gradient minimization on a single error function with several terms. The pixel values within the support of the object and PSF estimate arrays become the variables to be minimized. Therefore, CGM is performed on a single objective function containing hundreds to thousands of variables for even the relatively small image plane array of 64×64 . Fortunately, the error terms derived by Lane and Jefferies have analytic derivatives which simplify the calculation of the gradient at each iteration. Though understanding the CGM process is important, the error terms are the key to the unconstrained minimization process.

3.5.2 Image Error. As discussed in Section 2.5.3, the image domain error term,

$$E_i = \iint_{\gamma_f} |f(x, y)|^2 dx dy + \iint_{\gamma_h} |h(x, y)|^2 dx dy, \quad (3.3)$$

quantifies the squared magnitude of the negative pixels inside the support regions for both the object and PSF where γ_f and γ_h respectively represent the set of negative pixels within the object and PSF support regions. Instead of forcing all negative

values to zero as is done in the Ayers-Dainty approach, IDA seeks to find estimates of the object and PSF where the magnitudes of the negative pixel values are minimized.

3.5.3 Convolution Error. The convolution error term,

$$E_f = \frac{1}{N^2} \iint |G(u, v) - \tilde{F}(u, v)\tilde{H}(u, v)|^2 B(u, v) du dv, \quad (3.4)$$

where N^2 represents the total number of pixels in the image plane and $B(u, v)$ is a band-limit mask, should always dominate the combined error of the objective function since the deconvolution of the object and PSF from the measured image is the goal of this process. This error term can best be expressed in terms of the Fourier transforms due to the convolution theorem (7). As such, Equation 3.4 is minimized when the product of both $\tilde{F}(u, v)$ and $\tilde{H}(u, v)$ equals $G(u, v)$. With the addition of noise in the imaging process, $G(u, v)$ contains high frequency values not present in either $F(u, v)$ or $H(u, v)$. Thus, a band-limit mask, $B(u, v)$, is added to prevent the product of $\tilde{F}(u, v)$ and $\tilde{H}(u, v)$ from having to reconstruct the high frequency noise content. This band-limit mask should allow IDA to handle a greater amount of noise than the Lane method, which does not include the mask.

Another point to be considered is that the noise present within the passband will have to be accounted for within the object and PSF estimates. Even the best estimate of the object and PSF will contain a certain amount of error resulting from the noise whose spectral content lies within the cutoff frequency. Thus, the fundamental limit for restoring the measured image is not reached until the signal cannot be retrieved from the noise present within the passband.

3.5.4 Band-Limit Error. The band-limit error term,

$$E_{bl} = \frac{1}{N^2} \iint |\tilde{H}(u, v)|^2 B'(u, v) du dv, \quad (3.5)$$

is minimized when the magnitude of all spatial frequency values in the OTF beyond 1.39 times the cutoff frequency is zero or very small, where $B'(u, v)$ represents a high pass filter which blocks out OTF values within 1.39 times the cutoff frequency (12). This error term eliminates the occurrence of the trivial solution by preventing the PSF estimate from approaching a delta function. Since the delta function has a Fourier transform extending out to infinite spatial frequencies, limiting the OTF to a specific passband rejects the trivial solution.

Use of this error term also has a distinct disadvantage which was alluded to by Jefferies and Christou (12). As stated above in Section 3.5.3, the spectral content of the noise within the passband must manifest itself in the object and PSF estimates. When the PSF estimate is constrained by the band-limit error term, almost all of the noise within the passband is accounted for in the object estimate. This is the reason why Jefferies states that this constraint "has to be relaxed before convergence" (12).

3.6 Defining Comparison Metrics

Metrics are necessary to quantify errors in the reconstructed objects and PSFs and for comparison against other object and PSF estimates. Since this investigation solely uses computer generated images where the "true" object and PSF are known exactly, metrics are presented which compare an estimate of either the object or PSF with its actual value.

Goodman and Belsher [1976] discuss an error metric which uses a filtered object, call it $\hat{f}(x, y)$, rather than the true object, $f(x, y)$, since "restoration of an object's frequency components beyond the diffraction limited cutoff of the optical system is impossible to achieve with any linear invariant restoration filter" (9). Thus, Goodman suggests that a low pass filtered version of the true object is the best that can be obtained during post-processing. With the understanding that only those frequency components within the passband can be restored, a new error metric for

the object, ξ_f , follows:

$$\xi_f = \frac{\iint_{\gamma} |\hat{F}_n(u, v) - \tilde{F}_n(u, v)|^2 du dv}{\iint_{\gamma} |\hat{F}_n(u, v)|^2 du dv}, \quad (3.6)$$

where γ includes all points within the diffraction limited cutoff, $\hat{F}_n(u, v)$ represents the normalized spectrum of the filtered true object and $\tilde{F}_n(u, v)$ contains the normalized spectrum of the object estimate. Similarly, the PSF error can be written as a function of the true OTF, $H(u, v)$, and the normalized OTF estimate, $\tilde{H}_n(u, v)$, shown by

$$\xi_h = \frac{\iint_{\gamma} |H(u, v) - \tilde{H}_n(u, v)|^2 du dv}{\iint_{\gamma} |H(u, v)|^2 du dv}. \quad (3.7)$$

These error metrics count as error only those differences between the restored spectrum and the filtered true spectrum that lie within the passband. Division by the integral over the power spectrum expresses the comparison metric as a fraction, $0 \leq \xi \leq 1$, for estimates that are reasonably close to the actual value.

Since all objects used in this investigation will contain point sources of varying intensity, additional metrics are useful in defining the error in point source location and the intensity ratio for binary stars in the object estimates. For both true objects and images, the intensity ratio for a binary star is often denoted as $1 : \eta$, where η is defined as the ratio of the intensity of the dimmer star to the intensity of the brighter star. Thus, η , by definition, is less than 1.

A location error is defined for this investigation as the deviation in point source location between the true object and its estimate divided by the blur radius, Φ . Φ represents the radial distance from the center of the array to the first zero in the true PSF, when the PSF is an Airy function. If the PSF remains constant for all images, then the following equation can be used to calculate the location error for a

particular point source,

$$\xi_{loc} = \frac{\sqrt{(\tilde{x}_p - x_p)^2 + (\tilde{y}_p - y_p)^2}}{\Phi}, \quad (3.8)$$

where (x_p, y_p) represents the location of point source, p , in the “true” object and $(\tilde{x}_p, \tilde{y}_p)$ represents the location of point source, p , in the object estimate.

3.7 Independent Variables

From the objectives selected in Section 3.4, several aspects of the unconstrained minimization approach to blind deconvolution need to be isolated. By varying a single component within the isolated set, conclusions can be drawn regarding the effect of that variable on the reconstruction process. To meet the enumerated objectives, this investigation will analyze the IDA technique by varying the object contents, the support size and the light level present in each image.

3.7.1 Objects and Image Measurements. Four different objects were chosen to study the ability of IDA to reconstruct blurred images of astronomical objects. The four object arrays, 64×64 pixels in size, contain point sources of differing intensity. Object A, shown in Appendix B as Figure B.1, represents a single star centered in an empty field. Object B, Figure B.3, is a binary star object of intensity ratio 1:0.7 with a very wide separation. Object C, Figure B.5, shows another binary star object with intensity ratio 1:0.7 where the separation is closer. The final object, Object D (Figure B.7), has the same binary star object with a very close separation. Instead of using separate PSFs, binary point sources of varying separation are employed to show the resolving power of the unconstrained minimization technique.

A single PSF was selected to blur each of the objects listed above. This PSF has a certain radius, Φ , from its center to the first zero which can be measured in pixels, micro-radians or arc-seconds. By defining the separation distance between the point sources in Objects B, C, and D as ϕ , then the ratio, $\frac{\phi}{\Phi}$, represents a general means

of quantifying the separation in the three objects. Using the ratio, $\frac{\phi}{\Phi}$, the separation between the point sources for Objects B, C and D are respectively, 1.81, 0.84 and 0.71. When the PSF is convolved with the true point source objects, much of the detail disappears as revealed in Figures B.2, B.4, B.6 and B.8 which correspond directly to Objects A, B, C and D.

3.7.2 Support Size. The first experiment tests the ability of the algorithm to reconstruct noise-free blurred images with differing support sizes. Support is the only firm constraint input into IDA; thus determining an optimal support region in the first experiment is necessary to effectively running other experiments. It is desirable to test the correlation of support region size with definable areas within the impulse response or true PSF. Since a single PSF in the form of an Airy function is used to blur each object, support size will vary according to the "zeros" of the PSF. Three different support sizes, given in terms of the radius of a circle, were chosen. The first support size extends to the zero region surrounding the main lobe of the true PSF, having the same radius, Φ . The second and third support sizes respectively correspond to the null regions just after the first and second "rings" of the PSF. Support areas are circular regions centered for the PSF support and centered on each point source location for each object support. Thus the object support for one of the binary stars is the union of two circles of varying size each centered on the point source pixel locations. Figure 3.1 reveals an example of a support region for Object B.

Experimental testing will utilize the three separate support regions defined for each object as input into the unconstrained minimization method. Results from this testing can be analyzed to determine how support size affects the blind deconvolution reconstruction process.

3.7.3 Average Photo Events, \bar{K} . The most basic source of noise lies in photon fluctuations associated with the detection of the finite amount of light energy

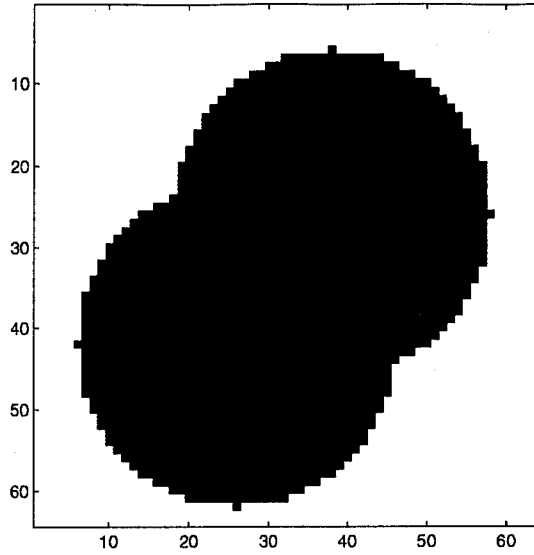


Figure 3.1 The object support region above relates to Object B where each circle is centered on one of the two stars in the true object.

available in the imaging system. These photon fluctuations pose a fundamental limitation to the “restorability” of a degraded image (9). Photon arrival at the detector has been previously modeled as a Poisson process (9, 13, 20). A similar model will be used here to create simulated images corrupted by photon noise. To understand the model, first one must comprehend the factors affecting photon arrival. The mean number of photons or the average number of photo events is a function of the visual magnitude of the object, the image exposure time, the mean imaging wavelength of the detector and the light gathering capacity of the optical device (3).

The model used to generate photon limited images makes use of the Poisson probability mass function defined by Ross [1993],

$$p(x) = e^{-\lambda} \left(\frac{\lambda^x}{x!} \right), \quad x = 0, 1, 2, \dots \quad (3.9)$$

where x represents the number of photon arrivals at a certain location and λ corresponds to the mean number of photons which arrive at a detector cell over a specified period of time (20). The number of photo events at each pixel location is a random

Table 3.1 Visual magnitude and photo events for common sky objects.

<i>OBJECT</i>	m_v	\bar{K}
Venus	-4.4	$2.35 \cdot 10^7$
Jupiter	-2.5	$4.11 \cdot 10^6$
Sirius	-1.5	$1.59 \cdot 10^6$
Artificial Satellite (typical)	-.96	$1.00 \cdot 10^6$
Polaris	+2.2	$5.54 \cdot 10^4$

variable from the Poisson distribution where the ratio of the irradiance in a pixel to the total energy in the noise-free image is proportional to the mean of the random variable, λ . The proportionality constant, \bar{K} , represents the average number of photo events in the entire image over a single exposure or integration time. Thus, the mean of the Poisson random variable at each pixel location, $\lambda(x, y)$, can be expressed in the following way,

$$\lambda(x, y) = \frac{\bar{K} g(x, y)}{\iint g(x, y) dx dy}, \quad (3.10)$$

where $g(x, y)$ represents a point in the noise-free convolution of $f(x, y)$ and $h(x, y)$. Equation 3.10 above was used to generate images corrupted by photon noise for differing photo event levels, \bar{K} . Apparent visual magnitude, m_v , is a convention employed by astronomers to compare the relative brightness of objects in the night sky (17). Each unit decrease in visual magnitude corresponds to a 2.5 factor increase in visual brightness; thus, smaller m_v indicates a brighter object. This same visual magnitude can be used to calculate the average photon flux of an object. Table 3.1 reveals the number of photo events corresponding to the visual magnitude for several common sky objects (23), based on a 1 meter aperture, an imaging wavelength of 500 nm and a 1.8-ms integration time. Three different values were selected for \bar{K} : 100,000, 10,000, and 5,000. The photon limited images for the four objects appear in Appendix B, Figures B.10 through B.21.

3.8 Constants

Now that several variables have been reviewed, a couple of factors must be held constant for accurate analysis of the independent variables. The constants for subsequent experimentation are the OTF and the initial estimates input into Jefferies and Christou's blind deconvolution algorithm.

3.8.1 Optical Transfer Function. As already stated, the OTF used to create all simulated images is held constant so that comparisons can be made regarding the ability of IDA to reconstruct it for different objects and differing amounts of noise. Subsequent experiments use the Airy pattern for the true PSF shown in Figure 3.2. This PSF is theoretically the PSF of a circular diffraction-limited system (11). Goodman [1968] defines the Fourier transform of this PSF, or rather the OTF, for a diffraction-limited circular aperture for incoherent light imaging as follows:

$$H(\rho) = \begin{cases} \frac{2}{\pi} \left[\cos^{-1} \left(\frac{\rho}{\rho_o} \right) - \frac{\rho}{\rho_o} \sqrt{1 - \left(\frac{\rho}{\rho_o} \right)^2} \right] & \text{if } \rho < \rho_o \\ 0 & \text{otherwise,} \end{cases} \quad (3.11)$$

where $\rho = \sqrt{u^2 + v^2}$ and ρ_o denotes the diffraction-limited cutoff frequency (7). By keeping this factor constant, any deviations observed in the PSF estimate result primarily from the object or the noise.

3.8.2 Initial Guesses. The iterative deconvolution algorithm requires an initial estimate at both the object and PSF for a given measured image. In the past, others (1, 12, 13) have input white noise for initial estimates of both the object and PSF. All runs in this investigation will use a single Gaussian estimate for the PSF and will use the measurement as the initial object estimate. Though this procedure draws close to the trivial solution, it also represents a more logical first guess at both values. The object should simply be a variation on the measured image whereas the

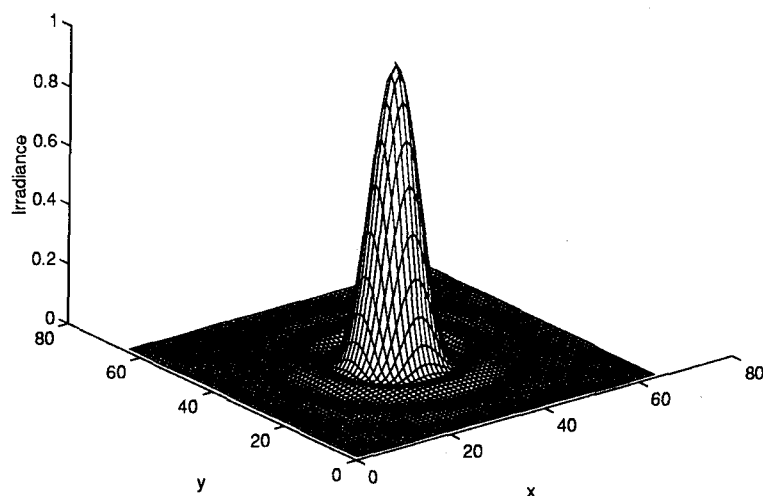


Figure 3.2 The PSF shown above was convolved with the four true objects to obtain the blurred images found in Appendix B.

PSF should contain some of the same properties as the Gaussian—radial symmetry and a smooth roll-off.

3.9 Summary

The merits of the unconstrained minimization approach to blind deconvolution derived by Lane and modified by Jefferies and Christou warrants further analysis. This chapter discussed several points crucial to understanding the experiments for this investigation. As presented, the terminology listed requires merely a basic understanding of Fourier optics. The simplifying assumptions made and the models developed here allow direct application of the findings of this study to actual astronomical images. The objectives defined in this chapter are further developed into actual experiments in Chapter 4. Additionally, the following chapter presents the results of those experiments and analyzes the results in light of the terminology, assumptions and metrics just discussed.

IV. Results and Analysis

4.1 Introduction

To determine how well Jefferies and Christou's iterative deconvolution algorithm (IDA) can reconstruct compensated astronomical imagery, several experiments are performed. These experiments utilize computer simulation to analyze the algorithm's performance under specific controlled conditions. Post-processing is performed using computer generated images. The following sections provide detailed information regarding the three experiments and draw conclusions from the results of each experiment.

4.2 Experiment One

Develop a baseline for object estimates using infinite signal measurements, and determine the optimal support size necessary for reconstruction. As stated in Section 3.4, the first major objective of this experiment involves testing IDA on noise-free images to understand the capability of this blind deconvolution technique without the presence of noise. A secondary goal involves varying the support constraint to determine its impact on the reconstruction process.

4.2.1 Simulation Parameters. Input images for this experiment represent the convolution of the "true" objects with a single PSF as discussed in Section 3.6.1. These four noise-free images (Figures B.2, B.4, B.6 and B.8) are displayed in a three-dimensional view where increasing irradiance corresponds to a higher value on the graph. In addition to the measurements, IDA requires initial estimates at both the object and PSF as well as support regions for both object and PSF in order to begin blind deconvolution processing. As alluded to in Section 3.7.2, three different support regions are selected for each object which utilize some of the known attributes of the true impulse response.

Assuming circular symmetry in the PSF, a circle is chosen as the shape of the support region for the PSF estimate. Knowing the objects are point sources which image into an impulse response or sum of impulse responses, support regions for the objects are also selected to be circular in shape. Therefore, depending upon the number of stars in the image, the support region for the object estimate consists of the total area under separate circular regions centered over each "known" star location. Use of this *a priori* information tests the best reconstruction IDA can obtain. For actual imagery, star locations may be revealed from other more complicated image processing techniques. In that case, support regions may be set up using the known data and subsequent images processed via this blind deconvolution technique.

The size of the circular regions must be determined. An appropriate support size might also be related to the impulse response. In order to tie the support size to the PSF, setting the radius of the support circles to the first, second and third zeros of the PSF is proposed. Since the true PSF in this case is the Airy disk, these zeros correspond to the radial points where the irradiance for an Airy function is zero. Sir George Biddell Airy (1801-1892) first derived an equation defining the irradiance of a point source imaged through a circular aperture (10). Airy's function for intensity, $I(\theta)$, appears below

$$I(\theta) = I(0) \left[\frac{2J_1(ka \sin \theta)}{ka \sin \theta} \right]^2, \quad (4.1)$$

where θ represents the angular distance from the center, k is the wave number, and $J_1(\cdot)$ is a Bessel function of the first kind of order one. The first three zeros for the Airy function occur when the quantity $ka \sin \theta$ is 3.83, 7.02 and 10.17, respectively. Upon integrating the Airy function, one finds that 84% of the light energy is present within the first zero corresponding to the main lobe of the Airy function. 91% of the light energy remains within the second dark ring and over 95% lies within the third zero (10). These zeros correspond to pixel locations for the true PSF used in this investigation. Figure 4.1 shows a slice through the center of the true PSF used to blur the objects for this experiment. Zeros for this PSF occur at 11, 20 and

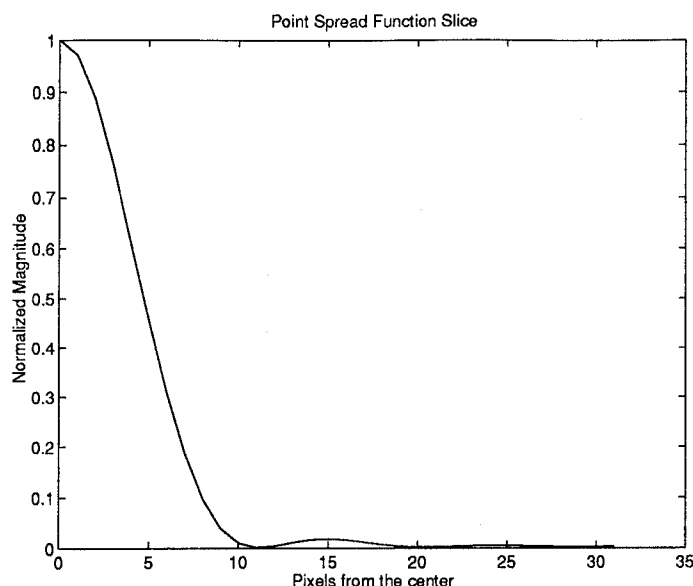


Figure 4.1 A slice through the true point spread function reveals zeros at 11, 20 and 29 pixels from the center.

29 pixels from the center. These pixel values then become the radii of the support region circles used to create support arrays for the object and PSF estimates.

In this first experiment, IDA mimics Lane's method for blind deconvolution since only the image and convolution error terms contribute to the combined error function. Additionally, there is no need to implement Jefferies' band-limit mask as part of the convolution error since no information in the measured image spectrum exists outside of the cutoff frequency defined by the OTF. Thus, applying this mask has no effect on the noise-free images processed in Experiment 1. A total of twelve runs of the deconvolution algorithm are required in this case to process the four images for each of three different support regions.

4.2.2 Simulation Results. Results from the computer simulation runs using unconstrained minimization for noise-free images appear outstanding. Figure 4.2 displays a gray-scaled image of the binary star with the smallest separation—blurred Object D, now called Image D. After blind deconvolution of that measurement using the Lane method, the object estimate clearly reveals the binary star as shown in Fig-

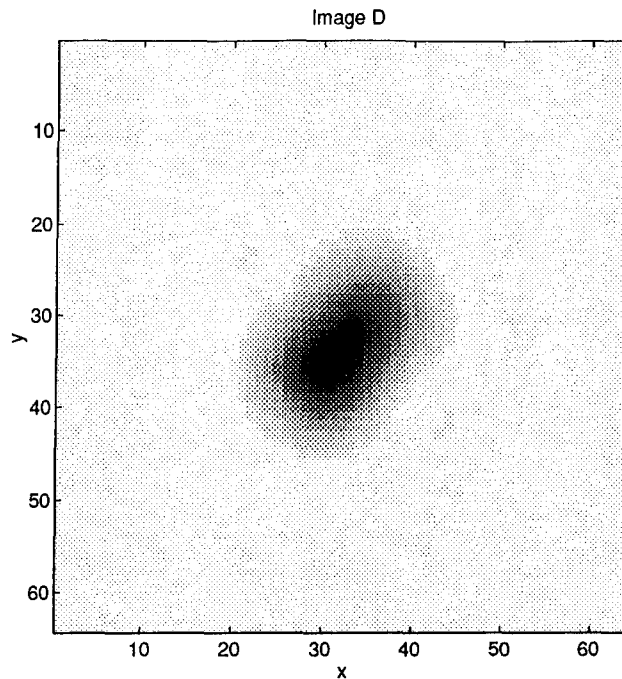


Figure 4.2 Image D, a noise-free blurred image.

Figure 4.3. Three-dimensional plots of the object and PSF estimates resulting from the processed images appear in Appendix C, Figures C.1 through C.24 for Experiment 1.

Section 3.6 defined several metrics which quantify the errors in the object and PSF estimates in relation to the actual objects and PSF. The numerical quantities appear in Table 4.1. Each of the four images were processed using each of three separate support regions defined at either the first, second or third zero in the true PSF. The table refers to the different support regions as 1, 2 or 3, where 1, 2 and 3 represent a circular support radius equal to the distance to the first, second and third zero in the true PSF, respectively. Also listed are the number of iterations required by the Lane method to achieve a local minimum. The total errors for both the object (ξ_f) and the PSF (ξ_h) represent the deviation from the true object or PSF within the passband as defined by Equations 3.6 and 3.7. The location error reveals the ratio of the error in the point source location to the blur radius. In the noise-free

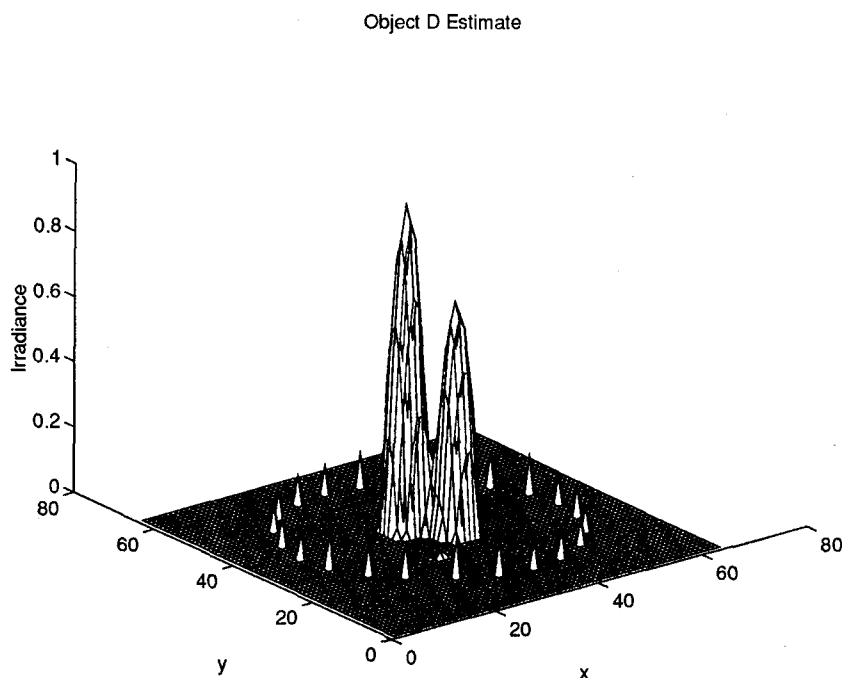


Figure 4.3 Object estimate of Image D after deconvolution using a support region extending out to the second zero of the true PSF.

case, almost all point sources were estimated to be at the exact same pixel location as in the true object, thus having zero location error. The intensity ratio appears for comparison against the true objects B, C and D—each containing a binary star with an intensity ratio of 1:0.7.

For further analysis of the support constraint, plots are shown which reveal the spatial frequency content of the true objects and their respective estimates. Figures 4.4 – 4.7 present the radially averaged, normalized object spectra estimated using differing support regions. In each plot, the horizontal axis displays spatial frequency where “1” represents the cutoff frequency of the optical system. The vertical axis is normalized for comparison purposes, and the magnitudes of the object spectra are radially averaged from the $(u, v) = (0, 0)$ or DC value. Graphed are the following five functions within each figure.

1. First, the true object spectrum appears. This spectrum represents the single or double point sources; therefore, it has infinite frequency content.

Table 4.1 Error metric summary for Experiment 1.

OBJECT / Support	Iter ^a	ξ_f	ξ_h	ξ_{loc} ^b	1 : η ^c
A / 1	294	0.258	0.279	0.000	n/a
A / 2	564	0.111	0.060	0.000	n/a
A / 3	873	0.116	0.045	0.000	n/a
B / 1	3000	1.155	1.541	0.545 / 0.545	1:0.69
B / 2	1184	0.096	0.046	0.000 / 0.000	1:0.70
B / 3	1533	0.146	0.054	0.000 / 0.000	1:0.69
C / 1	3000	0.987	1.867	*** / ***	*** ^d
C / 2	948	0.097	0.051	0.000 / 0.000	1:0.70
C / 3	1057	0.114	0.041	0.000 / 0.000	1:0.71
D / 1	1906	0.661	1.195	0.455 / 0.530	1:0.74
D / 2	1140	0.083	0.051	0.000 / 0.000	1:0.72
D / 3	1052	0.102	0.043	0.000 / 0.000	1:0.68

^aIterations required by IDA for reconstruction.

^bLocation errors are listed for the number of point sources present in the object.

^cIntensity ratio is only applicable for binary stars.

^dFor this estimate, the point source locations and relative intensities were indiscernible.

2. The solid line represents the true object spectrum passed through a lowpass filter with a cutoff frequency equal to that of the blurring function. This solid line reflects the theoretically best achievable solution possible, given that all information outside of the band-limit was discarded by the imaging process.

3. The line furthest away from the desired spectrum, shown by a dotted line in all four graphs, represents the estimates created using the smallest support region—defined by the first zero in the PSF. Inclusion of only the main lobe of the PSF in the support region does not provide adequate information to the algorithm to reconstruct the objects.

4. All four estimates generated from the support region using the second zero in the PSF come closest to the low-pass filtered true object spectrum. This observed quality in the object spectra is revealed quantitatively in Table 4.1, where the total object error, ξ_f , is optimal for support number 2 for each of the four images.

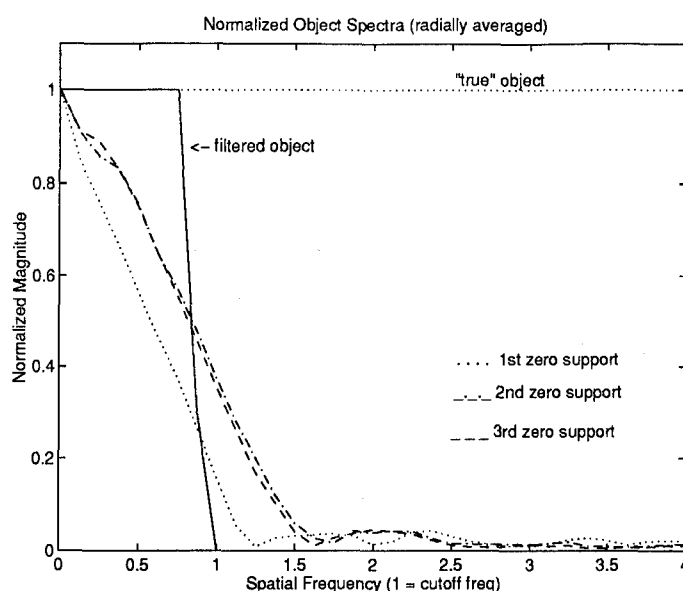


Figure 4.4 Experiment 1: Radially averaged object spectra for Image A comparing the filtered true object spectrum with three estimates using different support regions.

5. Object spectra representing the estimates generated from the support region using the third zero in the PSF remain close to the estimates processed with support region 2. However, the reconstructions shown in the spatial frequency domain reflect a slightly diminished tendency toward following the true object spectrum within the passband.

4.2.3 Conclusions. The object and PSF estimates shown in Appendix C, the comparison metrics in Table 4.1, and the data revealed in Figures 4.4 through 4.7 indicate that Lane's unconstrained minimization approach to blind deconvolution is certainly an acceptable technique for reconstructing blurred noise-free images. Obviously, an accurate estimate of the support for both the object and PSF aids in this reconstruction. For the noise-free, point source objects applied in Experiment 1, a support region which extends out to the second zero in the PSF provides the best estimates. This "second zero" support region will be utilized exclusively for subsequent experimentation. The high frequency content in the spectra and "spikes"

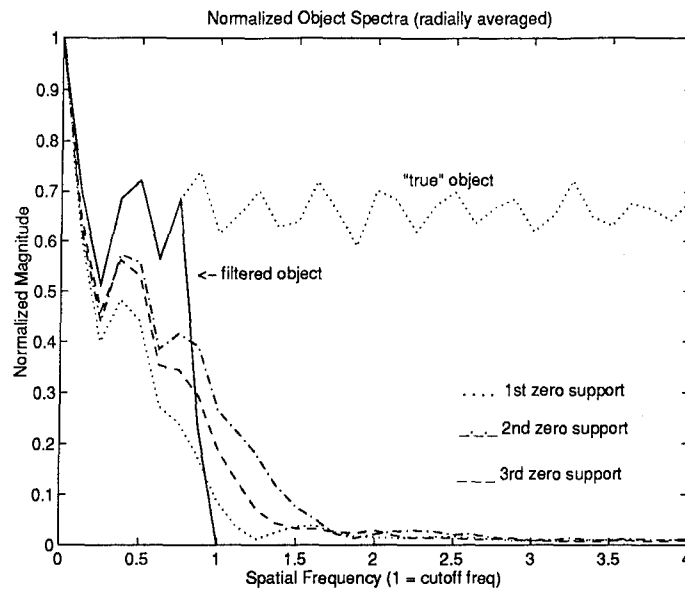


Figure 4.5 Experiment 1: Radially averaged object spectra for Image B comparing the filtered true object spectrum with three estimates using different support regions.

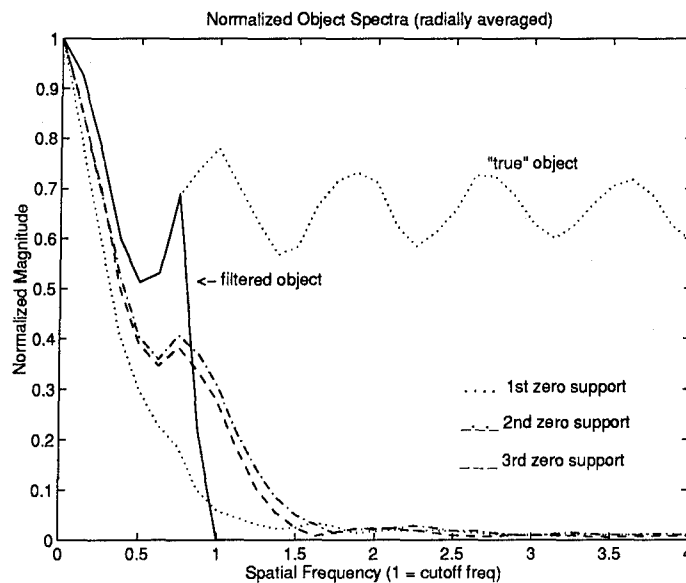


Figure 4.6 Experiment 1: Radially averaged object spectra for Image C comparing the filtered true object spectrum with three estimates using different support regions.

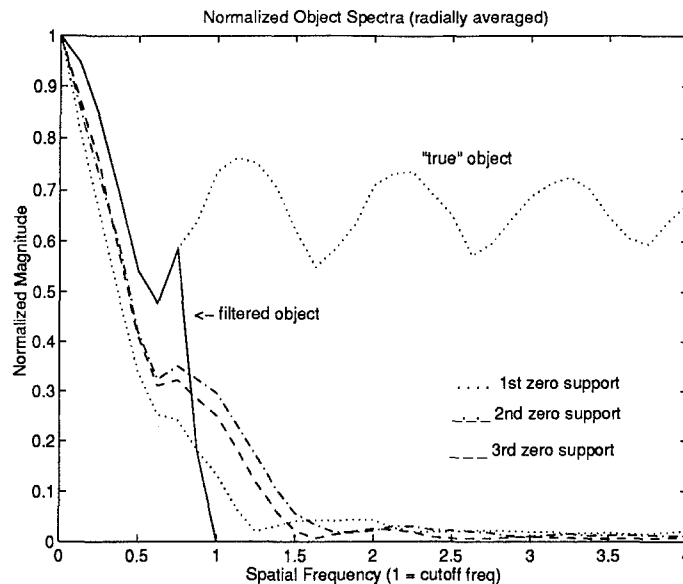


Figure 4.7 Experiment 1: Radially averaged object spectra for Image D comparing the filtered true object spectrum with three estimates using different support regions.

visible in Figure 4.3 at regular intervals as well as the other object estimates deserve further discussion.

Both the high spatial frequencies and the ring of “spikes” probably have a great deal of correlation, especially since the spikes have infinite frequency content. The spikes visible in all of the object estimates shown in Appendix C are formed on the very edge of the support region, thus viewing an estimate gives one a feel for the size of the support region applied. The boundary of the support region presents a large discontinuity in the image plane. This discontinuity may be the single most important factor in understanding the existence of the spikes. Since the appearance of the spikes occur every time, one might reason that their elimination by filtering out all irradiance present on the edge of the support region—essentially, erasing the spikes—would be valid. Another viable option would place the measured image in the center of a much larger array, then choose a support region large enough that the discontinuity occurs outside the original array size. This avenue is alluded to in Jefferies’ statement that his “support constraints were very loose” (12).

Spatial frequencies that are estimated above the cutoff frequency of the optical system pose more questions. The selected means of unconstrained minimization imposes no strict requirements on either object or PSF estimate. Neither the image error nor the convolution error restrict spatial frequency content outside the optical band-limit; thus, Lane's method will always produce information above the band-limit. Jefferies and Christou claim that super-resolution is possible using the unconstrained minimization technique. Jefferies cites Lucy [1992] who demonstrated that if the convolution components are of finite extent, then the positivity constraint permits gains in resolution over the diffraction limit (12). Goodman [1968] also states that retrieving object spectrum values outside the passband is theoretically possible using analytic continuation as long as the object is spatially bounded and the spectral information within the passband is known exactly (7). Others refute this super-resolution claim, stating that all information beyond the cutoff frequency of the imaging system is irrecoverable (2). Regardless of the super-resolution debate, high frequency content present in the object spectrum gives rise to sharp edges within the object in addition to the spikes present around the support edge. Thus, it remains to be proved elsewhere whether the discontinuity at the edge of the support region creates the spikes or whether the high frequency content allowed to exist in the object spectrum results in forming the spikes around the support region.

4.3 Experiment Two

Determine the effect of photon noise on the object estimate and compare with results previously obtained by Lane. Section 3.4 defines the objective of Experiment 2 for applying the unconstrained minimization technique modified by Jefferies to images corrupted by photon noise. Jefferies' modification involves the addition of a band-limit filter to the convolution error term in Equation 3.4 which means that the convolution of the object and PSF estimate do not include the high frequency

noise present in the measured image. These reconstructions can then be compared against noisy images reconstructed using the strict Lane method without the mask.

4.3.1 Simulation Parameters. The only variable parameter for this experiment is the light level present in each simulated image. Section 3.7.3 describes the Poisson model used to generate simulated low light level images. Experiment 2 utilizes the same four blurred images from experiment one but corrupts each with differing amounts of photon noise. Photon noise is quantified in terms of an average number of photo events present in each image. For this experiment, average photo events per image, \bar{K} , of 100,000, 10,000, and 5,000 are used. The resulting noisy images are shown in Appendix B, Figures B.10 through B.21. These twelve images become the measured images input into IDA for subsequent processing.

To maintain consistency among the images, a single support region corresponding to the second zero in the true PSF is utilized throughout this experiment. Additionally, a band-limit equal to the cutoff frequency in the OTF used to blur the objects is required to test the modification to the Lane method recommended by Jefferies and Christou. Finally, as in Experiment 1, Experiment 2 only applies the image and convolution error to the combined error function for minimization.

4.3.2 Simulation Results. Appendix D presents the actual object estimates obtained in Experiment 2 while Table 4.2 summarizes the comparison metrics for the object and PSF estimates.

The first two rows listed for each separate image represent a comparison between Lane's method and the band-limit modification. Both runs used the image containing 10^5 photo events as the measured image. The values for the object error, ξ_f , and the PSF error, ξ_h , reveal a significant decrease in the error value when the band-limit mask is employed. Further evidence can be observed by comparing the resulting object estimates visually as presented in Appendix D, Figures D.1 through D.8. Figures D.1, D.3, D.5 and D.7 show the object estimates using the strict Lane

Table 4.2 Error metric summary for Experiment 2.

OBJECT	\bar{K}	Iter ^a	ξ_f	ξ_h	ξ_{loc} ^b	1 : η ^c
A	10^5 ^d	769	0.437	0.834	0.182	n/a
A	10^5	875	0.207	0.157	0.203	n/a
A	10^4	1001	0.264	0.320	0.288	n/a
A	$5 \cdot 10^3$	1347	0.179	0.152	0.328	n/a
B	10^5	1020	0.293	0.226	0.091 / 0.091	1:0.69
B	10^5	1976	0.092	0.048	0.000 / 0.091	1:0.77
B	10^4	2743	0.138	0.077	0.091 / 0.091	1:0.76
B	$5 \cdot 10^3$	1530	0.292	0.412	0.288 / 0.257	1:0.77
C	10^5	832	0.316	0.302	0.257 / ***	*** ^e
C	10^5	1995	0.080	0.041	0.091 / 0.128	1:0.77
C	10^4	1109	0.193	0.155	0.182 / 0.091	1:0.68
C	$5 \cdot 10^3$	1643	0.313	0.460	0.364 / 0.203	1:0.91
D	10^5	1042	0.258	0.235	0.091 / ***	*** ^f
D	10^5	1270	0.105	0.066	0.091 / 0.128	1:0.76
D	10^4	1221	0.292	0.392	0.182 / 0.203	1:0.73
D	$5 \cdot 10^3$	3000	0.595	0.691	0.386 / 0.273	1:0.84

^aIterations required by IDA for reconstruction.

^bLocation errors are listed for the number of point sources present in the object.

^cIntensity ratio is only applicable for binary stars.

^dThe first line for each image ($\bar{K} = 10^5$) displays the metrics for estimates resulting from the strict Lane method. Subsequent runs utilize the band-limit mask.

^eThe dimmer point source location was indiscernible. Thus, no intensity ratio was calculated.

^fSee footnote e.

method on the photon noise corrupted Images A, B, C and D, respectively. Figures D.2, D.4, D.6 and D.8 reveal the smooth nature of the object estimates utilizing the band-limit mask. The Lane method proved unsuccessful at reconstructing images containing fewer than 10^5 photo events. Therefore, the only comparison made was for images where $\bar{K} = 10^5$.

Another method of viewing the results of the band-limit mask comparison involves plotting the radially averaged object estimate spectra. Figures 4.8 through 4.11 plot these spectra along with the filtered and unfiltered true object spectra. As previously determined, the estimates made using the band-limit mask more closely

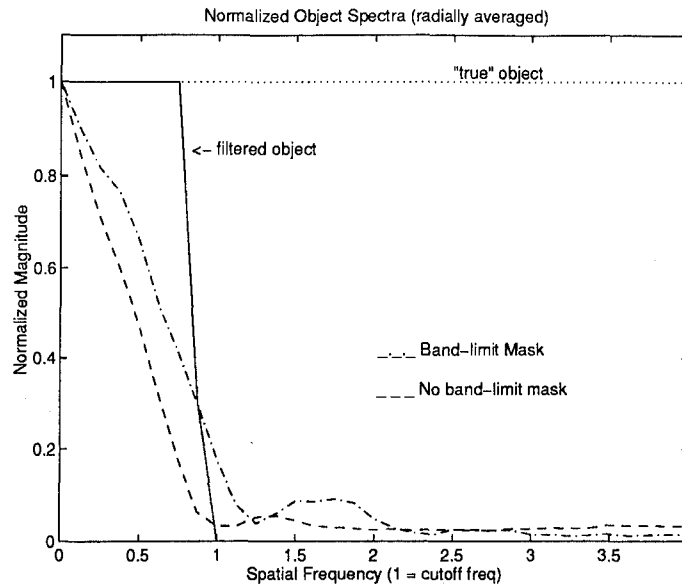


Figure 4.8 Experiment 2: Radially averaged object spectra for Image A ($\bar{K} = 10^5$) comparing the use of the band-limit mask to Lane's method. The filtered and unfiltered true object spectra appear as reference.

follow the true object spectrum than those using Lane's method. Evidence from the spectra as well as the object estimate lead one to conclude that the high frequency noise content in the image spectrum hinders the reconstruction process.

Knowing that the band-limit mask on the convolution error aides in the reconstruction of noisy images, results from images with differing light levels can now be presented. Figures D.10 through D.17 in Appendix D present the object estimates resulting from average photo event levels of 10,000 and 5,000. As previously shown by Lane (13), photon level significantly affects the reconstruction of images limited by the length of the exposure or the object's intensity. Table 4.2 reveals that in almost all cases, decreasing the average number of photo events increases the error in both the object and PSF estimates. The same conclusion is reached when one views the radially averaged object spectra shown in Figures 4.12 through 4.15. Except for Image A, each spectrum steps further away from the filtered true object spectrum as \bar{K} decreases. As the number of photo events decreases, the noise present in the measurement increases across spectral lines. Therefore, the increased noise within

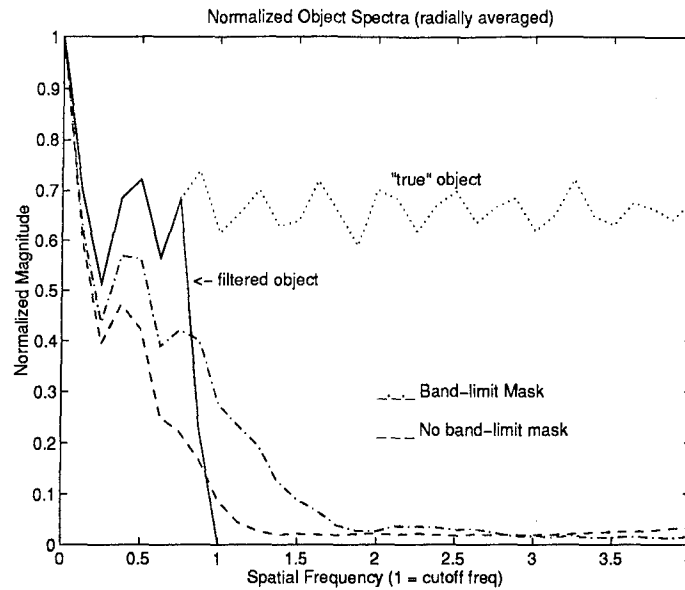


Figure 4.9 Experiment 2: Radially averaged object spectra for Image B ($\bar{K} = 10^5$) comparing the use of the band-limit mask to Lane's method. The filtered and unfiltered true object spectra appear as reference.

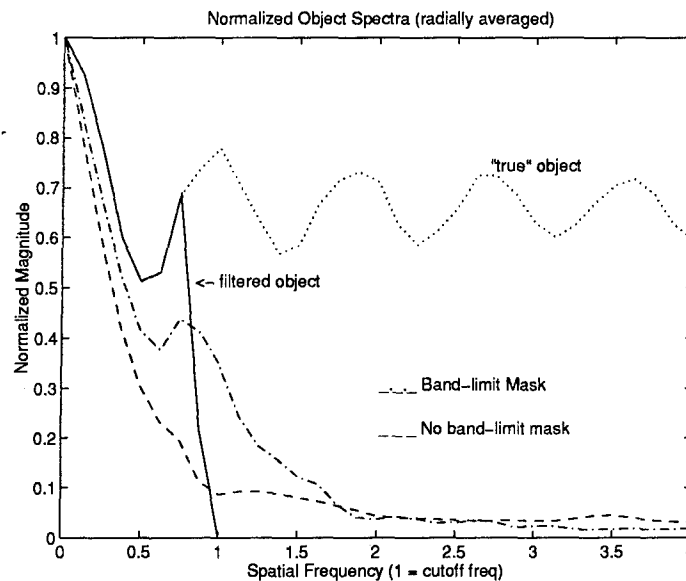


Figure 4.10 Experiment 2: Radially averaged object spectra for Image C ($\bar{K} = 10^5$) comparing the use of the band-limit mask to Lane's method. The filtered and unfiltered true object spectra appear as reference.

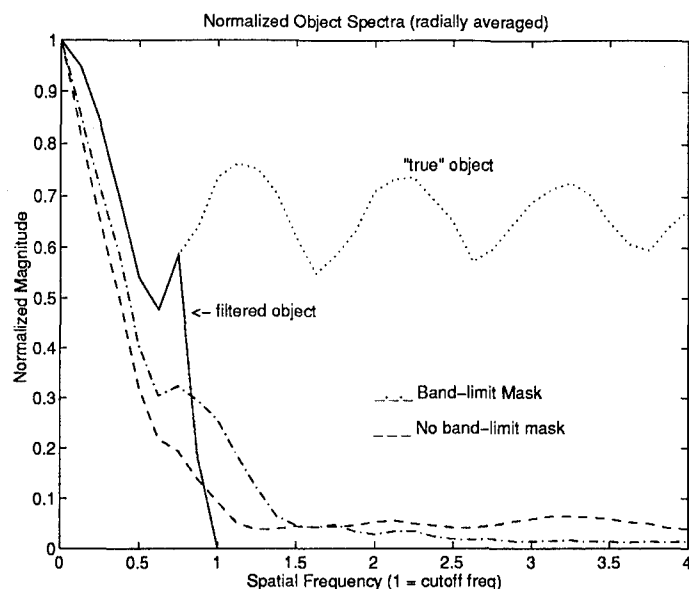


Figure 4.11 Experiment 2: Radially averaged object spectra for Image D ($\bar{K} = 10^5$) comparing the use of the band-limit mask to Lane's method. The filtered and unfiltered true object spectra appear as reference.

the passband manifests itself as greater error within the object and PSF estimates. For images with around 1,000 photo events, the resulting object and PSF estimates are very poor and thus, not presented in this analysis.

4.3.3 Conclusions. Experiment 2 was designed to test the validity of the band-limit mask as applied to photon limited images as well as determine the ability of IDA to reconstruct images with low light levels. As expected, decreasing the light level or number of photo events present in an image significantly degrades the reconstruction. The random arrival of photo events within an image effectively act as noise. Therefore, a limit to the reconstruction is reached when the photon noise sufficiently conceals the signal present in the image.

The results definitively prove the positive utility of the band-limit mask on the convolution error. This mask allows Jefferies' algorithm to reconstruct images with far less light present in the measurement than with Lane's method. The mask effectively filters out the high frequency content of the noise, and subsequently allows

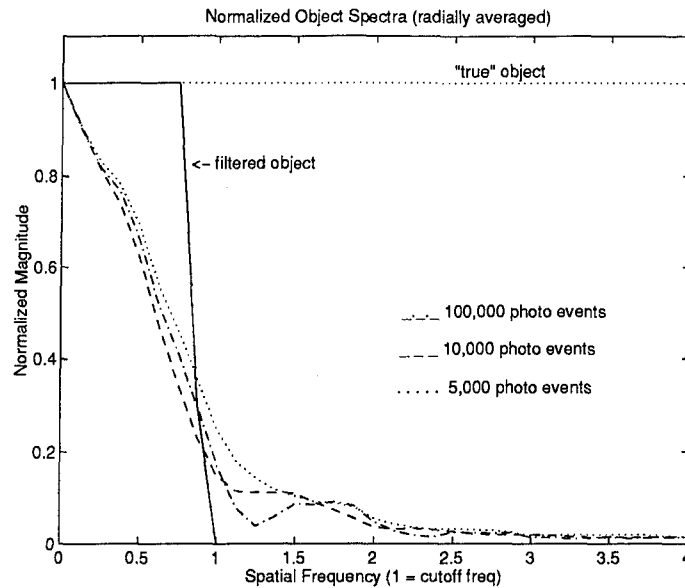


Figure 4.12 Experiment 2: Radially averaged object spectra for Image A applying the band-limit mask to images with differing amounts of photon noise, $\bar{K} = 10^5, 10^4$ and 5,000. The filtered and unfiltered true object spectra appear as reference.

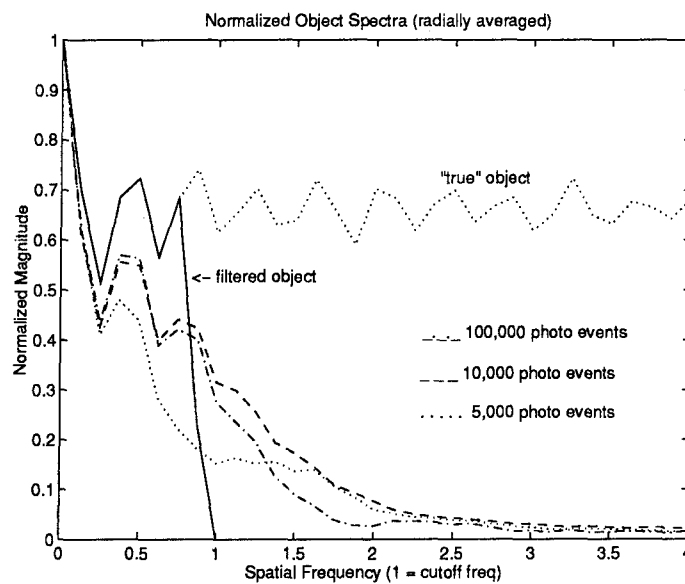


Figure 4.13 Experiment 2: Radially averaged object spectra for Image B applying the band-limit mask to images with differing amounts of photon noise, $\bar{K} = 10^5, 10^4$ and 5,000. The filtered and unfiltered true object spectra appear as reference.

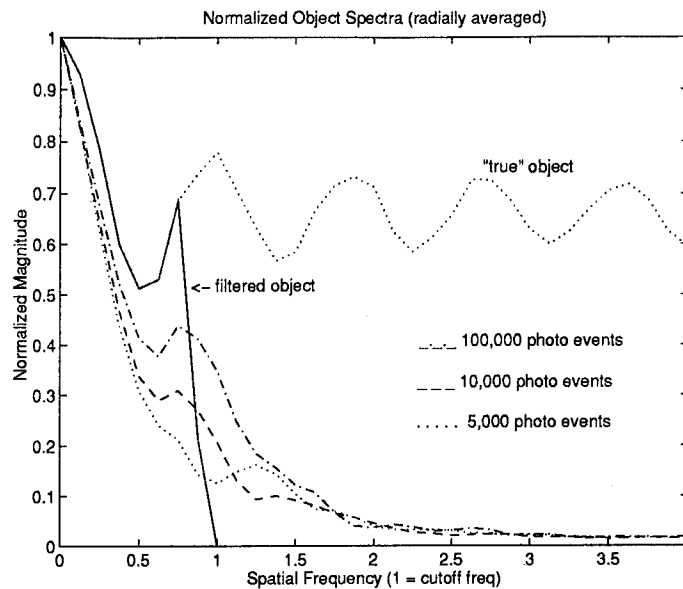


Figure 4.14 Experiment 2: Radially averaged object spectra for Image C applying the band-limit mask to images with differing amounts of photon noise, $\bar{K} = 10^5, 10^4$ and 5,000. The filtered and unfiltered true object spectra appear as reference.

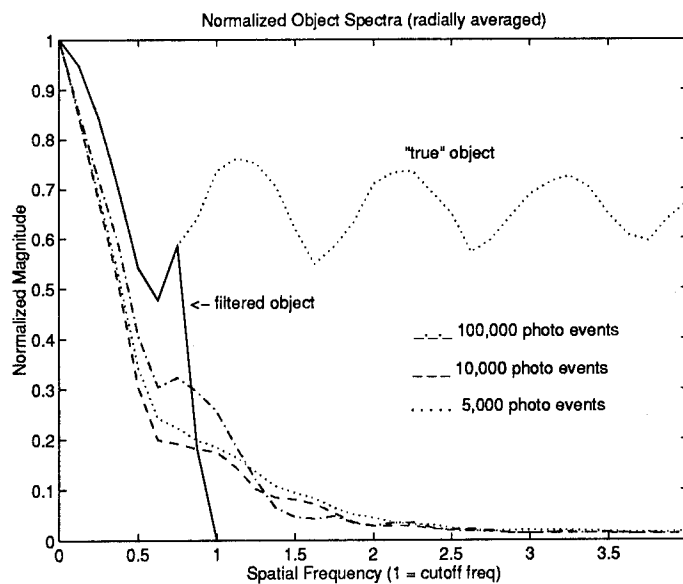


Figure 4.15 Experiment 2: Radially averaged object spectra for Image D applying the band-limit mask to images with differing amounts of photon noise, $\bar{K} = 10^5, 10^4$ and 5,000. The filtered and unfiltered true object spectra appear as reference.

reconstruction of images with a much lower signal-to-noise ratio. As revealed in Lane [1992], unconstrained minimization cannot effectively reconstruct images when the number of photo events in the brightest pixel is less than 10^4 (13). With the band-limit mask, however, excellent results can be obtained when the brightest pixel has less than 10^2 photo events present as expressed in Figure D.14 which shows the reconstruction of Figure B.17 containing fewer than 70 photo events in its brightest pixel.

4.4 Experiment Three

Determine the utility of the band-limit error term toward improving the reconstruction process. With the success of the band-limit mask in the convolution error term, this final experiment studies the band-limit error term, shown in Equation 3.5, which requires a knowledge of the same information necessary in Experiment 2. If the cutoff frequency of the optical system is known for a given image, then the band-limit error term might prove useful in the reconstruction process just as the band-limit mask greatly improved the object estimates in the previous experiment. A look at the comparison metrics and the number of iterations required in this experiment compared with similar quantities available from previous experiments for the same measurement should provide an understanding of the effect the band-limit error has on the blind deconvolution process.

4.4.1 Simulation Parameters. Experiment 3 differs from previous runs using this unconstrained minimization technique in that a third error term is added to the objective function to be minimized. The only input this third term requires is the band-limit of the imaging system, which is also required for use of the band-limit mask in the convolution error term. The convolution error term retains the band-limit mask and thus remains unchanged from Experiment 2. The image domain error term still minimizes any negative values in either the object or PSF estimates. As for support, the optimal support size determined in Experiment 1 will be input

once again in this study. *A priori*, one must know the linear extent of the second zero in the impulse response in the image domain and know the band-limit of the impulse response in the frequency domain.

Selected images used in this experiment include the four infinite signal blurred images applied in Experiment 1 and their simulated, light limited images used in Experiment 2 with average photo events of 10^5 and 10^4 . This experiment will input twelve different simulated images into the iterative deconvolution algorithm to test the utility of the band-limit error term. Jefferies and Christou state that the use of the band-limit term must "be relaxed before convergence" (12). Therefore, one can expect that the algorithm will run for a number of iterations with the band-limit error term, then converge after a series of more iterations using only the image domain and convolution error terms.

Some preparatory analysis provides useful data regarding the use of the band-limit term. The purpose for this term is to reduce high spatial frequency content in the PSF estimate. Figures 4.16 and 4.17 reveal the consequence of allowing the band-limit error to be used until convergence for noise-free Image B. The PSF estimate is very smooth and has the appearance of an Airy function, yet its error, ξ_h , of 0.423 is much larger than the error value obtained in Experiment 1 for the same measurement and support—see Image B, support 2 in Table 4.1. On the other hand, the object estimate consists of two rings centered on the actual point source locations. The object error, ξ_f , is 0.376 which is almost four times greater than the error obtained in Experiment 1 (see Table 4.1). As Figure 4.17 shows, only the rings contain the intensity and the points inside the ring have no intensity. Obviously, allowing the band-limit term to remain in the error function until convergence increases the object and PSF errors. The method used for this experiment allows the band-limit term to be used for the first fifty iterations, then the current estimates at iteration fifty are input as the initial guesses for the algorithm using only the image domain and the convolution error terms.

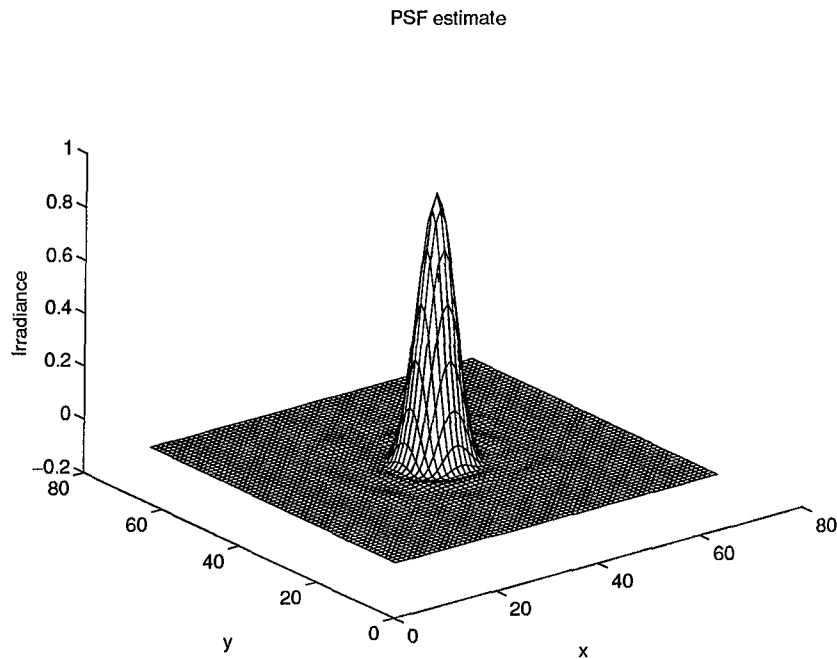


Figure 4.16 Experiment 3: PSF estimate of Image B after 2693 iterations using the band-limit error term to convergence. The band-limit term effectively constrains high spatial frequencies within the PSF estimates.

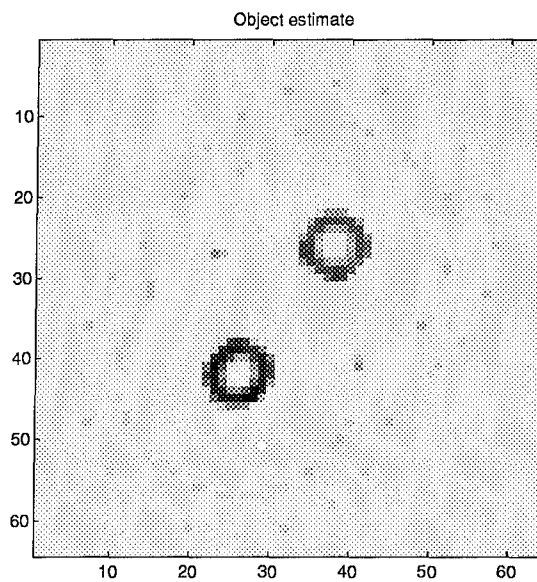


Figure 4.17 Experiment 3: Object estimate of Image B after 2693 iterations using the band-limit error term to convergence. Note the circular rings which surround the true point source locations, though these locations possess no intensity.

4.4.2 Simulation Results. Strict application of the band-limit error gives inconsistent results. Comparing these results with those established in previous experiments reveal a wide range of differences. Figures 4.18 through 4.21 show the results of processing the $\bar{K} = 10^5$ images with the band-limit error next to the results for the same simulated image in Experiment 2. Again, the filtered and true object spectra appear as references. From the graph, Image D (Figure 4.21) shows little deviation in the two reconstructions and would lead one to believe that the band-limit error has minimal effect on the algorithm. However, Image A (Figure 4.18) reveals an improvement with the band-limit error whereas Images B and C (Figures 4.19 and 4.20) show that application of the error has a detrimental effect on the object estimates.

Table 4.3 presents the comparison metrics for each object and PSF estimate. Metrics for the infinite signal images can be compared with data from Experiment 1 using the same support region. The use of the band-limit error term improves Image A, but requires almost four times as many iterations. Image D has very similar results in both cases, but metrics for Images B and C were much lower without the band-limit error term in Experiment 1 as shown in Table 4.1.

Similar results were obtained applying images corrupted by photon noise to this study. When compared against similar data in Table 4.2 for the simulated photon limited measurements from Experiment 2, the band-limit error significantly improves Image A in terms of the metrics, ξ_f and ξ_h . However, this error shows little deviation from previous results for Images C and D and proves detrimental for the reconstruction of Image B. Appendix E, Figures E.1 through E.12, displays the resulting object estimates for all of the data presented in Table 4.3.

4.4.3 Conclusions. The inconsistent results make drawing conclusions from Experiment 3 very difficult. From the limited number of images processed, the best results in using the band-limit error occur when the point sources are grouped closely

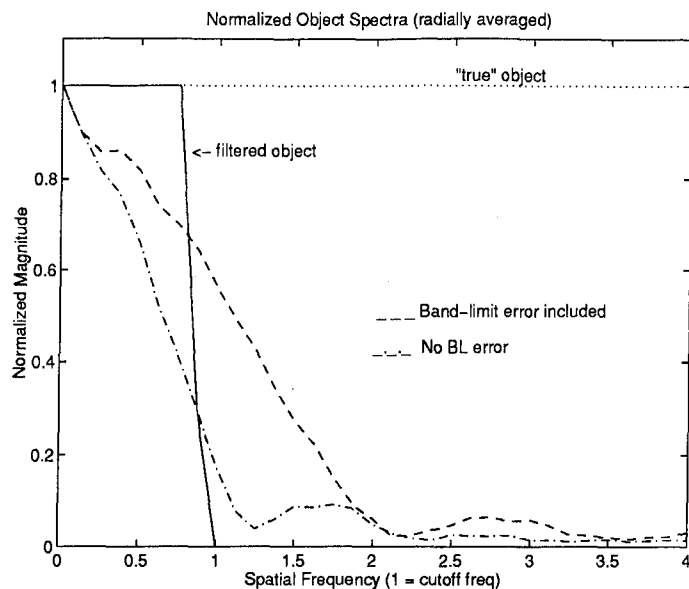


Figure 4.18 Experiment 3: Radially averaged object spectra for Image A comparing the object estimate reconstructed with the aide of the band-limit error to the estimate found in experiment 2 without the error.

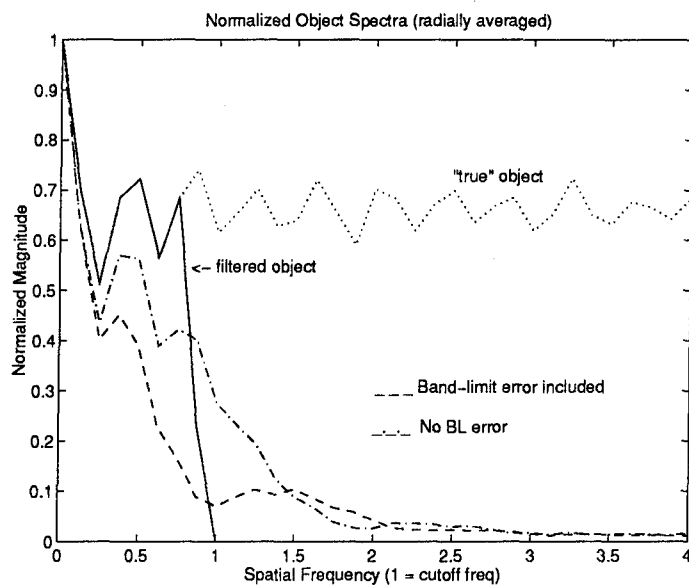


Figure 4.19 Experiment 3: Radially averaged object spectra for Image B comparing the object estimate reconstructed with the aide of the band-limit error to the estimate found in experiment 2 without the error.

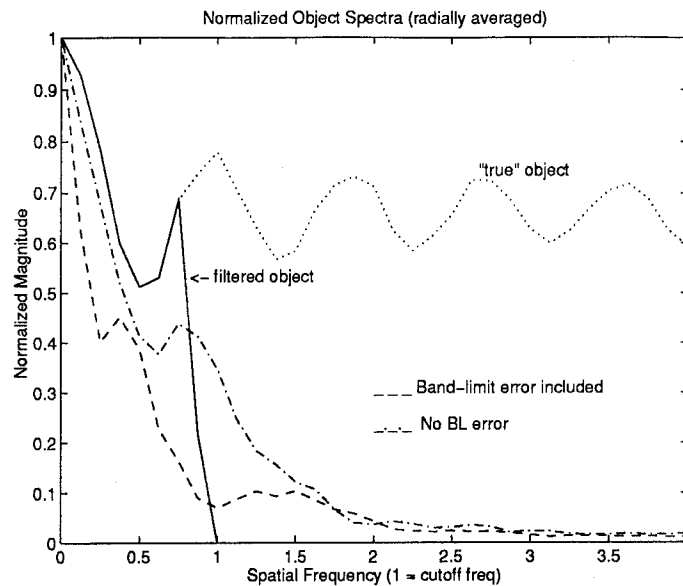


Figure 4.20 Experiment 3: Radially averaged object spectra for Image C comparing the object estimate reconstructed with the aide of the band-limit error to the estimate found in experiment 2 without the error.

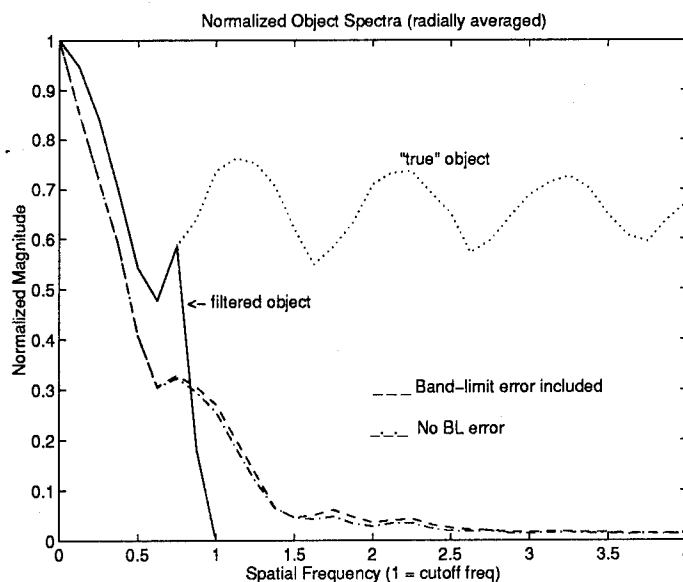


Figure 4.21 Experiment 3: Radially averaged object spectra for Image D comparing the object estimate reconstructed with the aide of the band-limit error to the estimate found in experiment 2 without the error.

Table 4.3 Error metric summary for Experiment 3.

OBJECT	K	Iter ^a	ξ_f	ξ_h	ξ_{loc} ^b	$1 : \eta$ ^c
A	∞ ^d	2105	0.059	0.036	0.000	n/a
A	10^5	2590	0.058	0.036	0.000	n/a
A	10^4	2739	0.103	0.071	0.091	n/a
B	∞	2693	0.372	0.635	*** / ***	*** ^e
B	10^5	1625	0.372	0.678	0.328 / 0.328	1:0.82
B	10^4	2169	0.536	2.262	0.257 / 0.257	1:0.71
C	∞	2113	0.335	0.508	*** / ***	*** ^f
C	10^5	2212	0.091	0.046	0.091 / 0.128	1:0.80
C	10^4	1569	0.211	0.185	0.182 / 0.182	1:0.66
D	∞	1260	0.083	0.047	0.091 / 0.128	1:0.77
D	10^5	1680	0.104	0.063	0.091 / 0.128	1:0.79
D	10^4	1002	0.296	0.415	0.182 / 0.128	1:0.71

^aIterations include fifty with the band-limit error then all subsequent iterations without the band-limit error.

^bLocation errors are listed for the number of point sources present in the object.

^cIntensity ratio is only applicable for binary stars.

^dThe first line for each image ($\bar{K} = \infty$) displays the metrics for estimates resulting from a noise-free, infinite signal image.

^eThe dimmer point source location was indiscernible. No intensity ratio was calculated.

^fSee note e.

around the center of the image. For Image B which contains two point sources spaced far apart, unsatisfactory results were obtained. As the point sources approach one another, the results approach those of Experiment 2. These trends seem to indicate that the band-limit error works better when applied to images containing information tightly grouped around the central point in the image plane.

In terms of the unconstrained minimization method, the addition of the band-limit error alters the objective function and thus changes the direction of the search for a local minimum. In some cases, this change in search direction can be a help and in others it might be a hindrance. Also a factor may be the number of iterations one should optimally take in this new search direction. More analysis is required to determine whether the number of iterations performed using the band-limit error might have a correlation with improved results. Perhaps improvement might be made for different images using a different number of initial iterations with the band-limit error.

4.5 Summary

This investigation sought to test whether unconstrained minimization might be an effective tool in solving the blind deconvolution problem for compensated imagery. Therefore, experiments were run on simulated blurred images with and without photon noise to determine the ability of the Lane method as modified by Jefferies and Christou to reconstruct imagery. Experimental objectives included the following: (1) a test of the support criterion, (2) analysis of the band-limit mask in the presence of photon noise, and (3) a study of the band-limit error term used by Jefferies and Christou. Results from these experiments provided answers to some questions, but generated several more. For instance, the high spatial frequency content produced in the noise-free case remains in the object and PSF estimates throughout all of the experiments. Though the high frequency information yields well-defined point sources apart from the image plane, spikes also appear on the

edge of the support region. The validity of the high frequency information also deserves further attention. Analysis may prove that this unconstrained minimization technique performs some analytic continuation as described by Goodman [1968] as necessary for super-resolution (7).

Along with the many questions evolving from this investigation, some positive results arose also. Resulting data proves that the unconstrained minimization technique can accurately recover object information from a measured image with very little information regarding the impulse response. The accuracy of the object and PSF estimates have a high dependence upon the choice of the support region. Excellent results were obtained using a support region extending out to the second zero in the true point spread function. Additionally, the band-limit mask contained in the convolution error term allows the algorithm to handle more noise in a measurement than the strict Lane method. This mask ensures that the object and PSF estimates convolve to form the portion of the measurement contained within the passband of the optics. Thus, *a priori* information regarding the cutoff frequency is essential in reconstructing low light level images. Lastly, the band-limit error term acts as an additional factor which may improve the quality of the reconstructed image. Its use will prevent the trivial solution from occurring, but using the band-limit term to alter the search pattern of the minimization routine may also produce some positive effects on the eventual "best" object estimate.

V. Conclusion and Recommendations

5.1 Introduction

Imagery obtained through the adaptive optics telescope at AMOS require additional processing to remove the blurring still present in the images. Little information is known about the blurring function which produces the images output from the adaptive optics telescope; thus a means of processing the compensated imagery is necessary which does not require knowledge of the PSF. The term given to this type of problem is blind deconvolution.

Over the last few years, several techniques have been suggested which attempt to iteratively solve the blind deconvolution problem with subsequent estimates at an object and a PSF under certain known constraints. Ayers and Dainty developed the first working algorithm which successively constrained object and PSF estimates in both the image domain and spatial frequency domain. The Ayers-Dainty technique also had some problems in that no avenue existed within the algorithm for determining when the best estimate of the object and PSF had been reached. Holmes and Lane reached separate solutions for determining convergence criteria for the blind deconvolution problem. Holmes formulated the problem in terms of a maximum-likelihood approach and Lane developed an unconstrained minimization method. This investigation focused on analyzing the unconstrained minimization technique to solve the problem of deconvolving a simulated image with little or no information about the impulse response.

Methods were explained and experiments were developed around analyzing the Lane method to solving blind deconvolution as modified by Jefferies and Christou [1993]. Simulated imagery was used to test the response of the iterative deconvolution algorithm to noise-free images and images corrupted exclusively by photon noise. The objectives tested involved observing the results of differing support sizes, studying the effects of a band-limit mask to reconstruct noisy images, and determining

the utility of a new error term designed to reduce high spatial frequency content in the optical transfer function estimates. Results produced by the experiments proved extremely promising. With information regarding only the band-limit of the optics, this algorithm effectively deconvolved noise-free data as well as simulated images modeled to contain differing amounts of photon noise. Several important conclusions were also drawn from the experimentation that deserve further enumeration.

5.2 Conclusions

In addition to accurately recovering object information from measurements with an unknown impulse response, results from the investigation of the unconstrained minimization technique revealed several significant conclusions.

1. The accuracy of the object and PSF estimates are highly dependent upon the choice of the support region. Excellent results were obtained using a support region extending out to the second zero in the PSF, where the area within the second zero retains 91 percent of the volume of the actual PSF.

2. The band-limit mask contained in the convolution error term allows the algorithm to handle significantly more noise in a measurement than the strict Lane method. This mask ensures that the object and PSF estimates convolve to form the portion of the measurement contained within the passband of the optics. Thus, *a priori* information regarding the cutoff frequency is essential in reconstructing low light-level images.

3. The band-limit error term acts as an additional factor which may improve the quality of reconstructed images. Its use will always prevent the trivial solution from occurring, but using the band-limit term to alter the search pattern of the minimization routine may also produce some positive effects in the object estimate. Since the band-limit error term can have a negative impact on the reconstruction, special care must be taken with regard to using this term.

4. High spatial frequency information, outside of the cutoff frequency, appears in the object and PSF estimates. Due to the nature of unconstrained minimization, nothing prevents the inclusion of this information. The information manifests itself in the object estimate as well-defined edges, meaning that no gradual roll-off occurs in the transition from high intensity regions to low intensity regions within the image plane. This quality improves the resolution of the object estimate beyond the diffraction limit. However, the high frequencies also contribute to spikes which form at regular intervals around the edge of the support region. The presence of this information above the cutoff frequency may lead some to question the validity of the results.

5.3 Recommendations for Further Research

Obviously much more research is required before the unconstrained minimization approach to blind deconvolution could be used operationally at AMOS. This investigation, however, seeks to present a basic framework to be built upon in subsequent research efforts. A single blind deconvolution technique is analyzed for objects containing single and double point sources. The following items are recommendations for future research aimed at producing an operational algorithm to improve the quality of compensated imagery similar to that produced at AMOS.

1. Try weighting the different error terms in the objective function. Evidence from Experiment 3 indicates that the band-limit error term can help or hinder the reconstruction process. A variable weight on the band-limit term as well as the image domain and convolution error terms may reveal an improved convergence or possibly enhanced object and PSF estimates.

2. Determine the steps necessary to reconstruct extended objects through the unconstrained minimization technique. Continuous extended objects, like satellites, pose entirely new problems when imaging through the atmosphere. Although outstanding results were obtained on point source objects, a blurred extended object

may prove very difficult to reconstruct using this method. The process of testing the iterative deconvolution algorithm should start where this investigation leaves off—with multiple point source objects. Adding more point sources should provide an understanding of how the algorithm performs for larger, more complex images. Modifications to the unconstrained minimization technique are most likely required to enable the recovery of detailed information in extended objects through blind deconvolution.

3. To reconstruct compensated images of satellites, compare unconstrained minimization to maximum-likelihood estimation as a different means to accomplish the goal of blindly deconvolving extended object data. A more thorough analysis of the work by Holmes (11) and Schulz (21) may lead to a more robust blind deconvolution algorithm capable of handling the complexity of extended objects.

4. Analyze the source of the high spatial frequency information found in the object and PSF estimates produced by this algorithm. Further research is required on Jefferies and Christou's claim that their iterative deconvolution algorithm can super-resolve blurred images (12). Such research would certainly help validate this method and give credence to the results of the algorithm which contain spatial frequency information beyond the band-limit of the imaging system.

Appendix A. Iterative Deconvolution Algorithm Tutorial

A.1 Introduction

This investigation focuses on the iterative deconvolution algorithm (IDA) developed by Stuart Jefferies and Julian Christou who graciously provided the actual code used in their paper (12). The IDA code (annotated simply IDA for this appendix) is an extensive image processing package. It provides numerous options for performing blind deconvolution and "not-so-blind" deconvolution. The program can take simply a measurement and initial guesses at both an object and PSF and iteratively alter the object and PSF estimates toward a best estimate of each using the Lane method (13) of unconstrained minimization. If more information is available, like the band-limit of the optics or Fourier modulus data, then IDA uses this information in an unconstrained minimization approach which is a modification to the Lane method. Additionally, IDA handles multiple images of the same object with ease. The program runs on a SUN workstation. The following sections discuss how IDA implements the algorithm derived by Lane and modified by Jefferies and Christou, the input required to run the program and the proper format for the data, what options are available in processing images, and the modifications which must be made each time IDA is run on a different image.

A.2 How IDA works

As revealed in Section 3.5, IDA solves the blind deconvolution problem through the minimization of an error function. Minimization is achieved through a conjugate gradient minimization routine which finds a local minimum to a multi-dimensional objective function through a steepest-descent search method. Such a method requires only a subroutine to calculate the value of a function at a particular location and another subroutine to calculate the derivative at the location. IDA provides these

subroutines to the conjugate gradient minimization function using the error terms and their derivatives presented in Jefferies and Christou [1993].

IDA minimizes the combined error function shown in Equation 2.16. Each pixel location in both the object and PSF estimate represent the different variables from which the error function must be minimized. The support region input is utilized by the program to reduce the number of variables. IDA only includes those pixel locations for both the object and PSF which lie within the support region. All other pixels are set to zero outside the support. Using the arrays provided for initial estimates, IDA picks off the value at each pixel location within the support to create the series of values for a first guess at the object and PSF estimate.

The conjugate gradient minimization routine alters each pixel value in the series in a direction opposite to the gradient. Thus, each successive iteration reduces the combined error function value. The iterations cease when one of three things occur: (1) a local minimum is reached such that any variation in pixel values causes an increase in the objective function, (2) the reduction in the error function value for each iteration decreases below a pre-set tolerance, or (3) a maximum number of iterations is reached.

A.3 Required Input

Running IDA requires several input data files. Modifications made to Jefferies and Christou's code for this investigation require that the data files be formatted in either binary or ASCII. Below, each of the inputs are defined and the appropriate formats are annotated.

A.3.1 Convolution Image. IDA first requires a filename containing the data representing the convolution image, also known as the measurement. A binary format is required for this data.

A.3.2 Object Estimate. The second input necessary to reconstruct an object from the input measurement is the filename containing the initial estimate at the object in binary format. At regular intervals in the iteration process, the current object estimate will be written to this file. A binary representation of the final estimate appears in this file alone after IDA completes; thus, the initial estimate contained in this file is destroyed.

A.3.3 PSF Estimate. Similar to the object estimate, IDA requires the name of the binary file containing the first guess at a PSF. This estimate is also overwritten by successive estimates. Upon completion of the program, this file contains the final estimate at the PSF.

A.3.4 Object and PSF Support Arrays. A single file containing two support arrays must be provided to IDA. The file contains the object support array followed immediately by the PSF support array in ASCII format. The two arrays must be the same size as the object, PSF and convolution image. The value in each pixel location contains either a "0" or "1", where one represents a pixel within the support region and zero represents a pixel outside the support region.

A.3.5 Output Log File. IDA requires a unique filename to write the output information. A name of an existing file will be rejected. This file will contain a summary of the parameters entered to run the program and a listing of the quantitative values of the different error terms at each iteration.

A.3.6 Maximum Iterations. The final input required for IDA to reconstruct an image is the maximum number of iterations allowed for the run. Choosing too few iterations is not a problem since the program has an option which allows the user to "restart" from the point at which the maximum number of iterations was reached by inputting the estimates obtained as the initial estimates and typing "1" for the restart parameter.

A.4 Available Options

After the information above has been entered, a series of additional questions regarding which error terms IDA will use to perform unconstrained minimization must be answered. The first question asks for either 0, 1, or 2 for the telescope aperture parameter. The second queries whether a restart is required, and the third asks for a Fourier spectrum parameter of 0, 1, or 2. If a non-circular convolution mask must be input, then a fourth question prompts the user for that information. The next few sections outline how to implement several different variations on the iterative deconvolution algorithm by answering the four questions listed below differently.

Q1. Input telescope aperture parameter (2,1,0):

Q2. Input 1 for a restart (else 0):

Q3. Input Fourier spectrum parameter (2,1,0):

Q4. Input 1 for non-circular convolution mask (else 0):

A.4.1 Basic Lane Method. The Lane method is the simplest form of the unconstrained minimization technique which IDA can perform. The Lane method, as discussed in Section 2.5.3, minimizes an error function containing only an image domain error term and a convolution error term. Since no *a priori* information is required, a "0" is entered for all four questions. However, if a restart is desired, then "1" would be the appropriate entry for the second question, Q2.

A.4.2 Band-limit Mask. As shown in experiment two, the addition of a band-limiting mask on the convolution error term significantly increases the ability of IDA to reconstruct images in the presence of noise. Utilization of the band-limit error occurs whenever the telescope aperture parameter, set in Q1, is non-zero. Entering either "1" or "2" for Q1 will require an additional data file. After all the questions are asked, IDA will prompt the user for the file containing cutoff frequency

information. If multiple measurements images of the same object are input, then IDA expects to find the cutoff frequency in pixels from the center for each unknown PSF. The program then creates a binary mask array for each PSF with a circular region of "1's" with a radius equal to that input from the cutoff frequency file. If non-circular masks are desired, then answering "1" to Q4 gives the user the opportunity to enter a filename containing the non-circular mask(s) used in conjunction with the convolution error term. To use the band-limit mask alone, similar to the runs made in experiment two, simply answer "1" to Q1 and "0" to the others.

A.4.3 Band-limit Error Term. The third term in Jefferies and Christou's error function is a band-limit error which minimizes the high frequency content of the PSF. This error term was used in experiment three with mixed results. IDA adds this term to the objective function whenever the telescope aperture parameter is "2". Thus, the current version of IDA does not allow for use of the band-limit error without employing the band-limit mask also. As explained above, entering "2" for Q1 will require additional information regarding the cutoff frequency of each PSF in pixels. The band-limit error term minimizes all pixel values in the OTF estimate outside of 1.39 times the input cutoff frequency (12).

As explained in Section 4.4, experiment three required that the band-limit error term be used for only the first few iterations, then IDA was restarted. In this case, the maximum iterations were set to 50 and the answers to Q1 through Q4 were 2, 0, 0, 0, respectively. After running 50 iterations with the band-limit error, IDA was restarted with a large maximum iteration value and the following values entered for Q1 through Q4: 1, 1, 0, 0. The first "1" makes use of the band-limit mask and the second "1" tells IDA that the input object and PSF estimates are from a previous run that did not attain a minimal objective function value.

A.4.4 Fourier Modulus Error. The third question (Q3) allows IDA to employ the fourth error term or the Fourier Modulus error. This error term was

not explored in this investigation since it requires explicit knowledge of the object attainable only through other image processing techniques. The Fourier spectrum parameter is set to zero unless use of the error term is desired. Entering "2" for Q3 requires input of both the real and complex portions of the object spectrum. Simply entering "1" for Q3 informs IDA that Fourier modulus information will be entered. Additionally, use of the Fourier modulus error term requires the input of a "signal-to-noise" filter as explained in Jefferies and Christou [1993], the wavelength of the observations, the diameter of the aperture, and image scale in milli-arcseconds/pixel. More information can be found regarding the Fourier modulus error in Jefferies and Christou (12).

A.5 Modifications and Recompile

Since the code supplied by Jefferies and Christou is in FORTRAN, array size parameters must be set prior to compilation of the code. To facilitate processing of images having different sizes or support areas, a header file containing all of the applicable parameters for processing of a single image or set of images may require modification each time IDA is run. This header file sets the number of PSFs that will be required for a single run, the number of pixels on one side of the image array, the number of variables IDA will have to minimize in the objective function, and the tolerance at which the change in the error function value must reach before a minimum value is found. Each of the parameters are explained in detail below.

A.5.1 Number of PSFs. The number of PSFs or *npsf* must be set to "1" for a single measurement, object and PSF combination. However, if multiple realizations of the same object are input into IDA, then the total number of different PSF estimates which IDA will have to make at each iteration is the value for *npsf*.

A.5.2 Number of Pixels. IDA requires that all arrays input into the program (measurements, estimates, support, etc.) have the same size, $npix \times npix$,

where *npix* represents the number of pixels in either one row or one column of the square array.

A.5.3 Number of Variables. This parameter gives rise to modifying the header file and recompiling IDA even for different images of the same array size. The number of variables, *nvar*, equals the total number of non-zero pixels within *both* the object and PSF support arrays. Therefore, any time the support size changes, *nvar* changes and IDA must be recompiled. For the four different images used in this investigation, a copy of the header file was kept in each of four different files with the appropriate values for *nvar*. When a run was required for image B for instance, the header for image B was copied into the header file using the following UNIX command: *cp headerB IDA.h*. Then, compiling was accomplished through a "make-file" supplied by Stuart Jefferies by issuing this command: *make IDA.FITS*.

A.5.4 Tolerance. The tolerance, *tol*, represents a very small amount of change in the value of the error function. Once the amount of change reaches the tolerance, then it is assumed that the conjugate gradient minimization routine has found a local minimum and further iterations cease.

A.6 Summary

This appendix provides information regarding the use of the IDA FORTRAN code provided by Stuart Jefferies and modified for use in this investigation. A brief explanation of how the algorithm is implemented was presented along with explicit details regarding the use of IDA to reconstruct images. The program allows a user to utilize many different means of implementing the unconstrained minimization technique to solve the blind deconvolution problem. It is hoped that this appendix will allow wider use of IDA to process blurred images and that future research can proceed more efficiently by using the documentation presented here. Copies of the

IDA code used in this study can be obtained through Major Michael Roggemann,
Air Force Institute of Technology/ENP, Wright-Patterson AFB, OH 45433-6583.

Appendix B. Simulated Images

B.1 True Objects and Noise-Free Images

This section contains a visual representation of the four objects used in experiments one, two and three. Each object is a 64×64 array with one or two point sources within each array. Three of the objects contain binary stars with an intensity ratio of 1:0.7. Immediately after each "true" object appears an image resulting from the convolution of the object with a single PSF shown in Figure B.9.

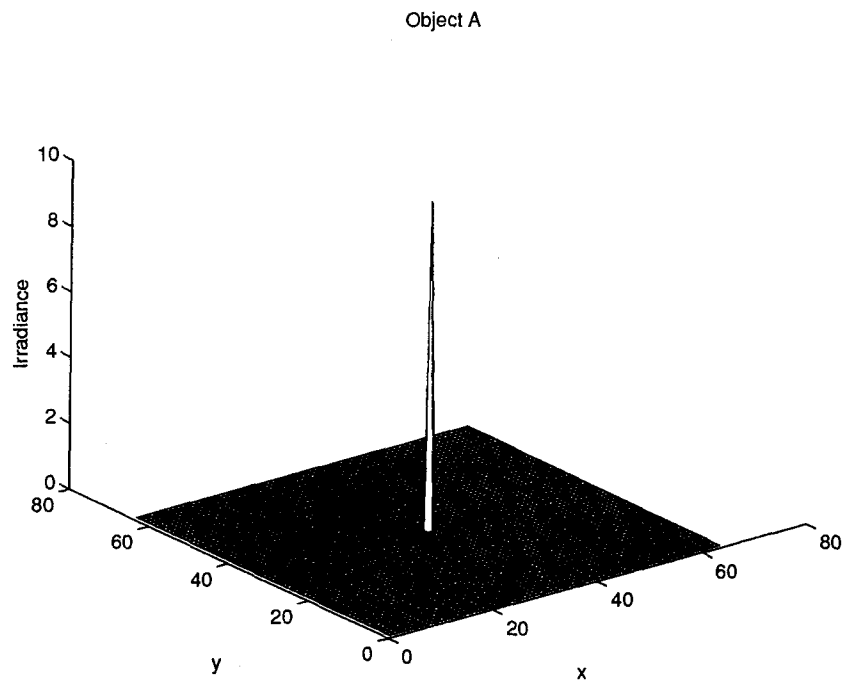


Figure B.1 Object A contains a single point source centered in the array.

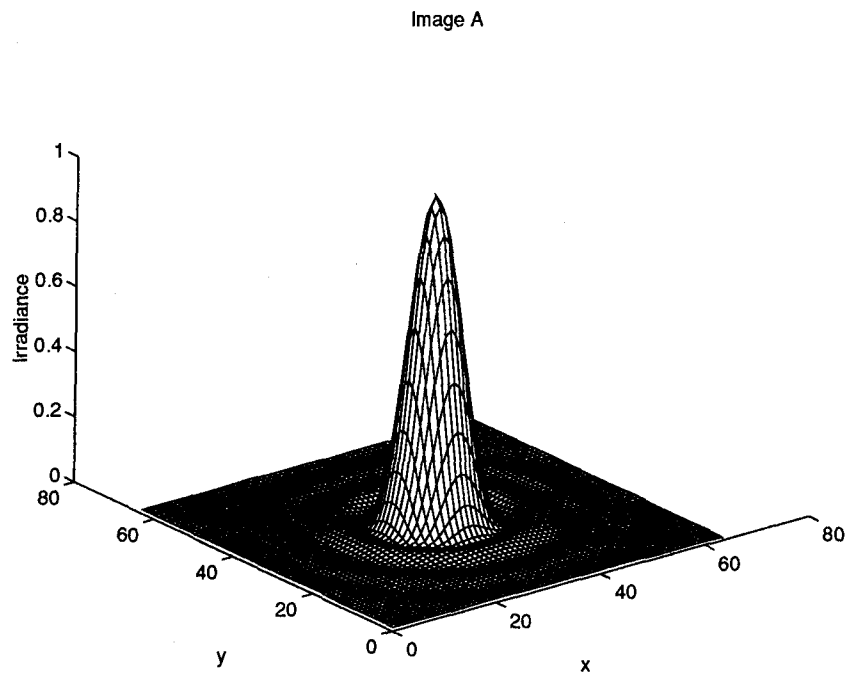


Figure B.2 Image A represents the convolution of Object A with the PSF in Figure B.9.

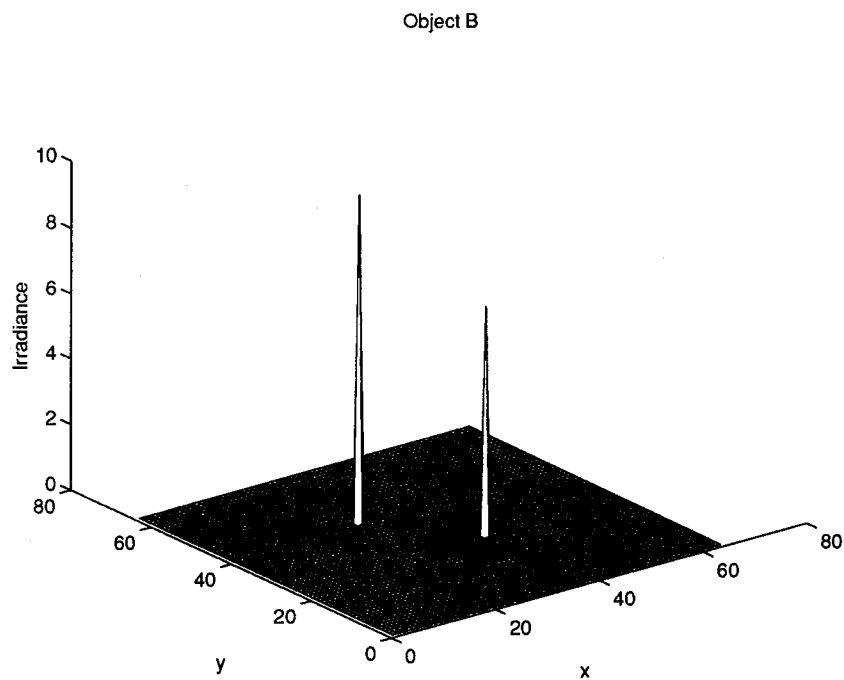


Figure B.3 Object B contains two point sources separated by 1.81 times the blur radius.

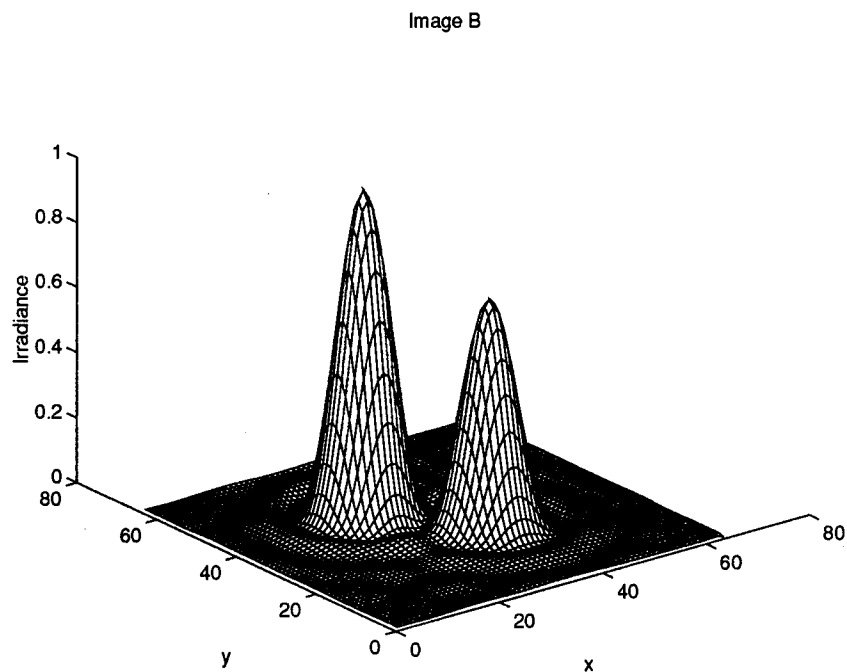


Figure B.4 Image B represents the convolution of Object B with the PSF in Figure B.9.

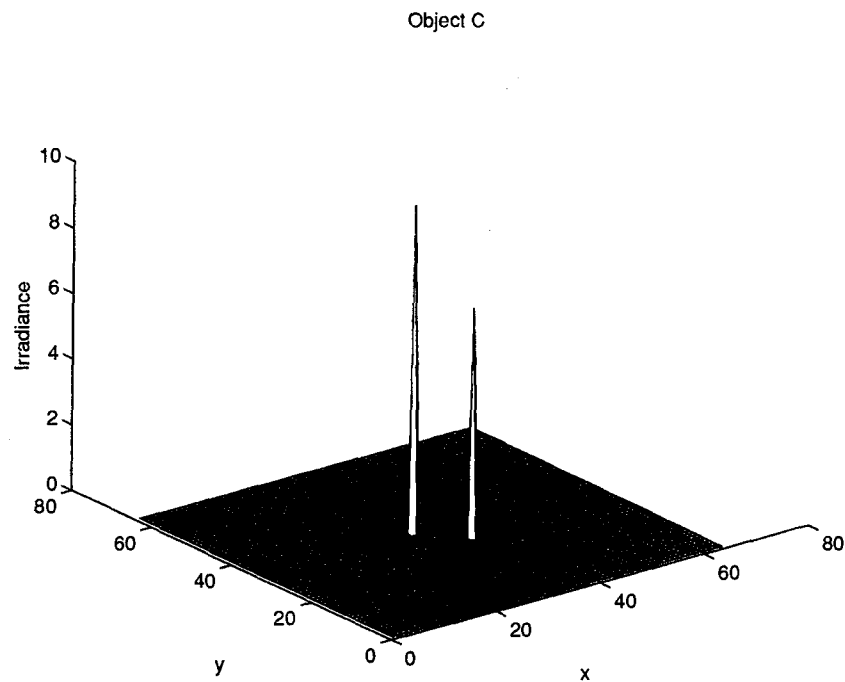


Figure B.5 Object C contains two point sources separated by 0.84 times the blur radius.

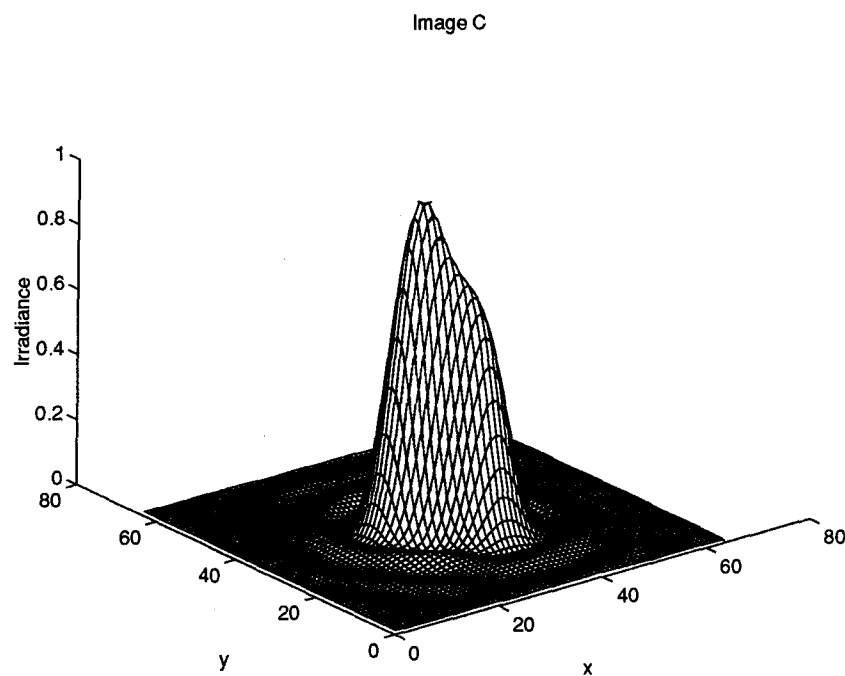


Figure B.6 Image C represents the convolution of Object C with the PSF in Figure B.9.

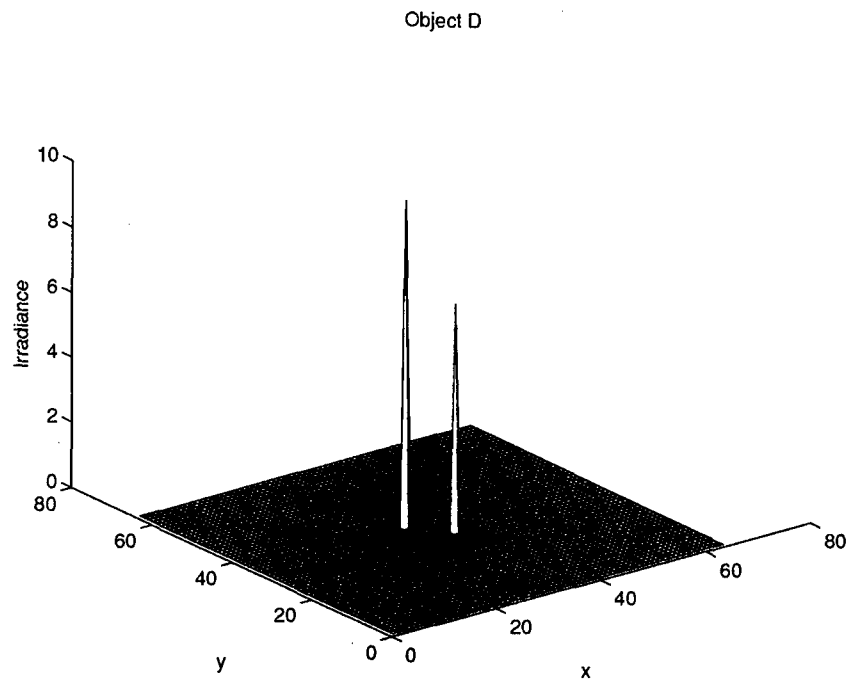


Figure B.7 Object D contains two point sources separated by 0.71 times the blur radius.

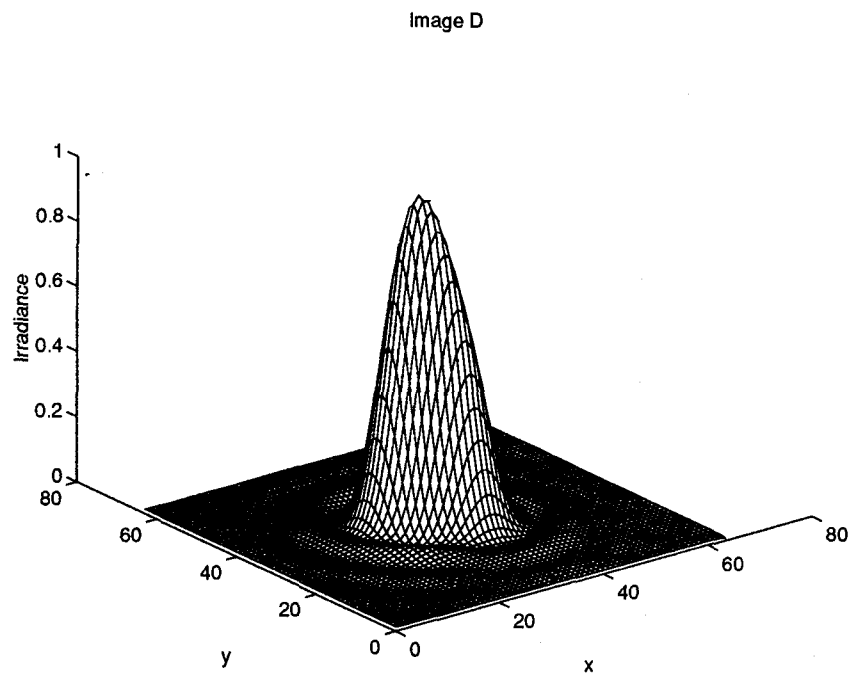


Figure B.8 Image D represents the convolution of Object D with the PSF in Figure B.9.

B.2 True Point Spread Function

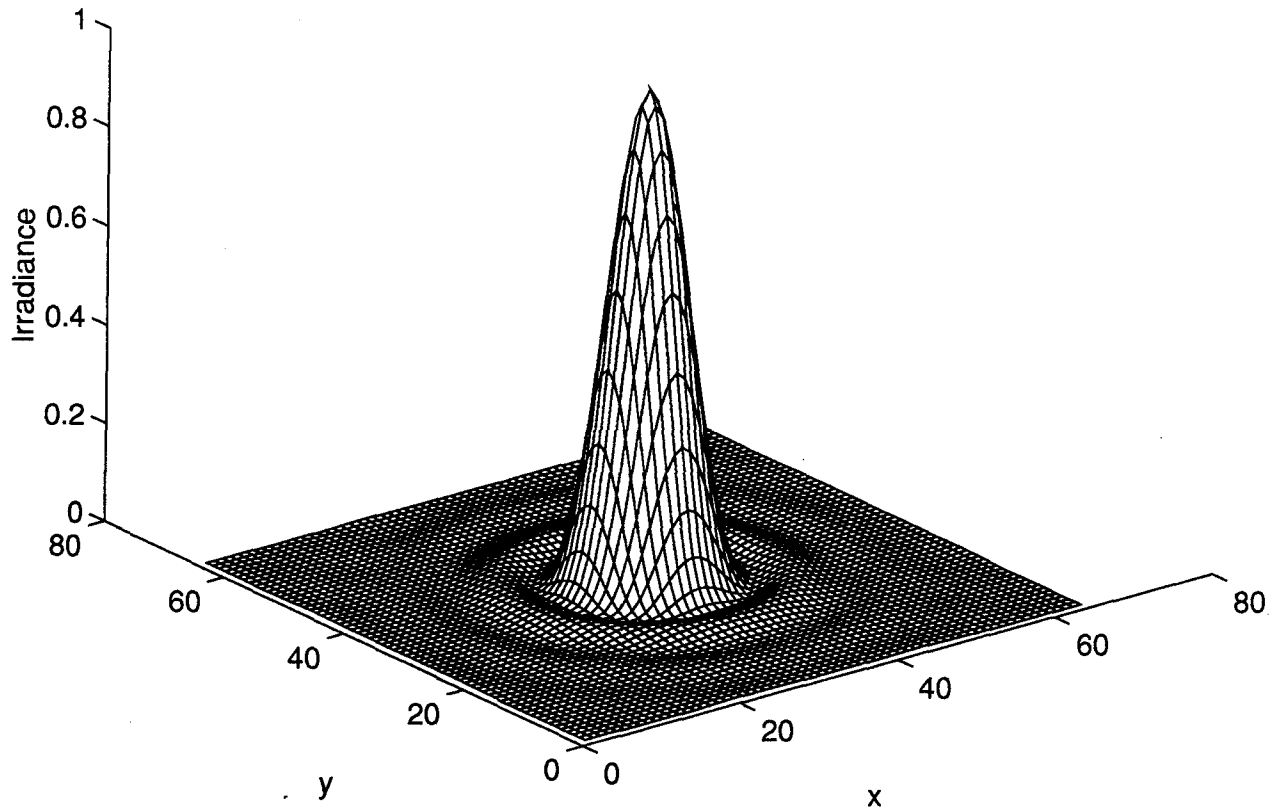


Figure B.9 The true PSF was used to generate the blurred images previously shown. The iterative deconvolution algorithm attempts to estimate this PSF along with the applicable object for each blurred image. The blur radius for the PSF shown above is 11 pixels representing the spatial distance from the center of the array to the first zero.

B.3 Photon Limited Images

Image A (100,000 photo events)

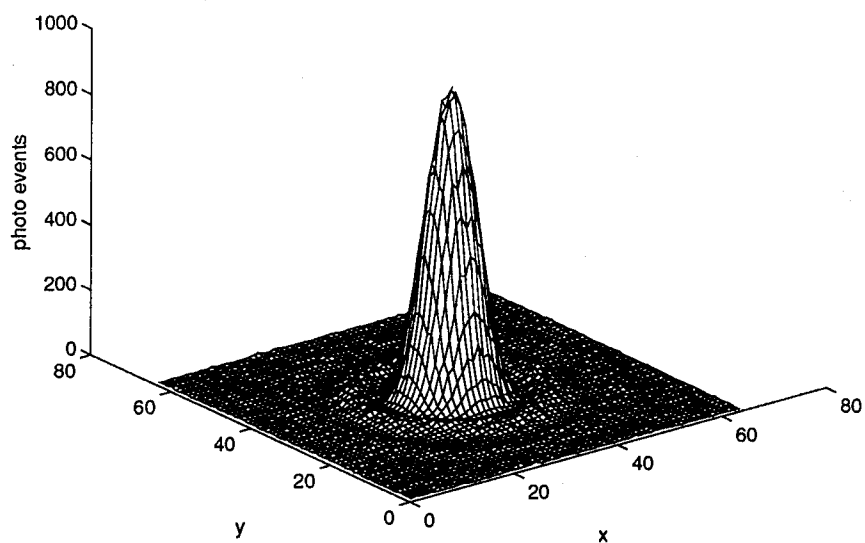


Figure B.10 The image above represents a short-exposure of Image A containing only 100,000 photo events ($\bar{K} = 10^5$).

Image A (10,000 photo events)

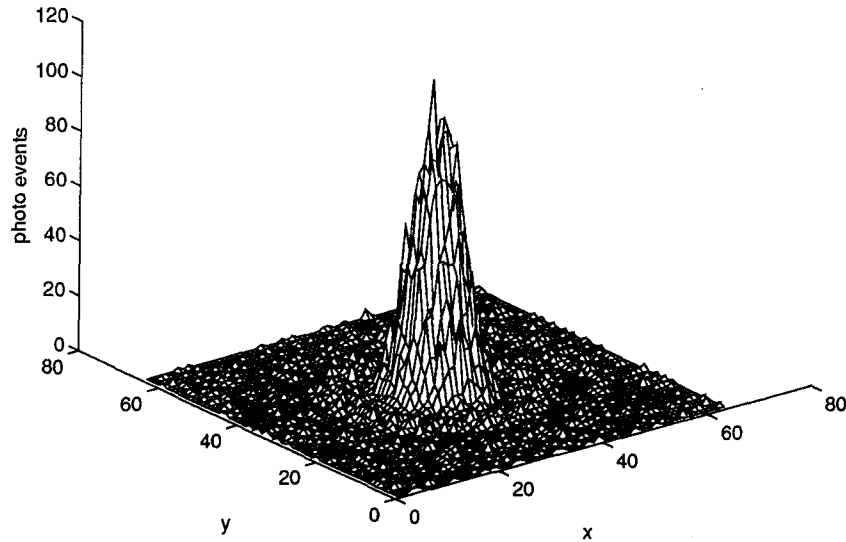


Figure B.11 The image above represents a short-exposure of Image A containing only 10,000 photo events ($\bar{K} = 10^4$).

Image A (5,000 photo events)

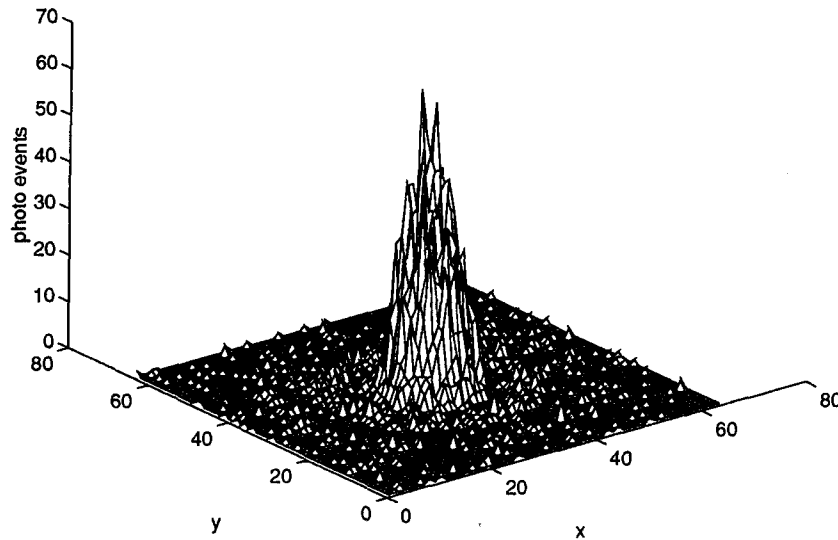


Figure B.12 The image above represents a short-exposure of Image A containing only 5,000 photo events ($\bar{K} = 5 \cdot 10^3$).

Image B (100,000 photo events)

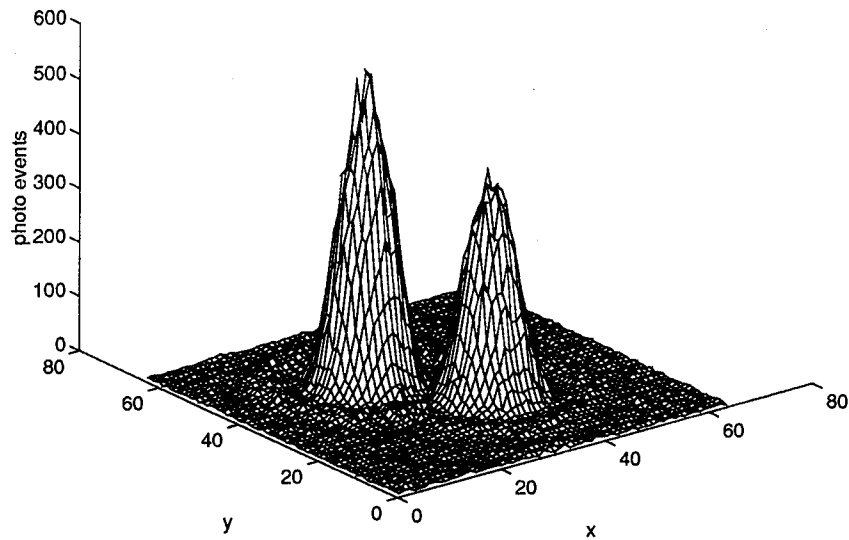


Figure B.13 The image above represents a short-exposure of Image B containing only 100,000 photo events ($\bar{K} = 10^5$).

Image B (10,000 photo events)

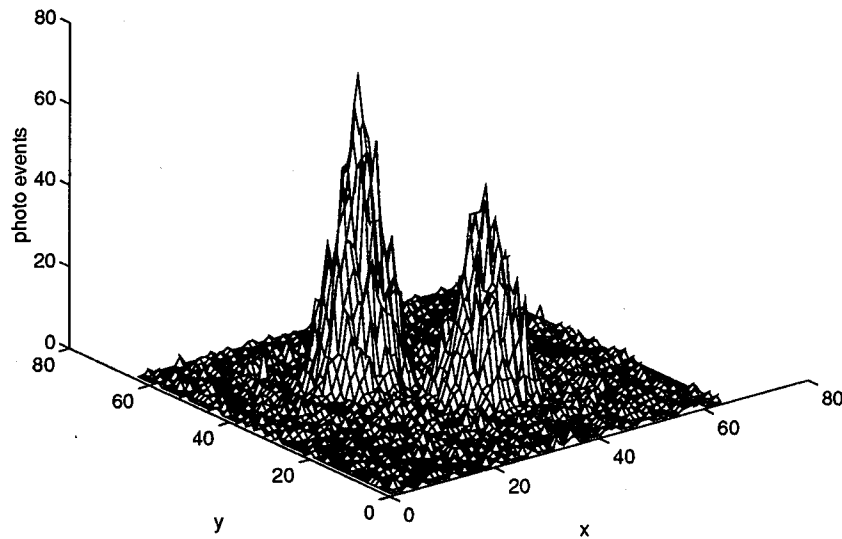


Figure B.14 The image above represents a short-exposure of Image B containing only 10,000 photo events ($\bar{K} = 10^4$).

Image B (5,000 photo events)

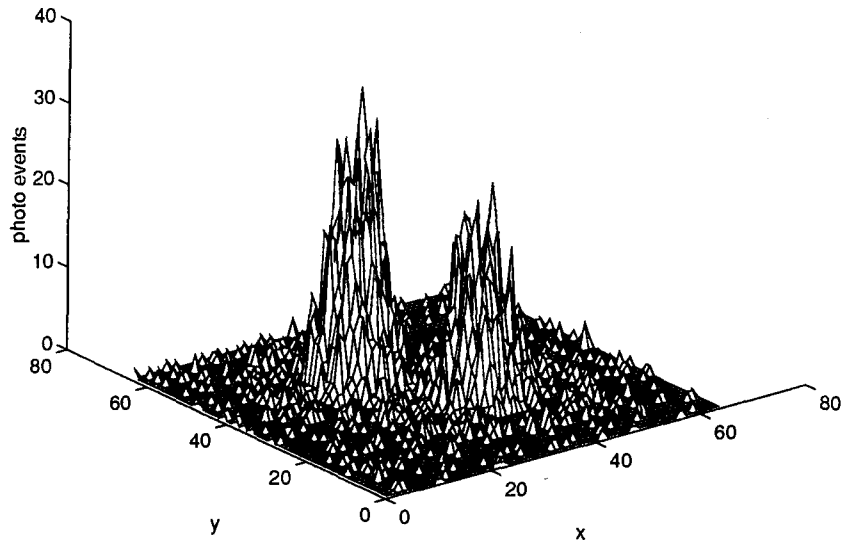


Figure B.15 The image above represents a short-exposure of Image B containing only 5,000 photo events ($\bar{K} = 5 \cdot 10^3$).

Image C (100,000 photo events)

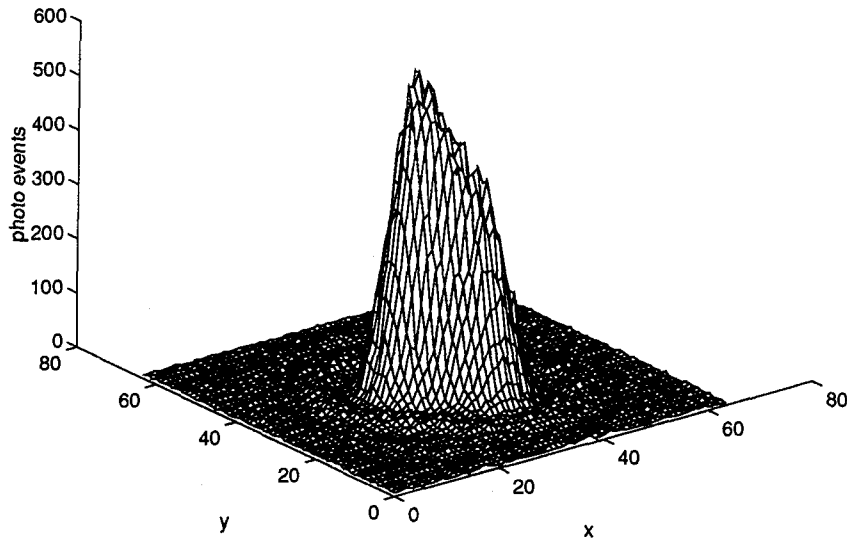


Figure B.16 The image above represents a short-exposure of Image C containing only 100,000 photo events ($\bar{K} = 10^5$).

Image C (10,000 photo events)

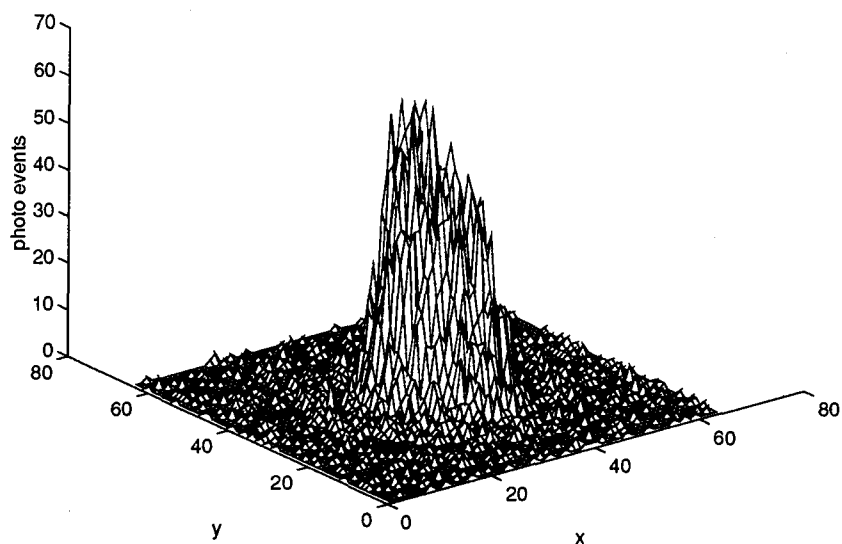


Figure B.17 The image above represents a short-exposure of Image C containing only 10,000 photo events ($\bar{K} = 10^4$).

Image C (5,000 photo events)

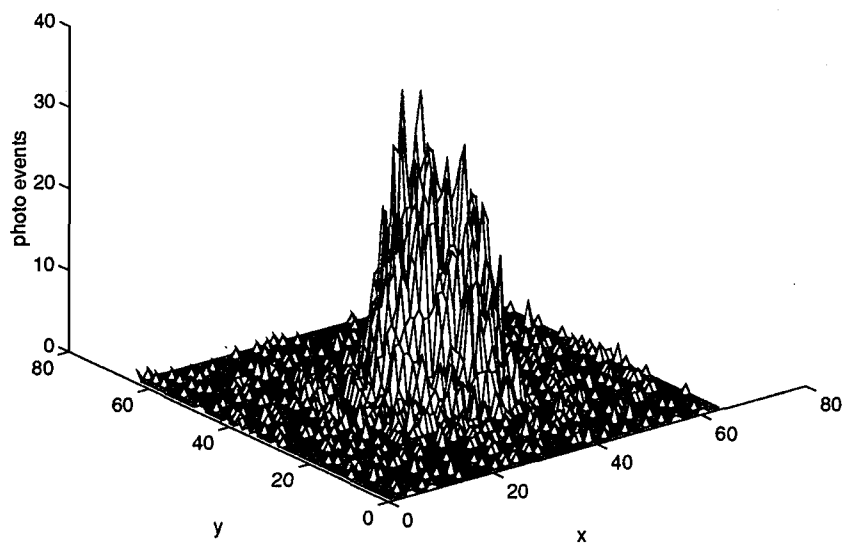


Figure B.18 The image above represents a short-exposure of Image C containing only 5,000 photo events ($\bar{K} = 5 \cdot 10^3$).

Image D (100,000 photo events)

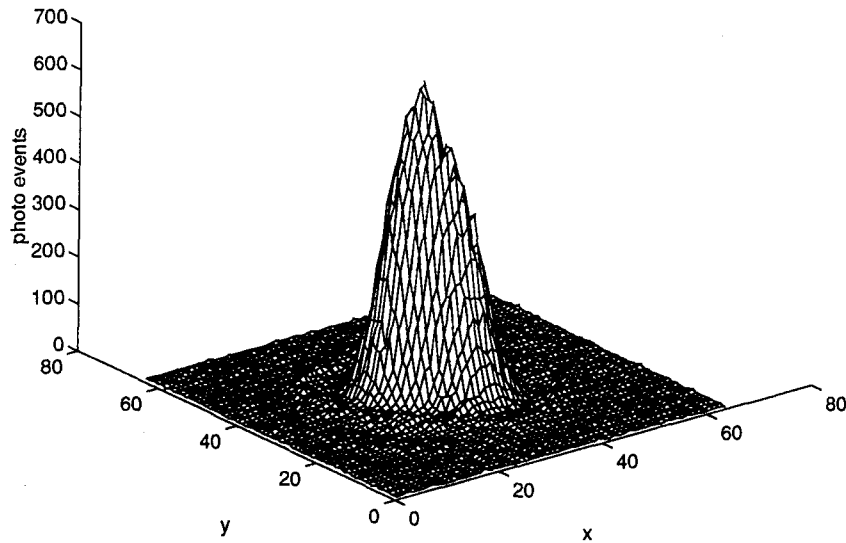


Figure B.19 The image above represents a short-exposure of Image D containing only 100,000 photo events ($\bar{K} = 10^5$).

Image D (10,000 photo events)

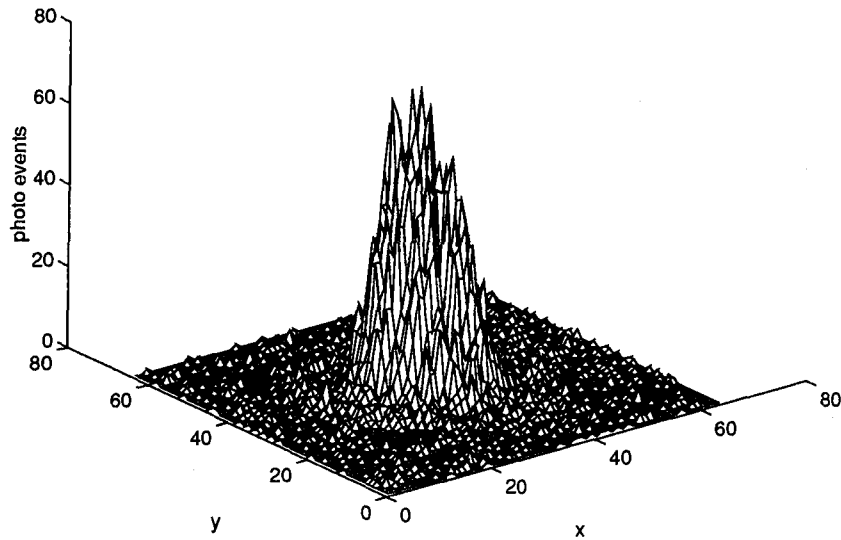


Figure B.20 The image above represents a short-exposure of Image D containing only 10,000 photo events ($\bar{K} = 10^4$).

Image D (5,000 photo events)

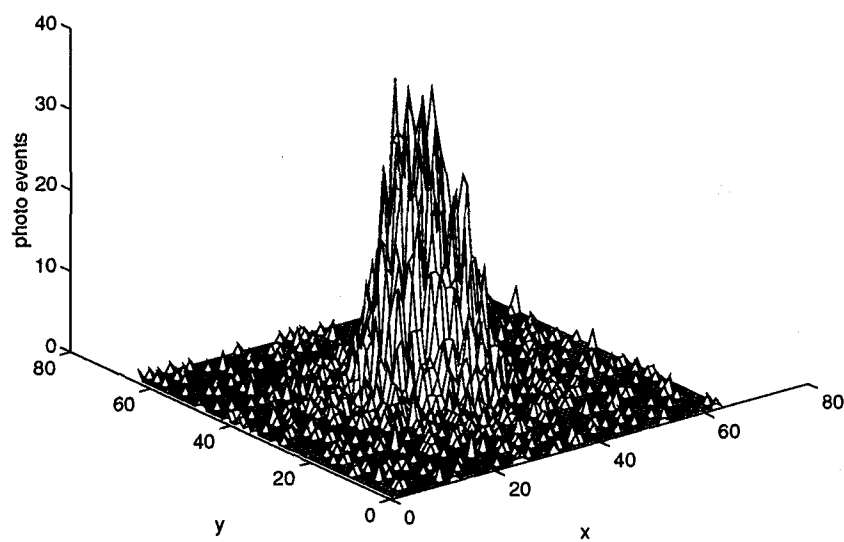


Figure B.21 The image above represents a short-exposure of Image D containing only 5,000 photo events ($\bar{K} = 5 \cdot 10^3$).

Appendix C. Experiment 1 Results

The first experiment tests the unconstrained minimization approach to blind deconvolution for noise-free blurred images. Results are presented for the four images shown in Figures B.2, B.4, B.6 and B.8 using three different support regions. The support regions correspond to the first, second and third zero of the true PSF as explained in Section 3.7.2. The data presented in this appendix refer to the smallest support size (corresponding to the first zero) as support region 1, the medium-sized support as support region 2 and the largest as support region 3. A ring of “spikes” appear on the edge of the support region for each object estimate. This phenomenon seems to be a function of the algorithm, and the amplitude of the spikes decreases with larger support regions. As presented in Chapter 4, the best results are obtained using support region 2 for these images.

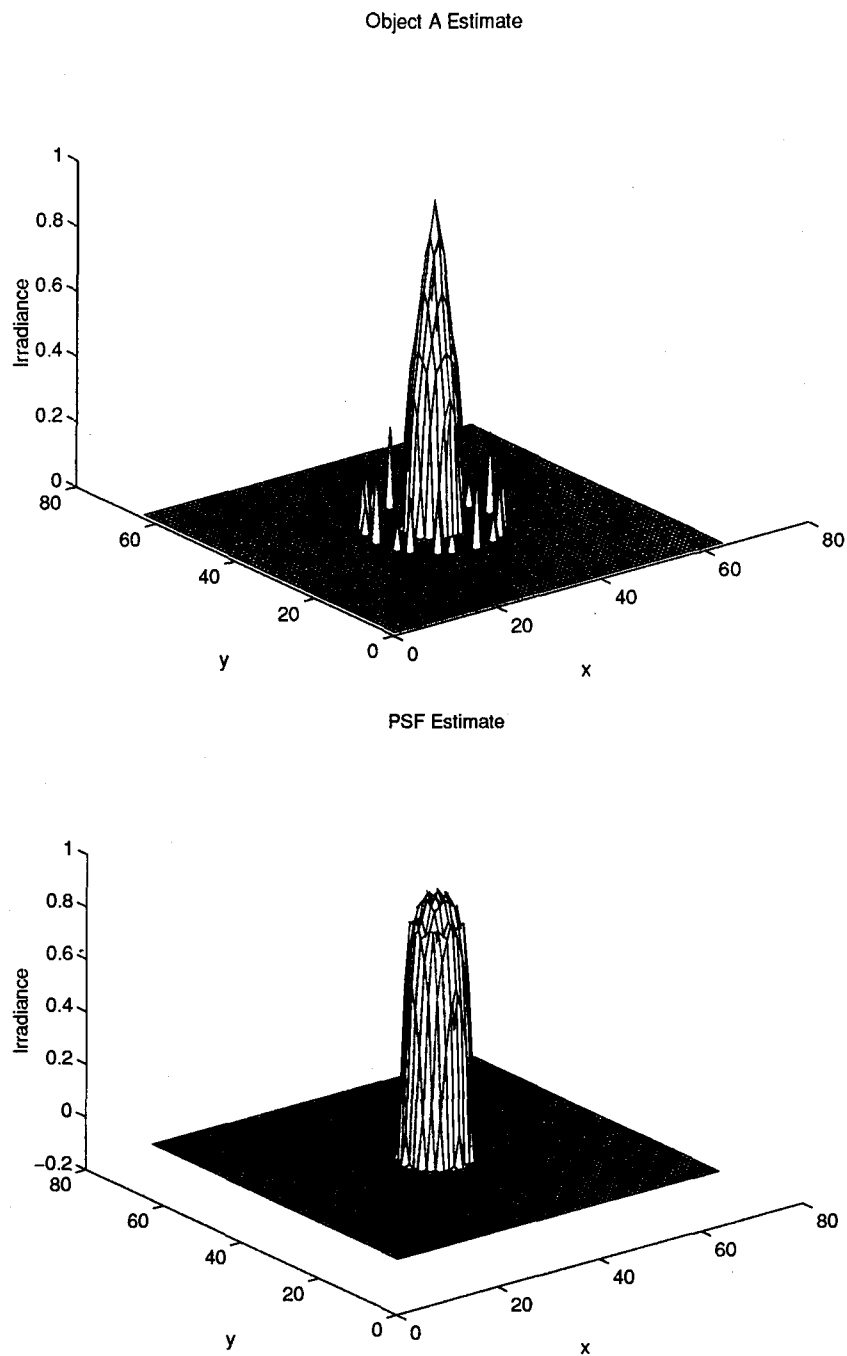


Figure C.1 Shown above are the object and PSF estimates produced by unconstrained minimization from noise-free Image A and utilizing support region 1.

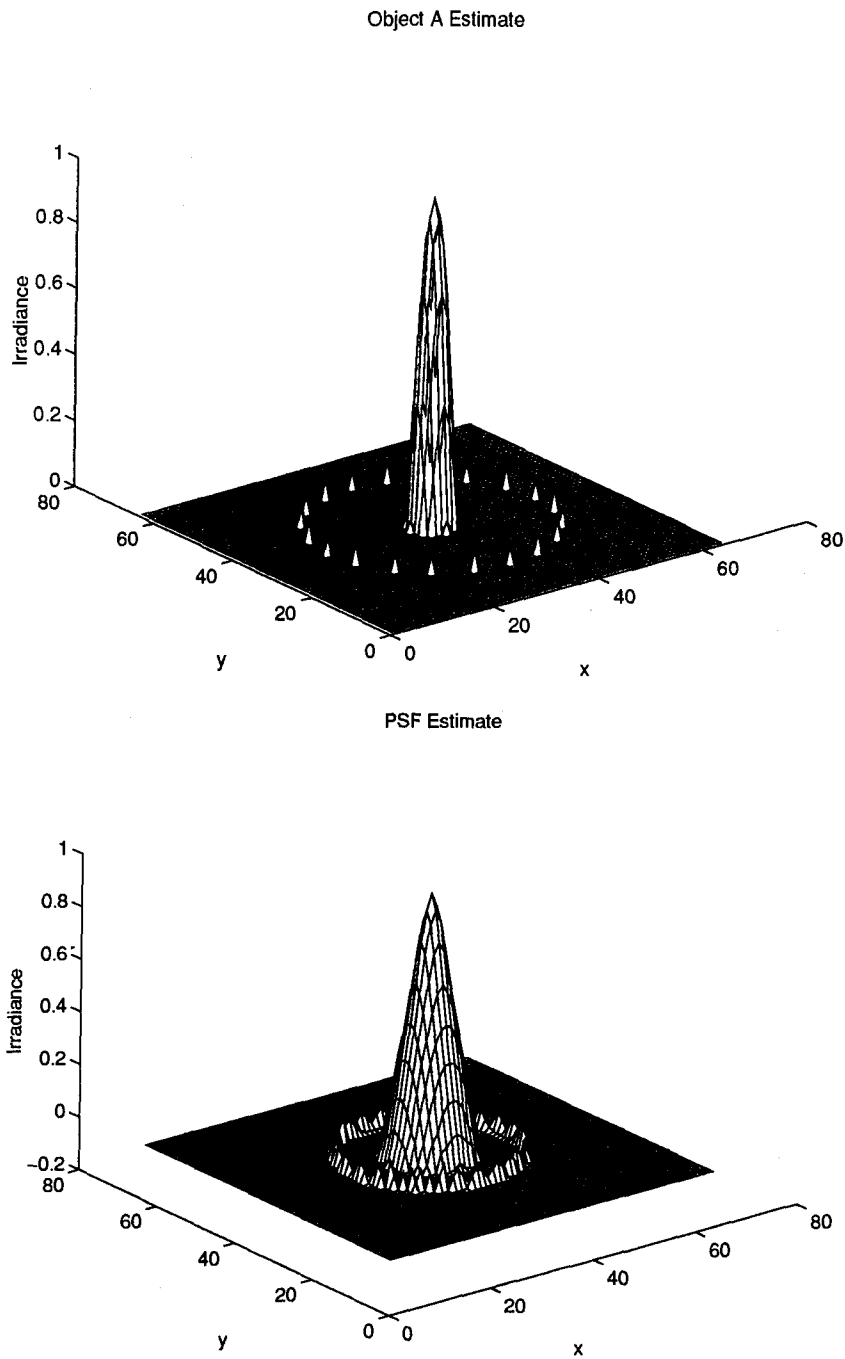


Figure C.2 Shown above are the object and PSF estimates produced by unconstrained minimization from noise-free Image A and utilizing support region 2.

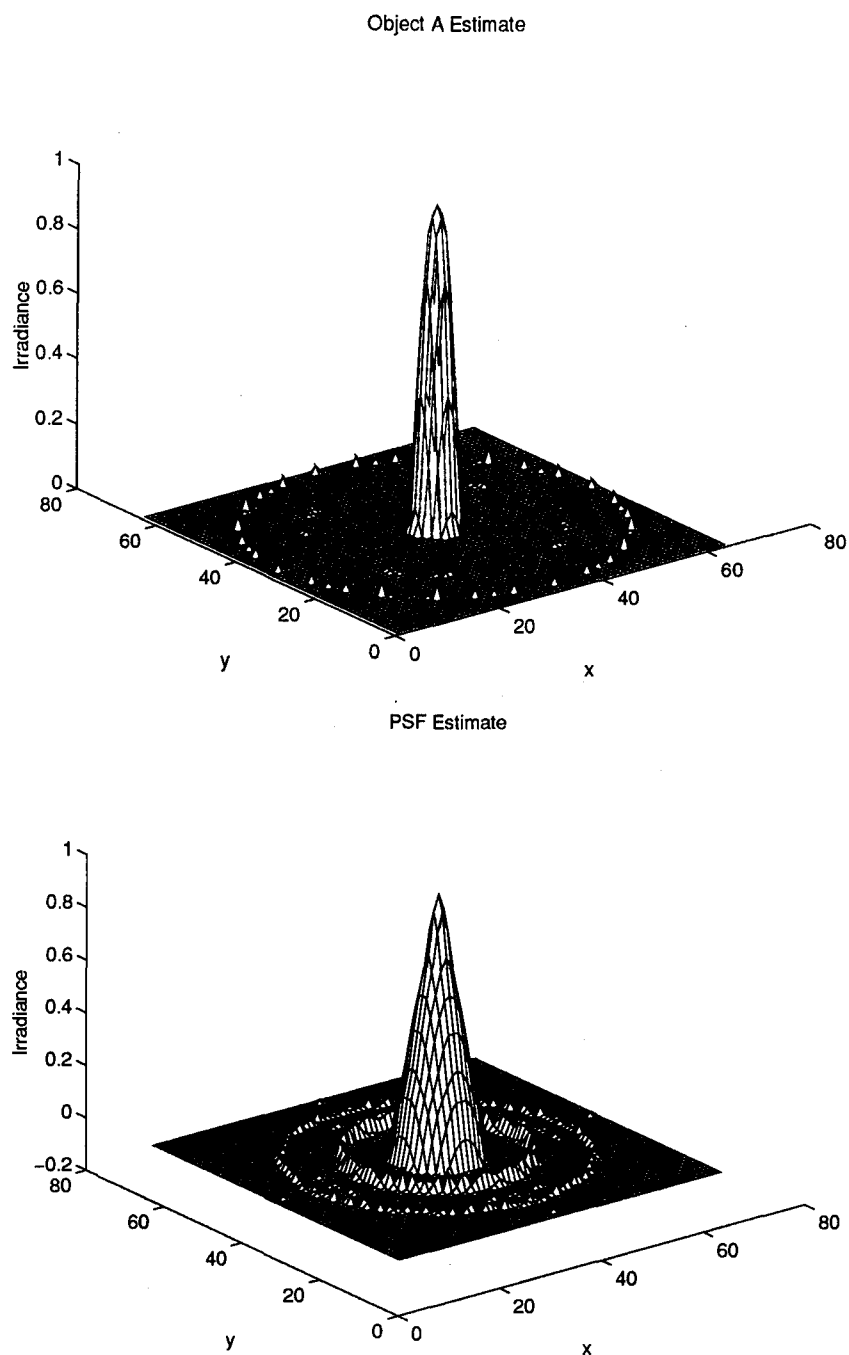


Figure C.3 Shown above are the object and PSF estimates produced by unconstrained minimization from noise-free Image A and utilizing support region 3.

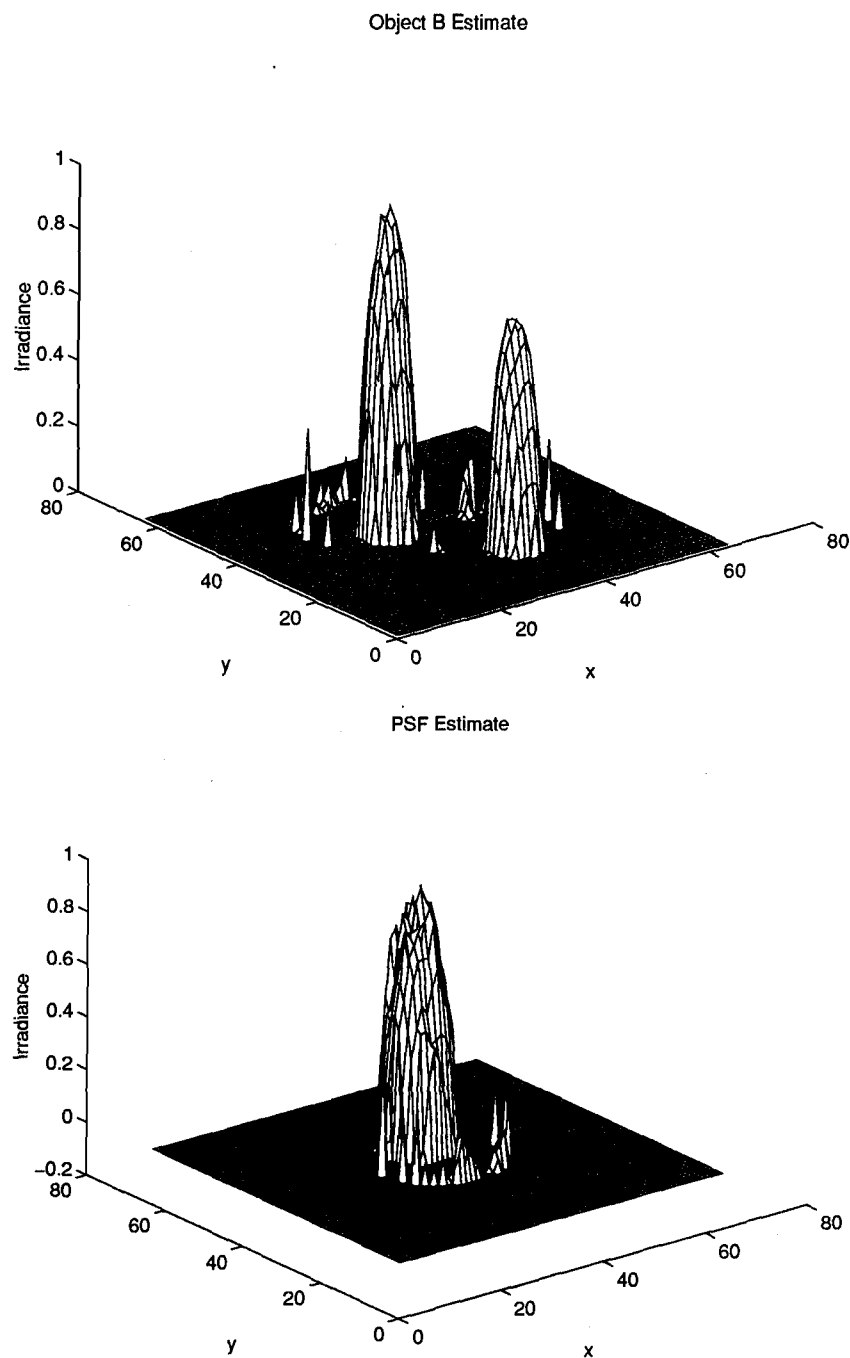


Figure C.4 Shown above are the object and PSF estimates produced by unconstrained minimization from noise-free Image B and utilizing support region 1.

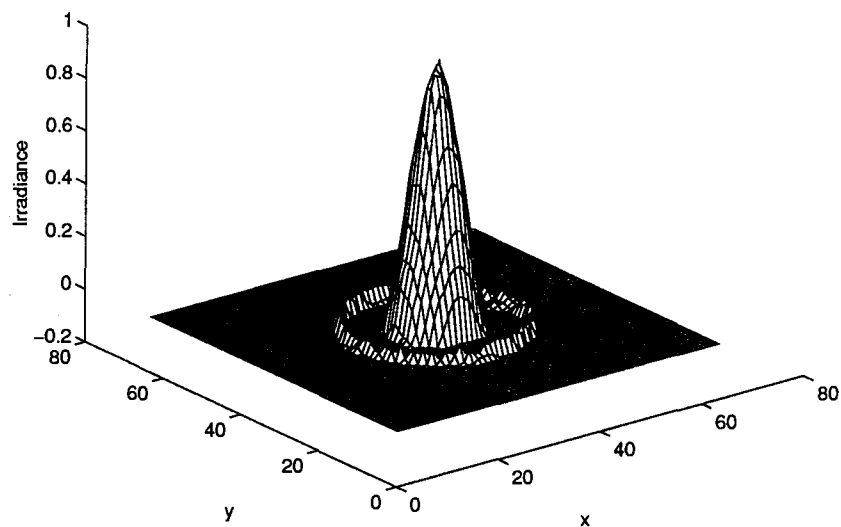
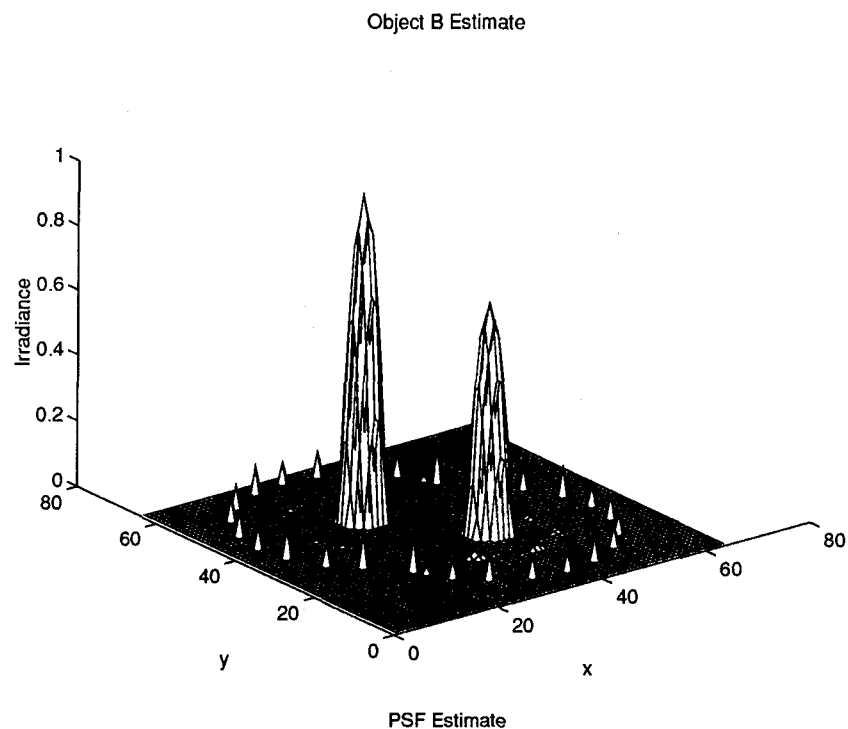


Figure C.5 Shown above are the object and PSF estimates produced by unconstrained minimization from noise-free Image B and utilizing support region 2.

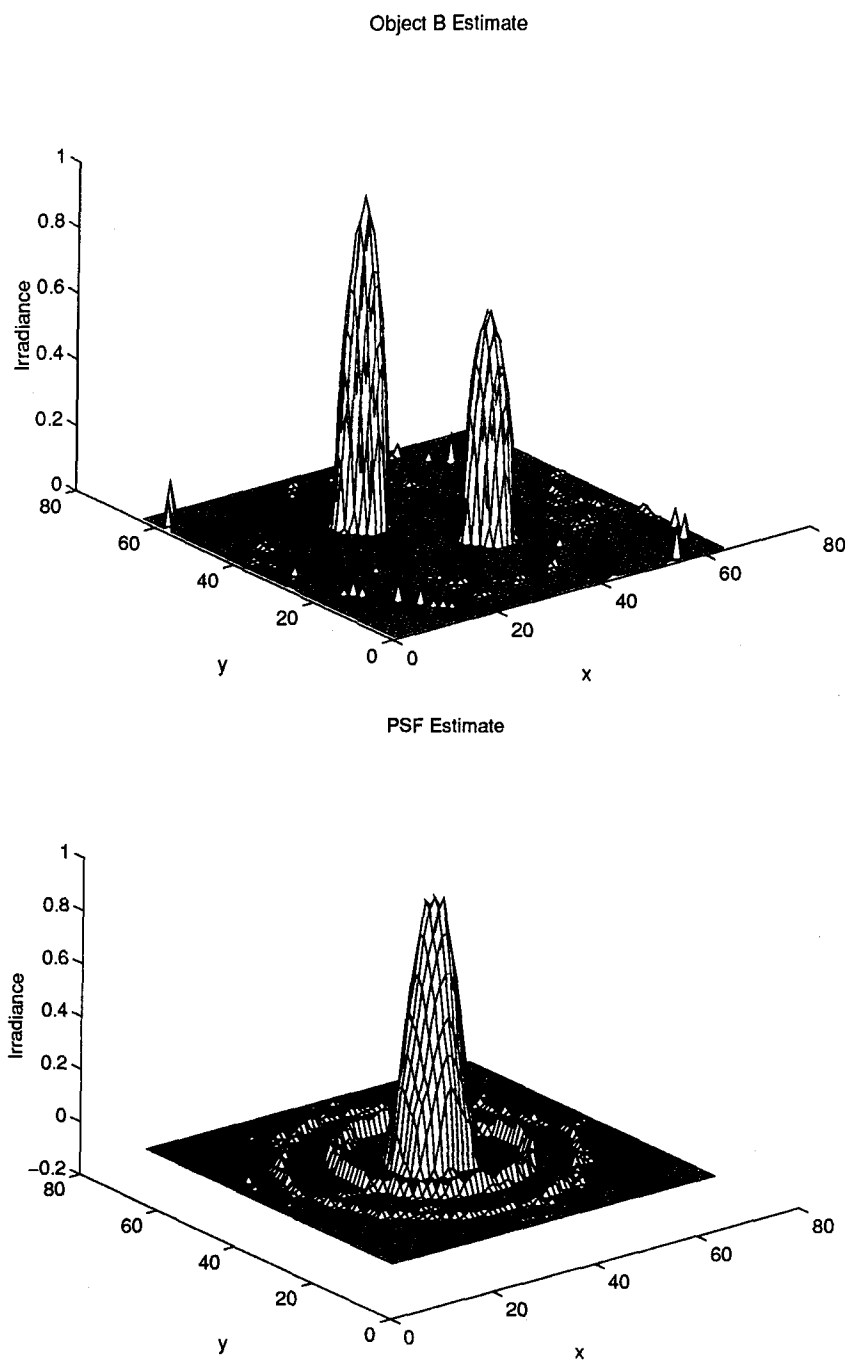
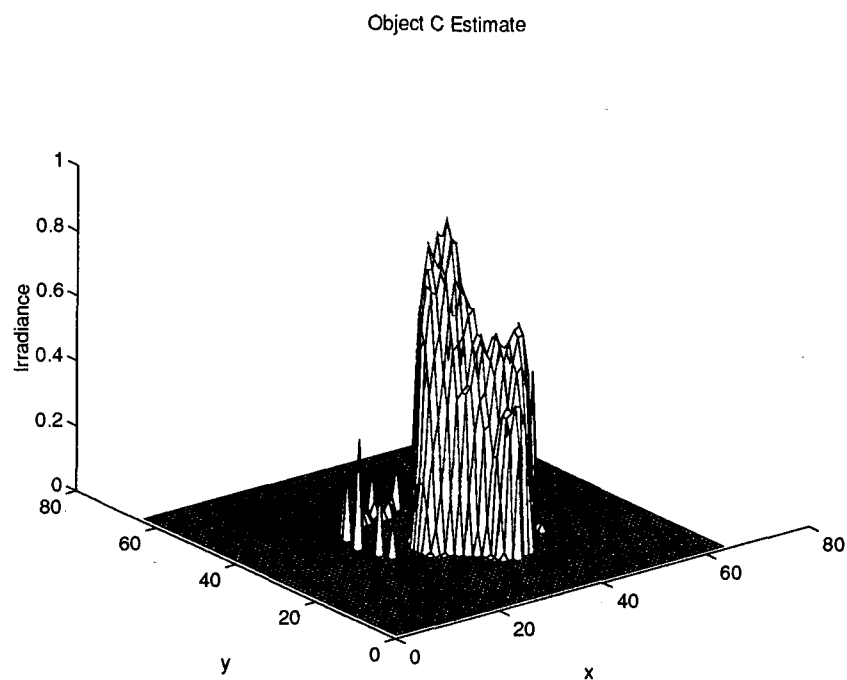


Figure C.6 Shown above are the object and PSF estimates produced by unconstrained minimization from noise-free Image B and utilizing support region 3.



PSF Estimate

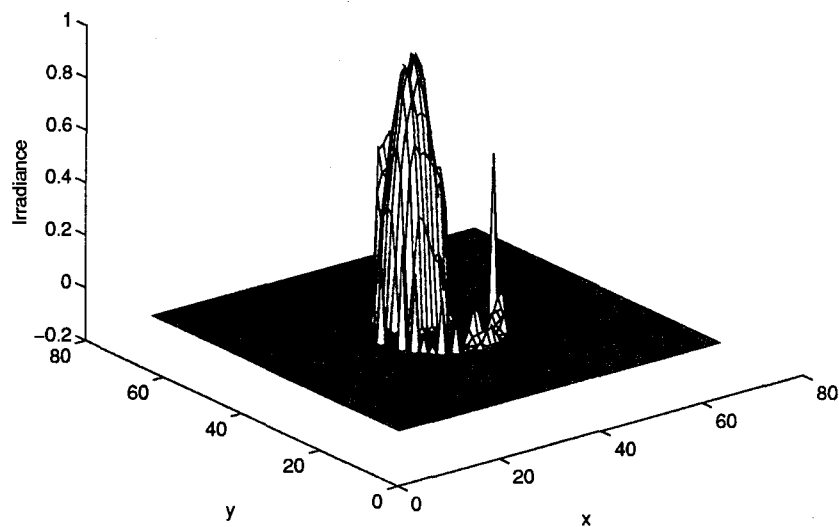


Figure C.7 Shown above are the object and PSF estimates produced by unconstrained minimization from noise-free Image C and utilizing support region 1.

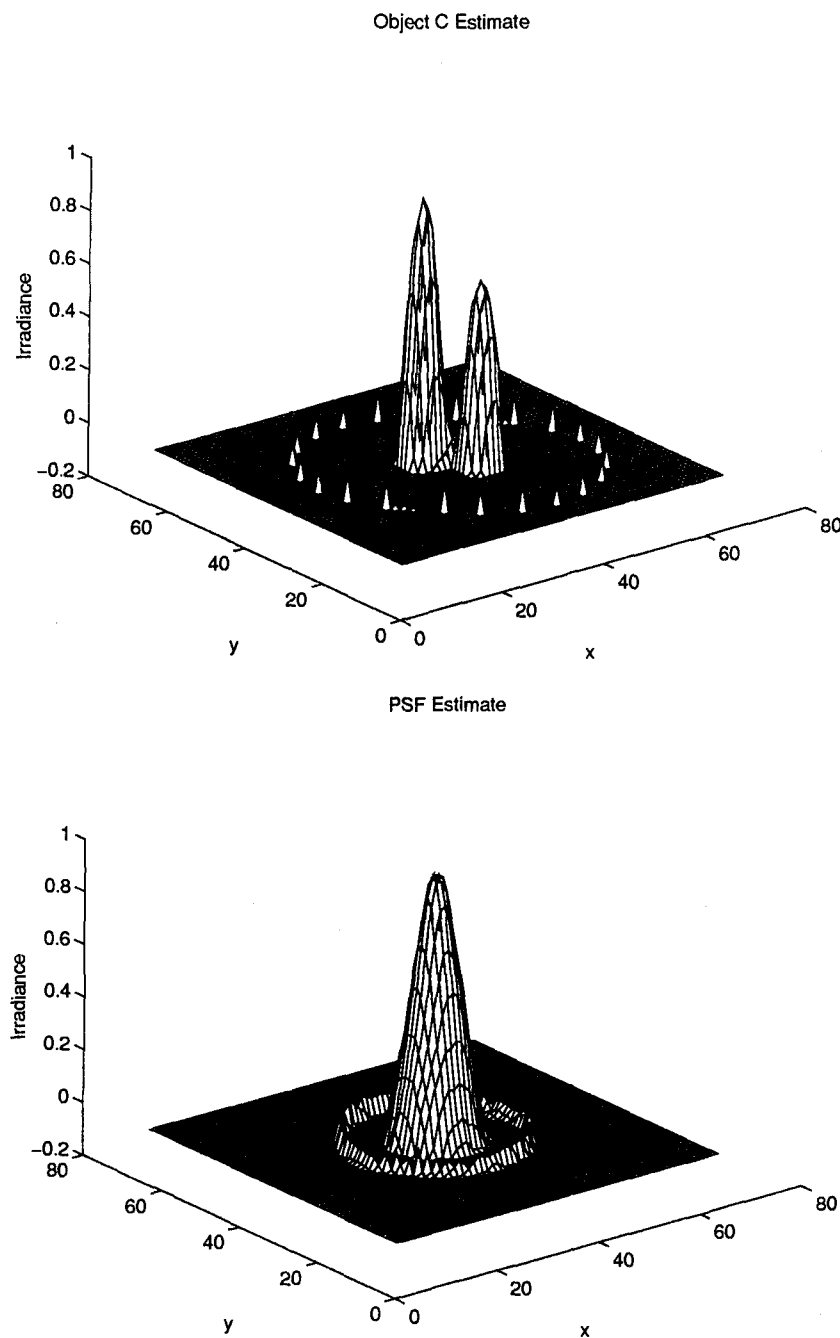


Figure C.8 Shown above are the object and PSF estimates produced by unconstrained minimization from noise-free Image C and utilizing support region 2.

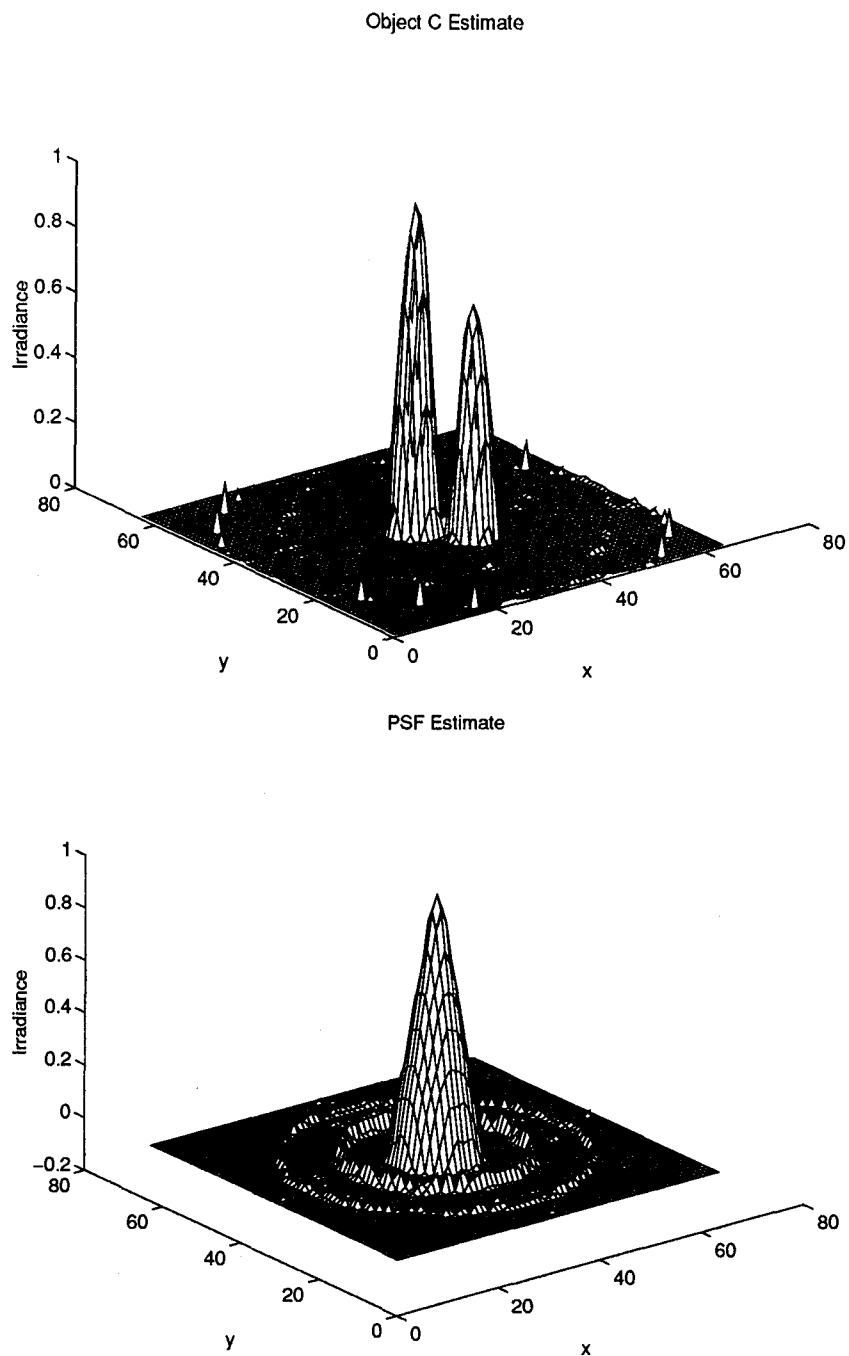


Figure C.9 Shown above are the object and PSF estimates produced by unconstrained minimization from noise-free Image C and utilizing support region 3.

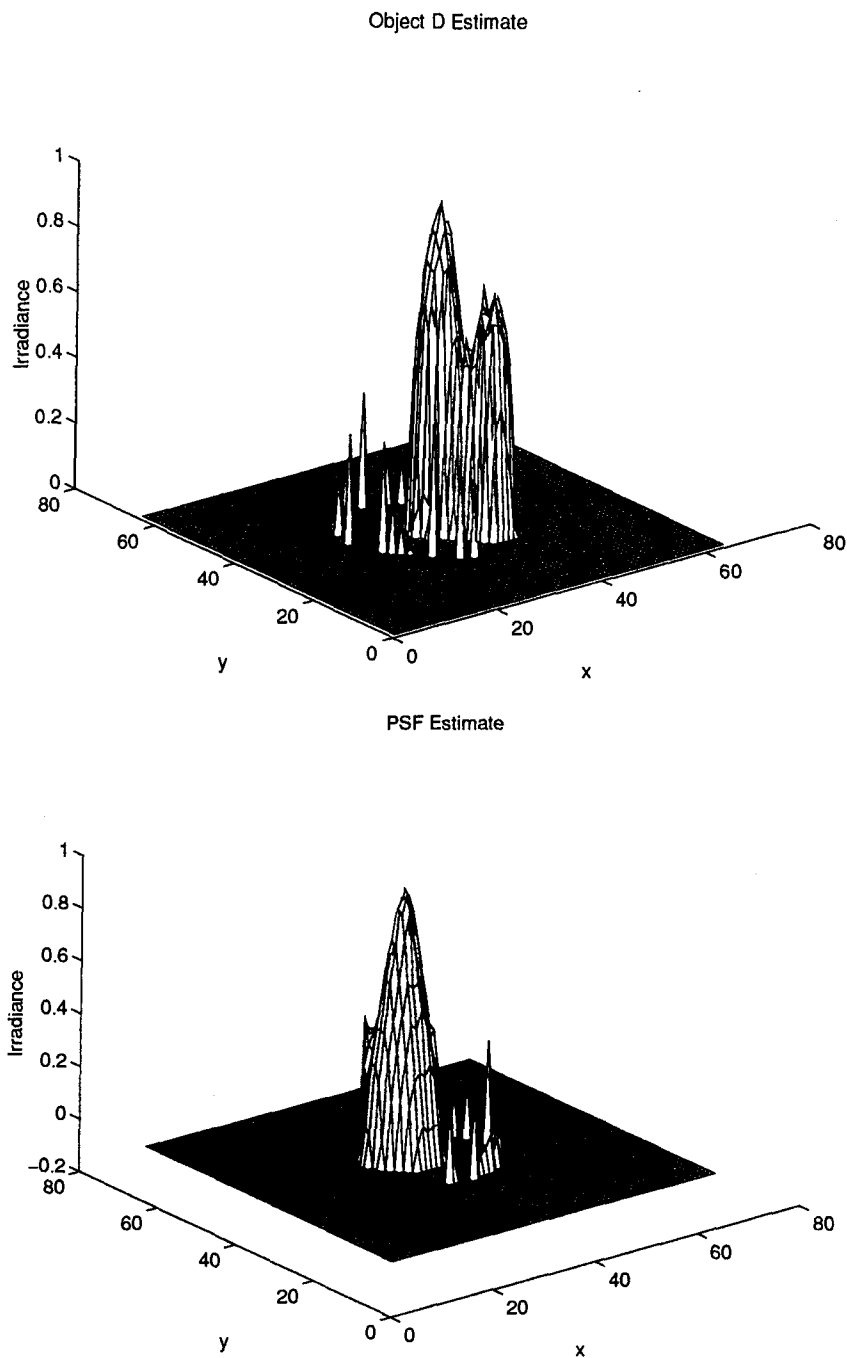


Figure C.10 Shown above are the object and PSF estimates produced by unconstrained minimization from noise-free Image D and utilizing support region 1.

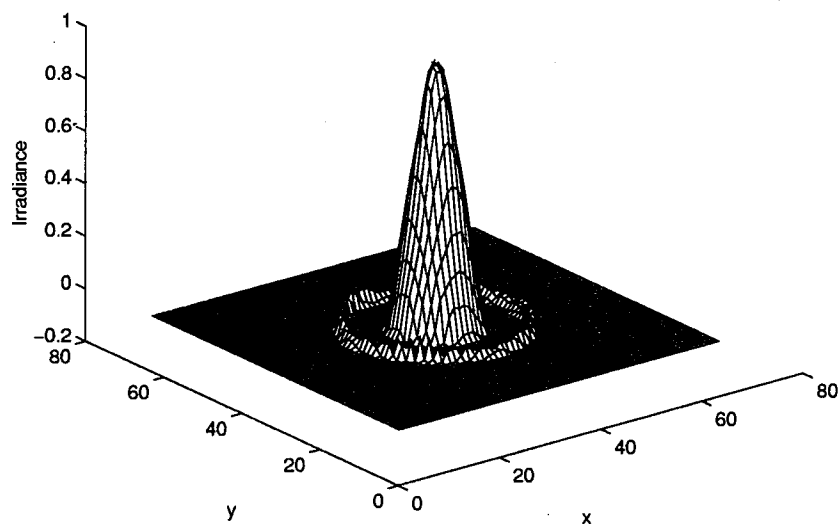
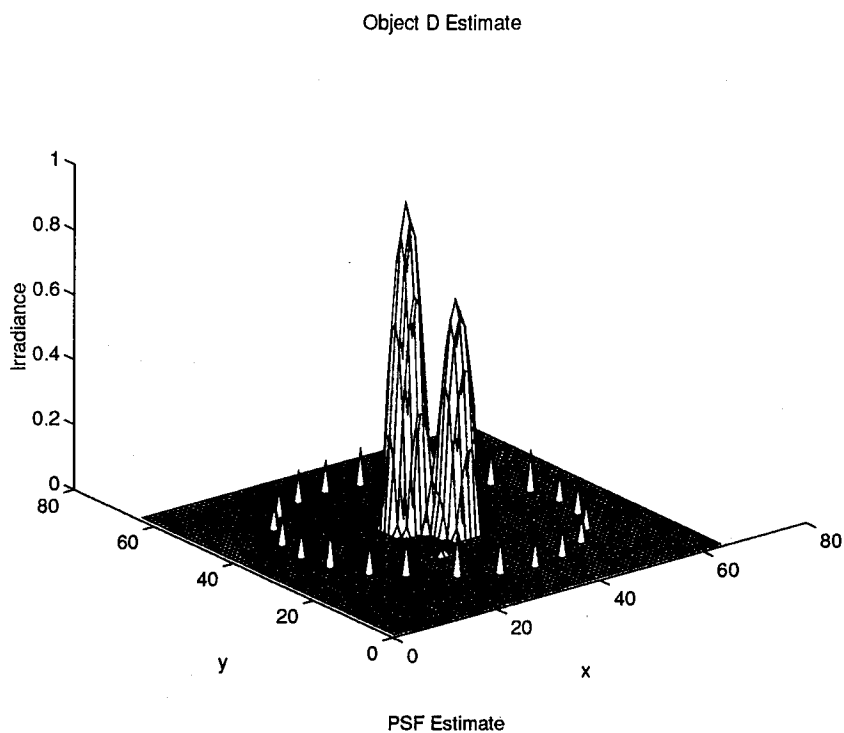


Figure C.11 Shown above are the object and PSF estimates produced by unconstrained minimization from noise-free Image D and utilizing support region 2.

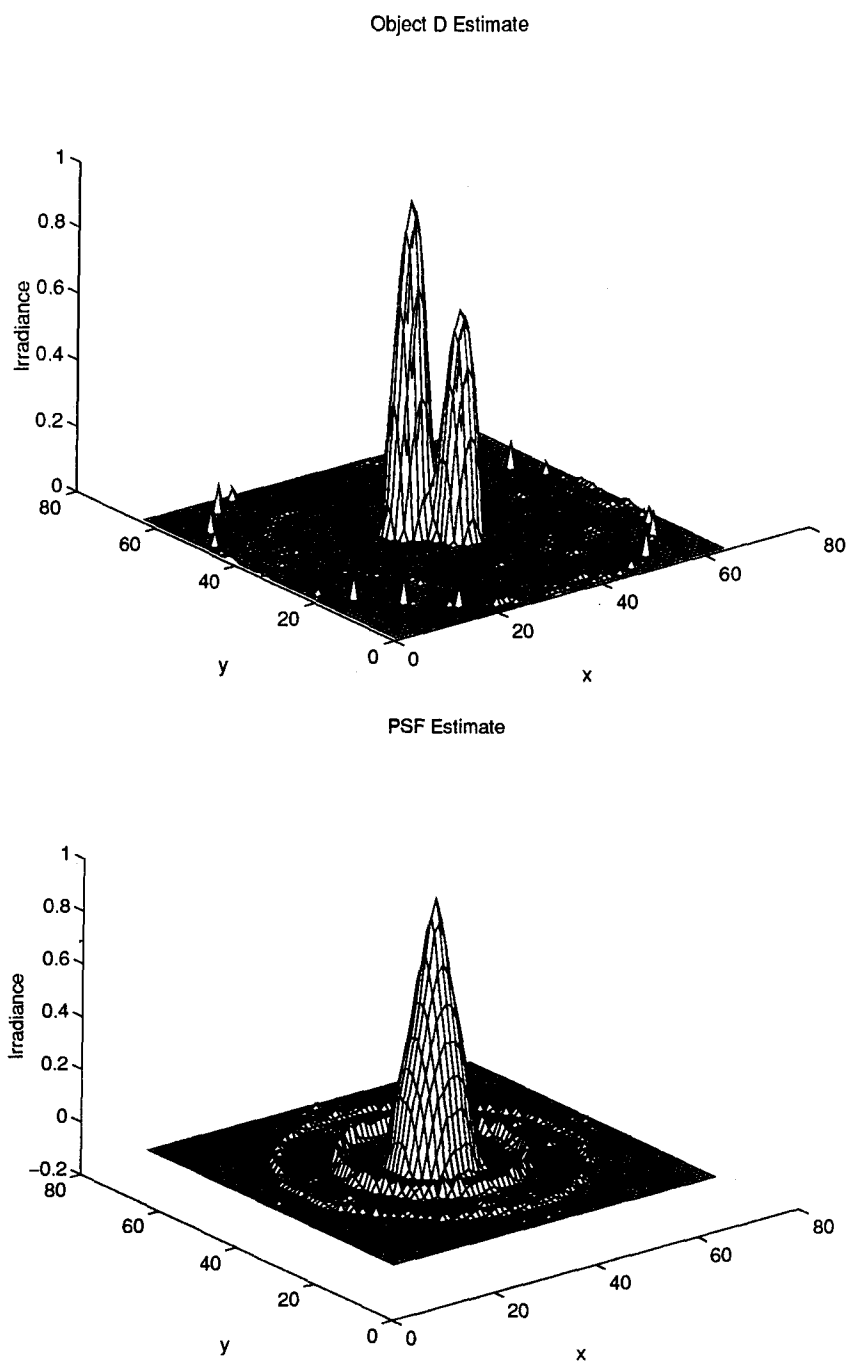


Figure C.12 Shown above are the object and PSF estimates produced by unconstrained minimization from noise-free Image D and utilizing support region 3.

Appendix D. Experiment 2 Results

The second experiment analyzes the performance of the iterative deconvolution algorithm in the presence of photon noise. The simulated photon limited images shown in Figures B.10 through B.21 are used as input measurements into the algorithm. A band-limit mask in the convolution error is compared against the basic Lane method of unconstrained minimization. Results presented in Figures D.1 through D.8 show that even with as many as 100,000 photo events, the addition of the band-limit mask greatly enhances the "reconstructability" of the algorithm. Two PSF estimates are shown in Figure D.9 which reveal the wide variation in impulse response estimation in the presence of noise. Presentation of further PSF estimates provide little insight to the ability of this algorithm to reconstruct objects from noisy blurred images, therefore, no other PSF estimates are shown. The remainder of the data presented show object estimates from images containing 10,000 and 5,000 photo events. It is clear that less light reduces the algorithm's ability to effectively reconstruct images.

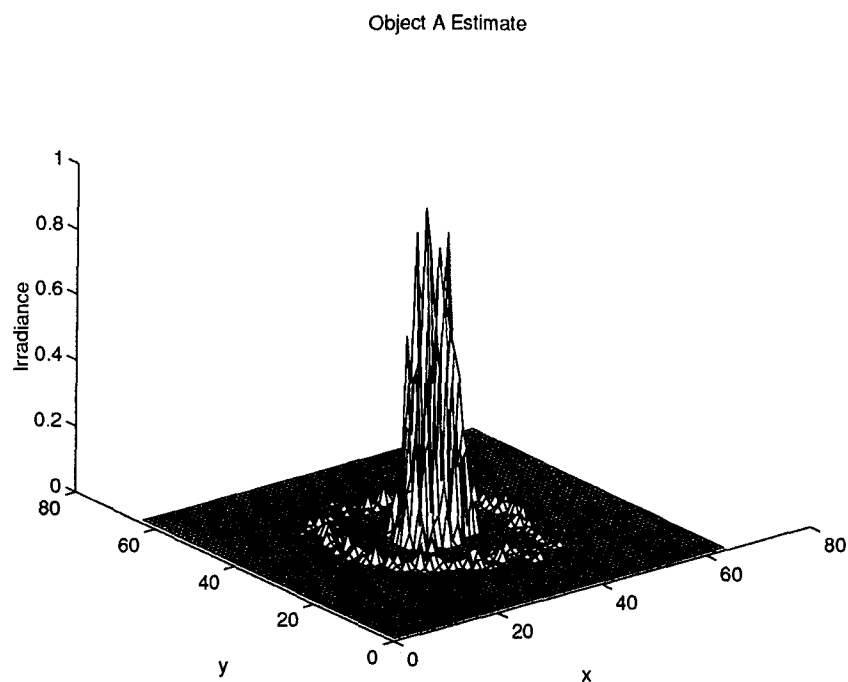


Figure D.1 The object estimate above resulted from Image A ($\bar{K} = 10^5$) using the strict Lane method for unconstrained minimization.

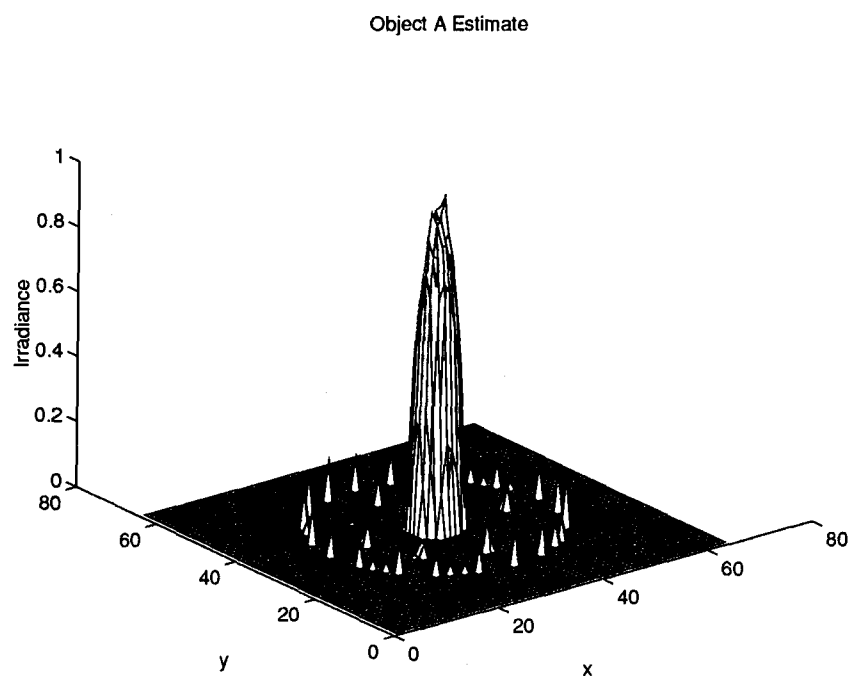


Figure D.2 The object estimate above resulted from Image A ($\bar{K} = 10^5$) using a band-limit mask in the convolution error term.

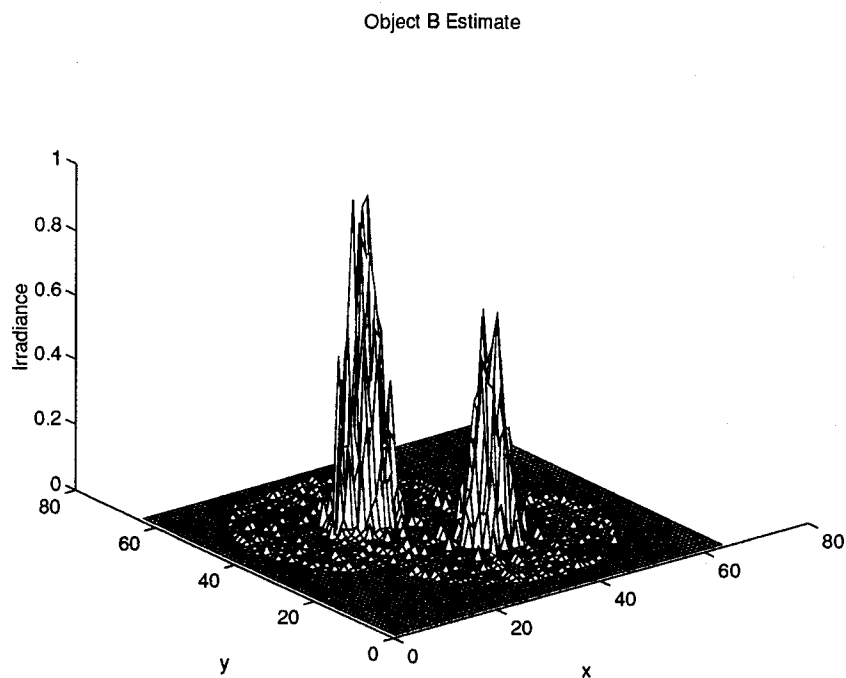


Figure D.3 The object estimate above resulted from Image B ($\bar{K} = 10^5$) using the strict Lane method for unconstrained minimization.

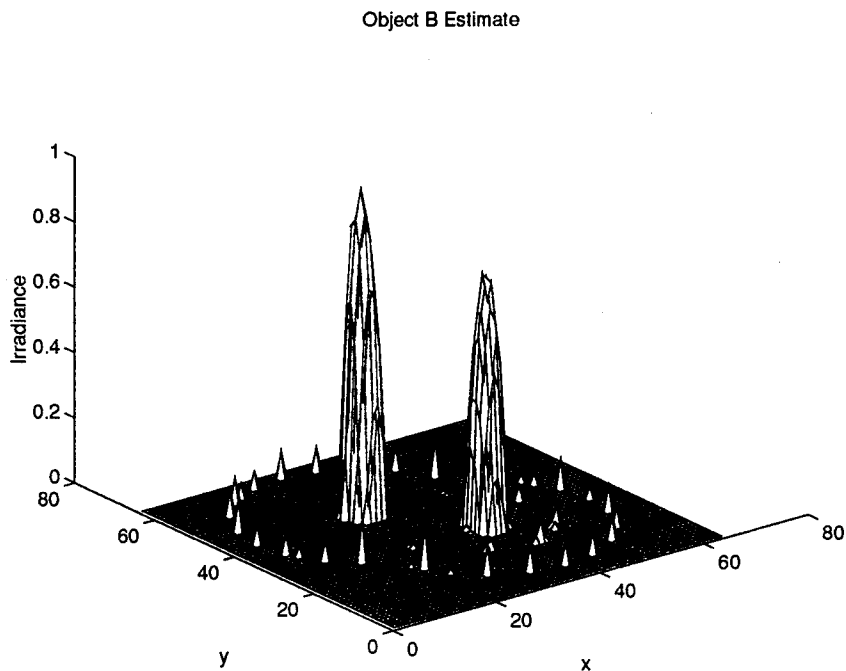


Figure D.4 The object estimate above resulted from Image B ($\bar{K} = 10^5$) using a band-limit mask in the convolution error term.

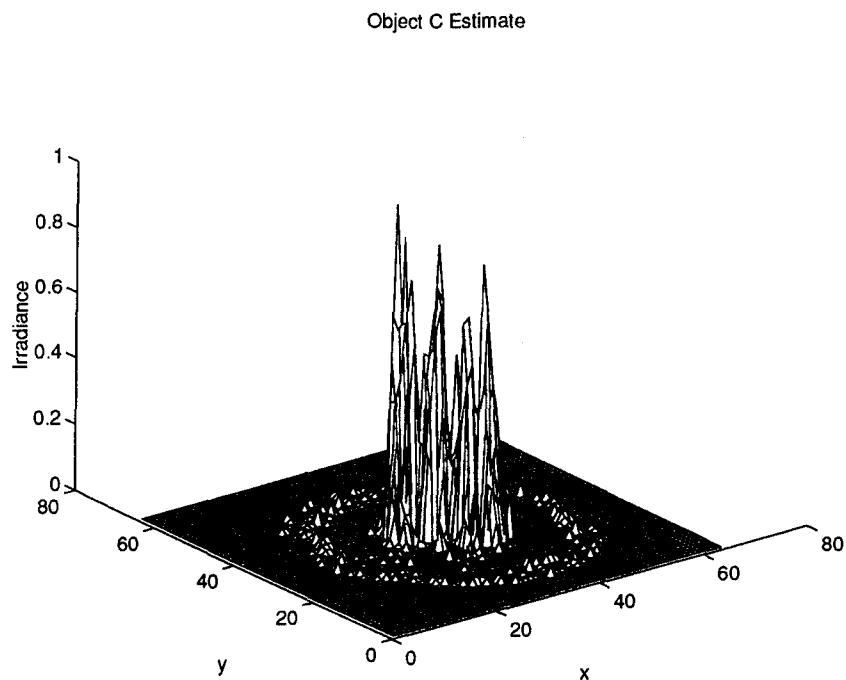


Figure D.5 The object estimate above resulted from Image C ($\bar{K} = 10^5$) using the strict Lane method for unconstrained minimization.

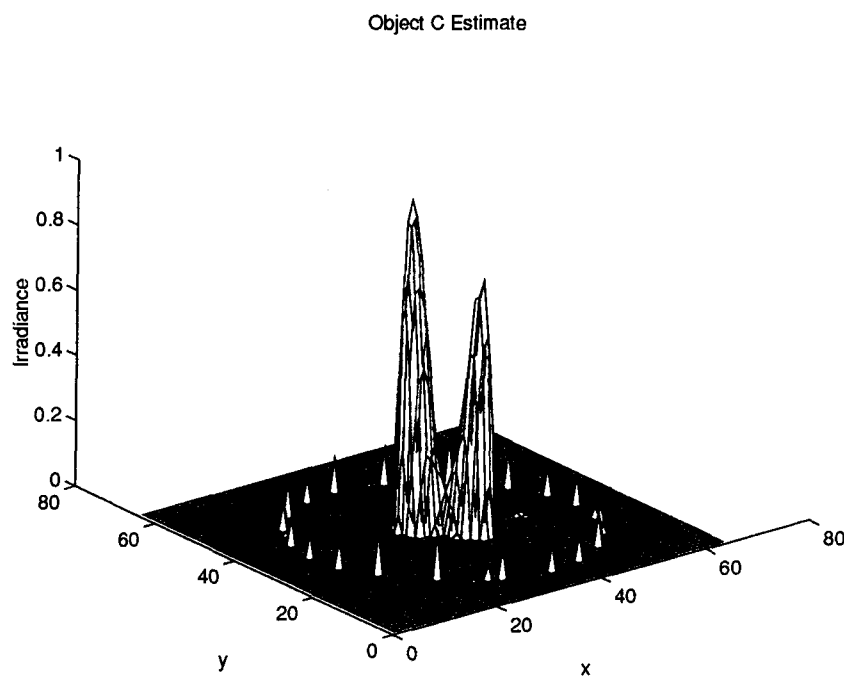


Figure D.6 The object estimate above resulted from Image C ($\bar{K} = 10^5$) using a band-limit mask in the convolution error term.

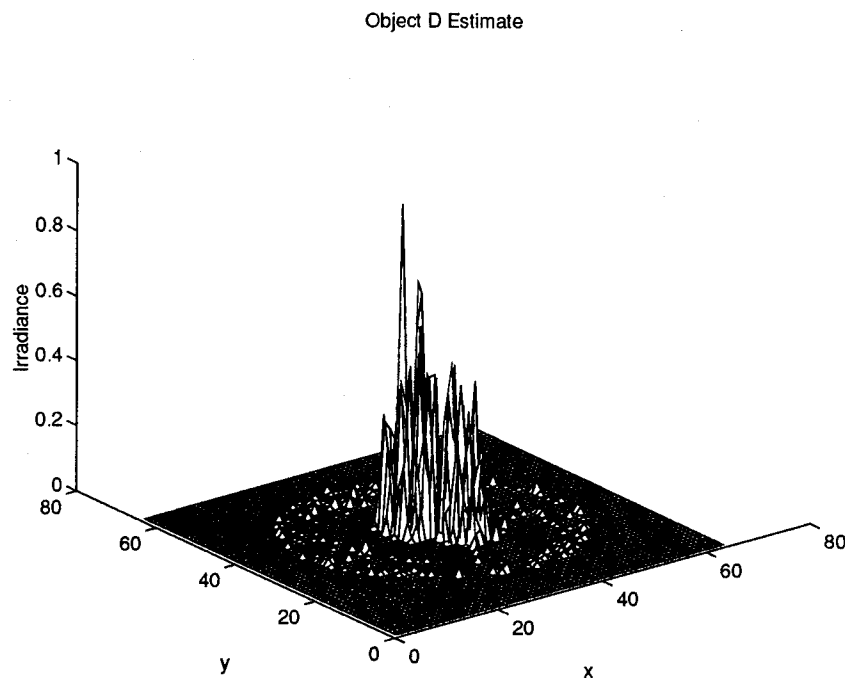


Figure D.7 The object estimate above resulted from Image D ($\bar{K} = 10^5$) using the strict Lane method for unconstrained minimization.

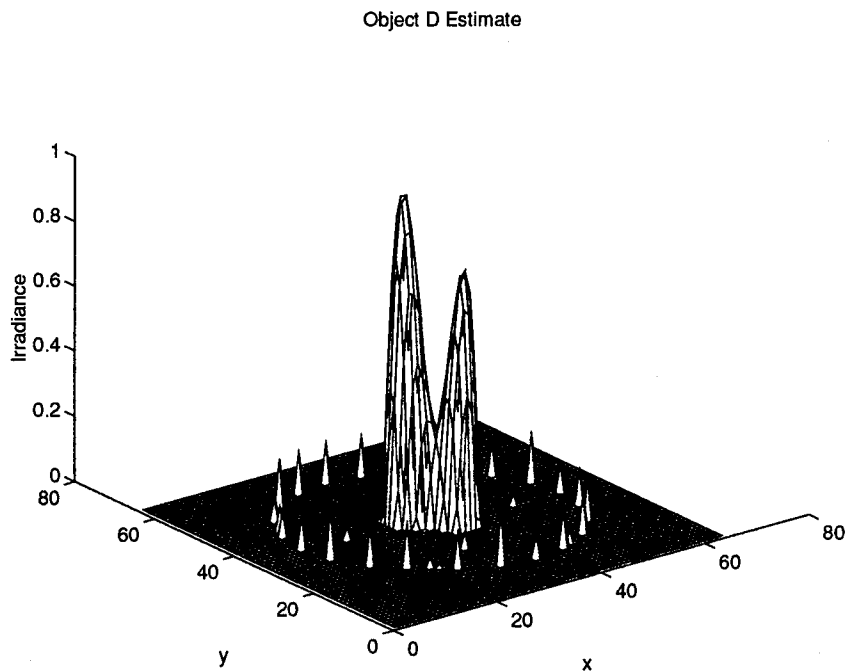


Figure D.8 The object estimate above resulted from Image D ($\bar{K} = 10^5$) using a band-limit mask in the convolution error term.

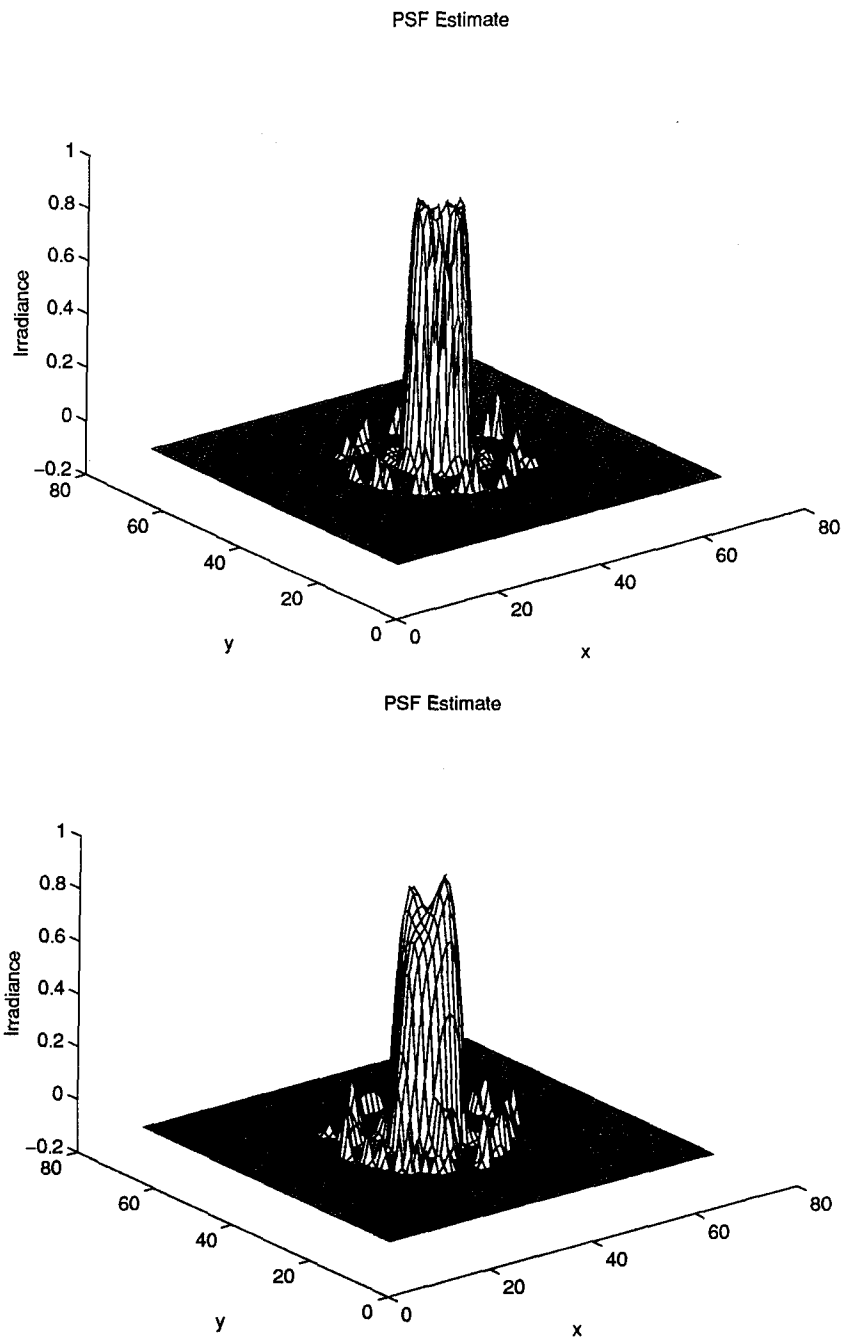


Figure D.9 The PSF estimates above resulted from Images A and D ($\bar{K} = 10^5$) using a band-limit mask in the convolution error term. These estimates reveal that the presence of noise in the measurement causes deviations in the PSF estimate from the "true" PSF. Subsequent PSF estimates are not shown.

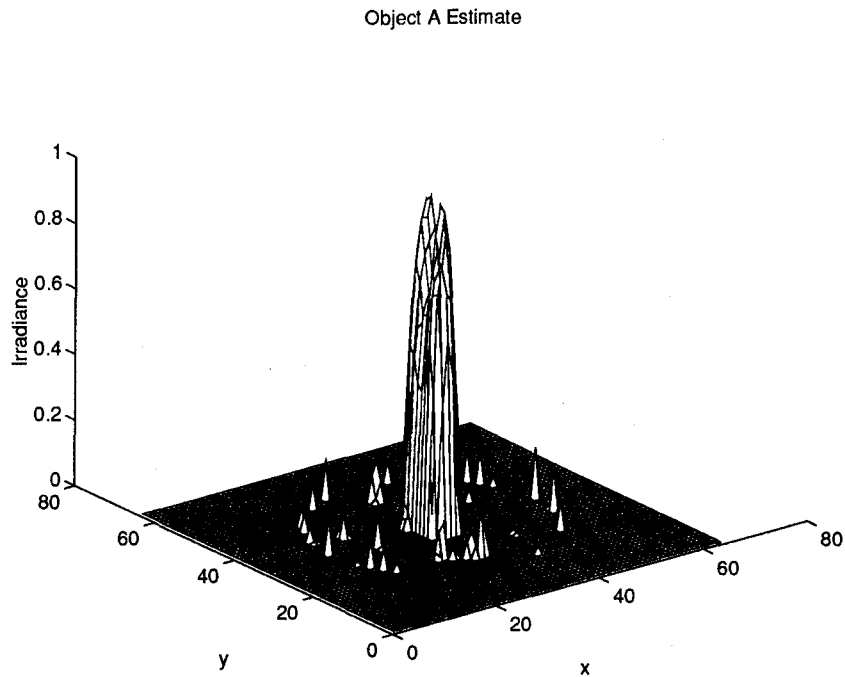


Figure D.10 The object estimate above resulted from Image A ($\bar{K} = 10^4$) using a band-limit mask in the convolution error term.

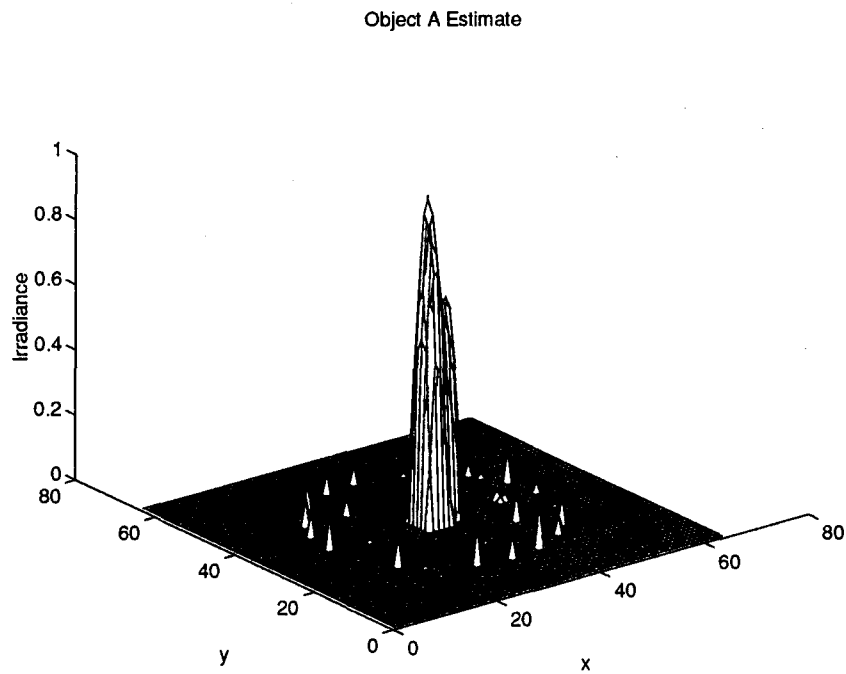


Figure D.11 The object estimate above resulted from Image A ($\bar{K} = 5,000$) using a band-limit mask in the convolution error term.

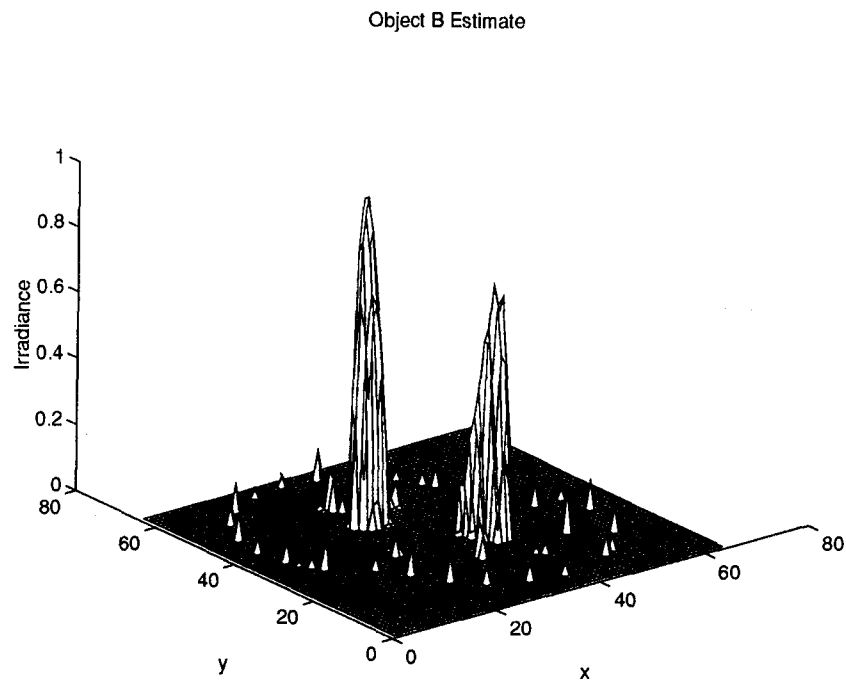


Figure D.12 The object estimate above resulted from Image B ($\bar{K} = 10^4$) using a band-limit mask in the convolution error term.

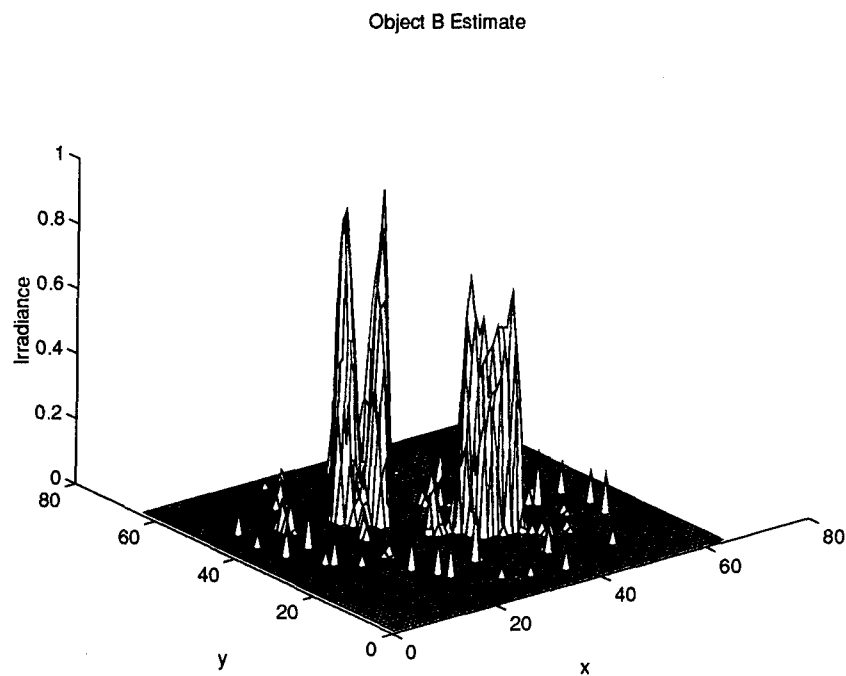


Figure D.13 The object estimate above resulted from Image B ($\bar{K} = 5,000$) using a band-limit mask in the convolution error term.

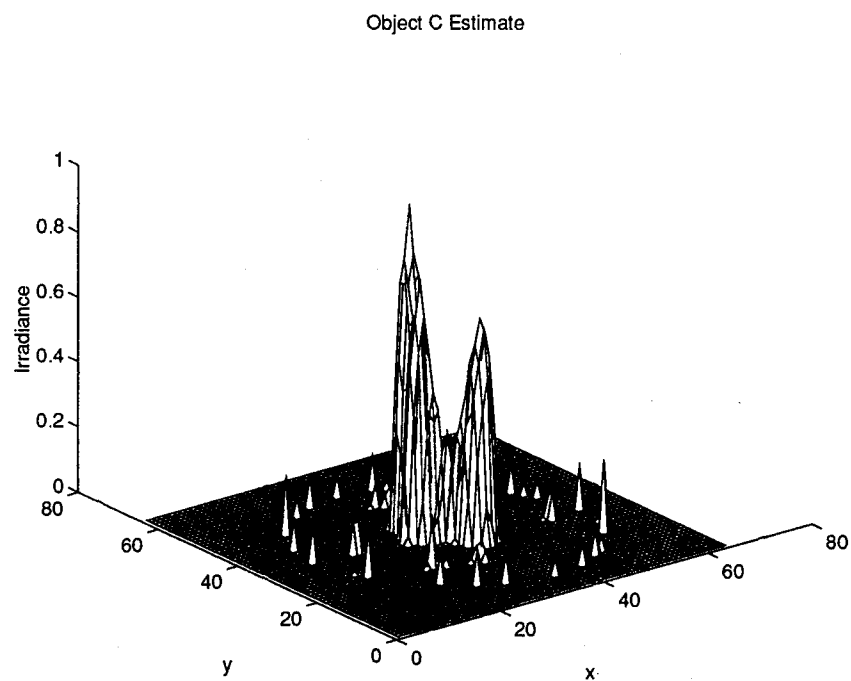


Figure D.14 The object estimate above resulted from Image C ($\bar{K} = 10^4$) using a band-limit mask in the convolution error term.

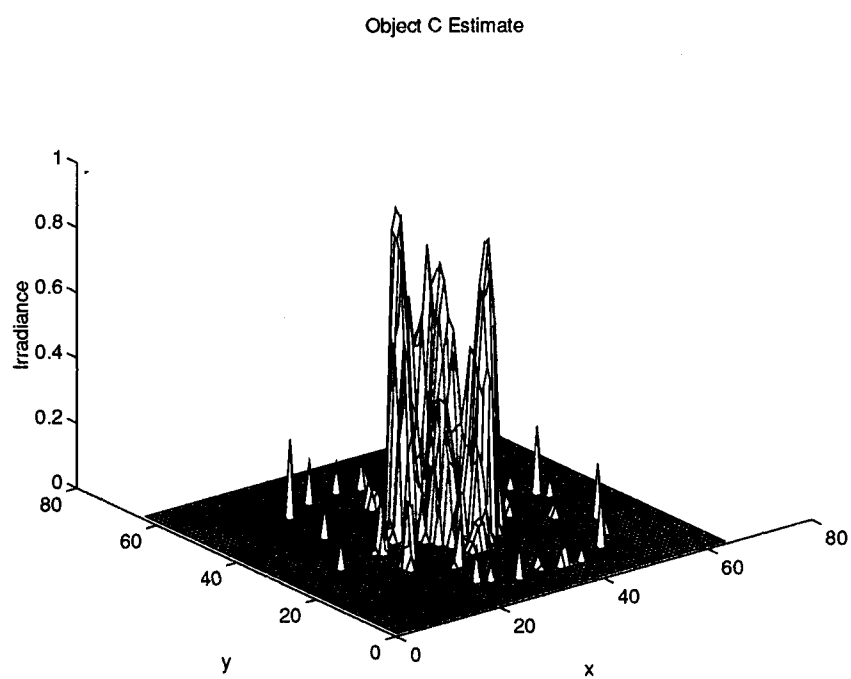


Figure D.15 The object estimate above resulted from Image C ($\bar{K} = 5,000$) using a band-limit mask in the convolution error term.

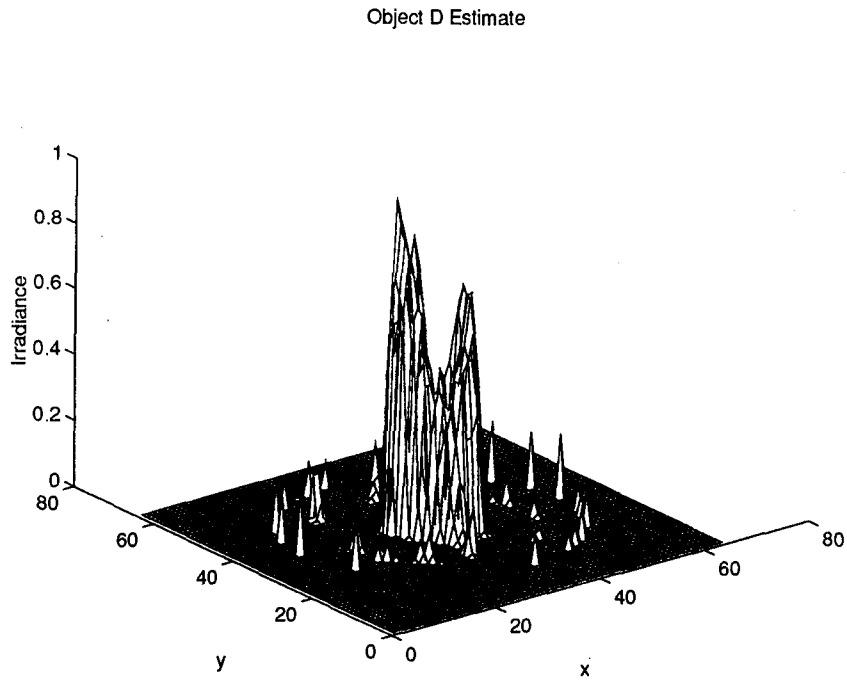


Figure D.16 The object estimate above resulted from Image D ($\bar{K} = 10^4$) using a band-limit mask in the convolution error term.

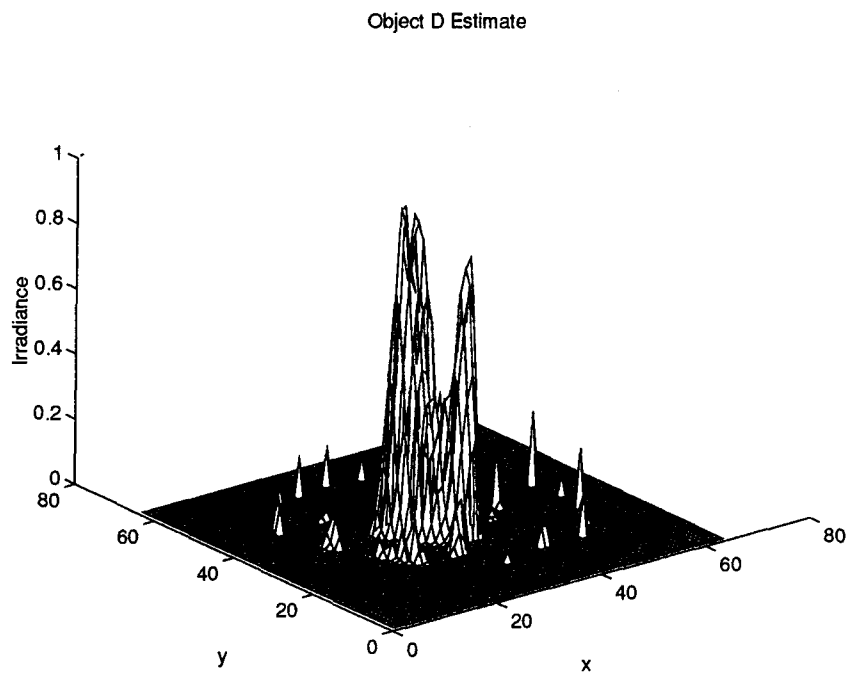


Figure D.17 The object estimate above resulted from Image D ($\bar{K} = 5,000$) using a band-limit mask in the convolution error term.

Appendix E. Experiment 3 Results

The third experiment tests the addition of a band-limit error term within the objective function for unconstrained minimization to improve the reconstruction of both noise-free and photon limited images. The band-limit error, as explained by Jeffries and Christou (12), is utilized at the start of the iterative process to prevent the trivial solution from appearing. Though no trivial solution was previously obtained with these images, this experiment attempts to determine whether the band-limit error may have a positive effect on the reconstruction process. This experiment used a fixed number of iterations (50) employing the band-limit error term, then ran the algorithm without the band-limit error term to achieve proper convergence. Mixed results appear in the following data revealing that the use of the band-limit term should be studied further.

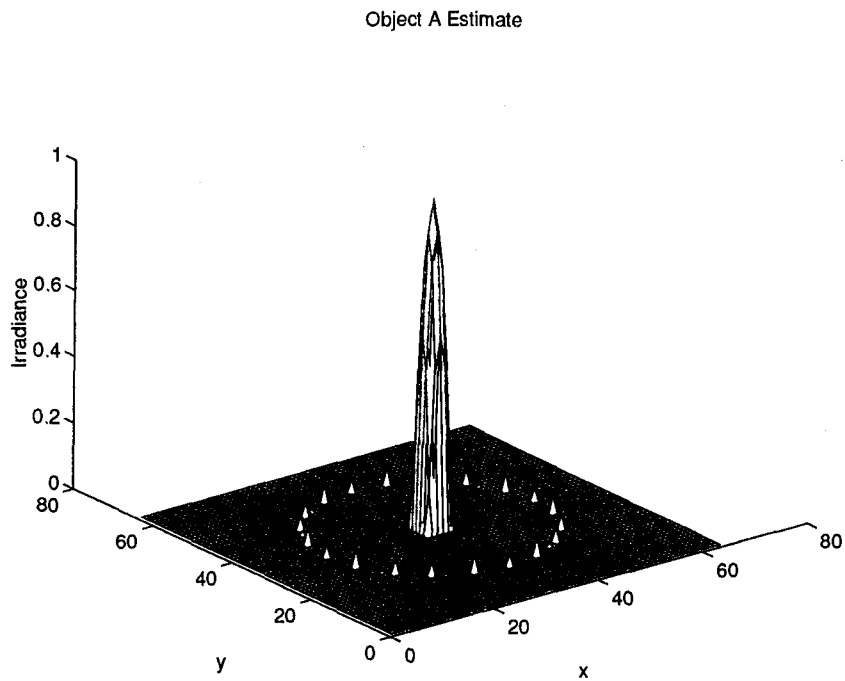


Figure E.1 The object estimate above resulted from Image A (noise-free) using a band-limit error term in the unconstrained minimization technique.

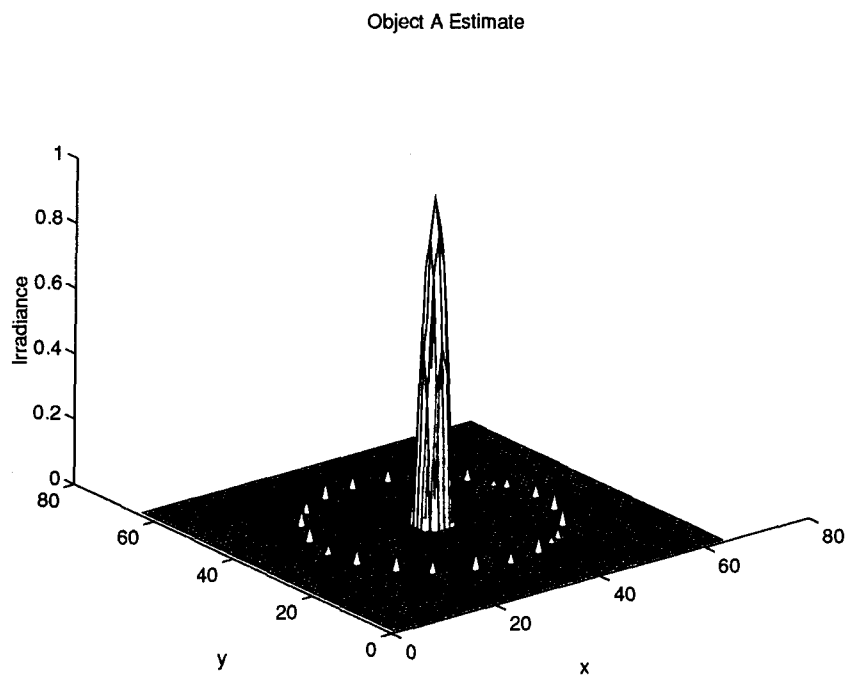


Figure E.2 The object estimate above resulted from Image A ($\bar{K} = 10^5$) using a band-limit error term in the unconstrained minimization technique.

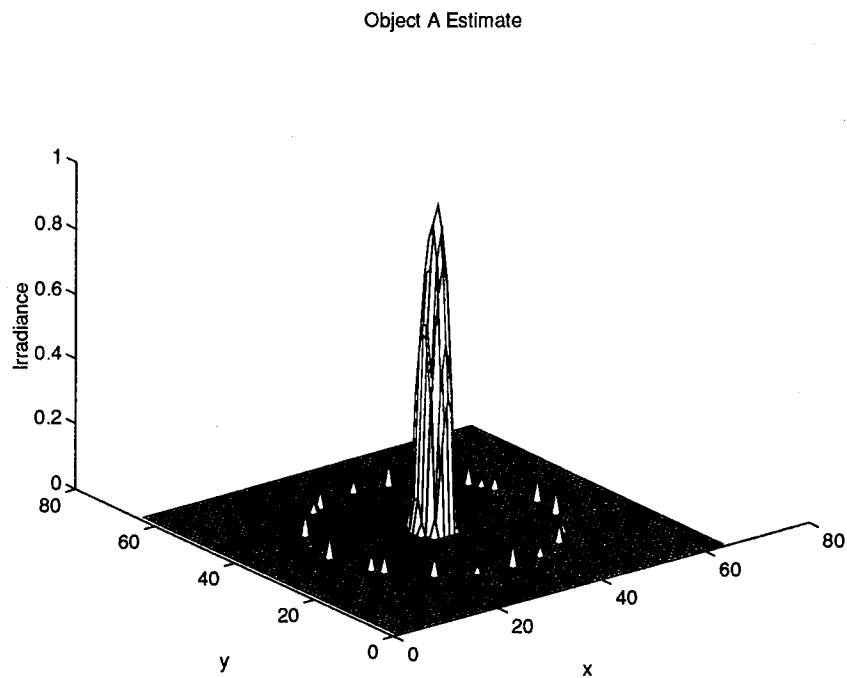


Figure E.3 The object estimate above resulted from Image A ($\bar{K} = 10^4$) using a band-limit error term in the unconstrained minimization technique.

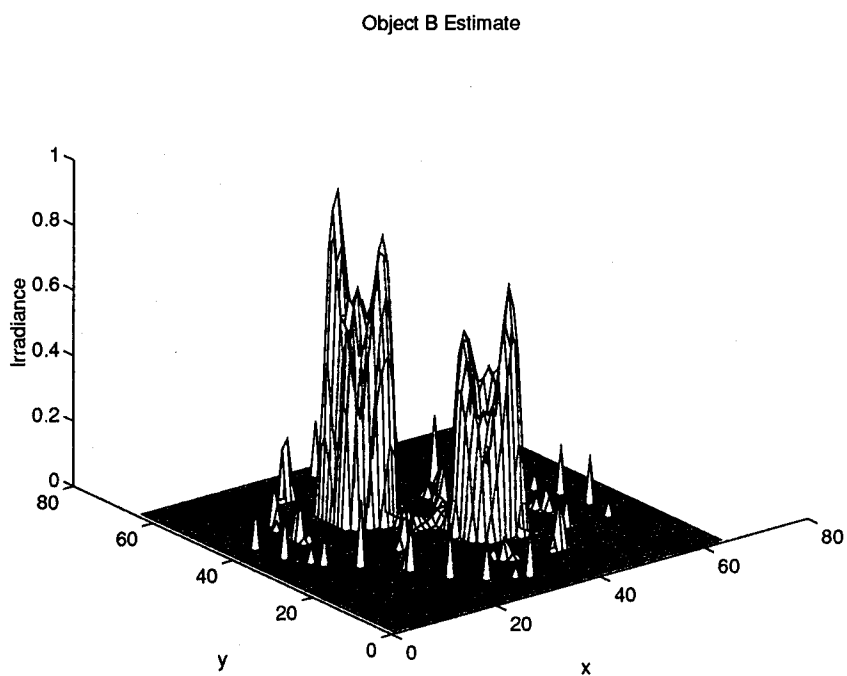


Figure E.4 The object estimate above resulted from Image B (noise-free) using a band-limit error term in the unconstrained minimization technique.

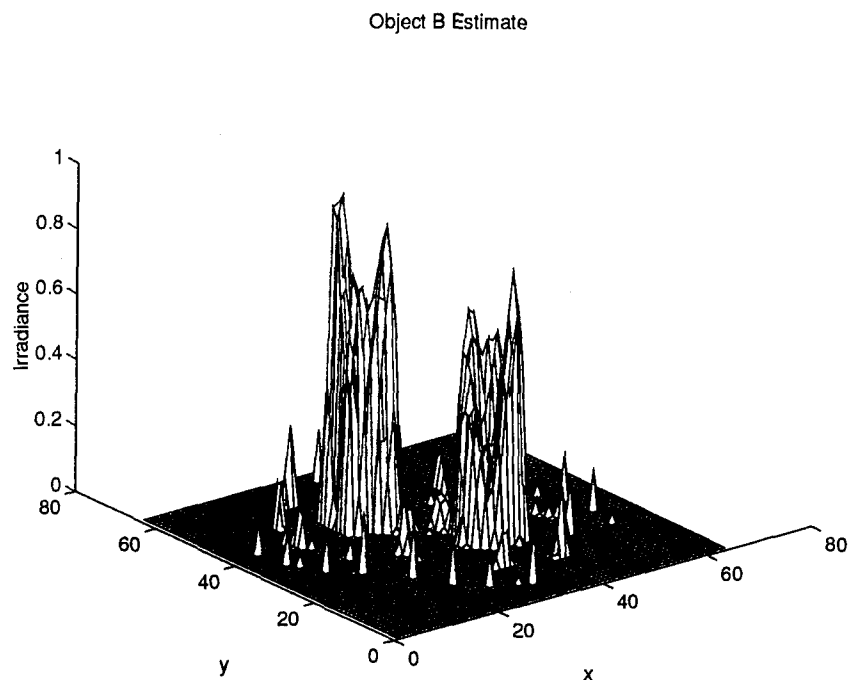


Figure E.5 The object estimate above resulted from Image B ($\bar{K} = 10^5$) using a band-limit error term in the unconstrained minimization technique.

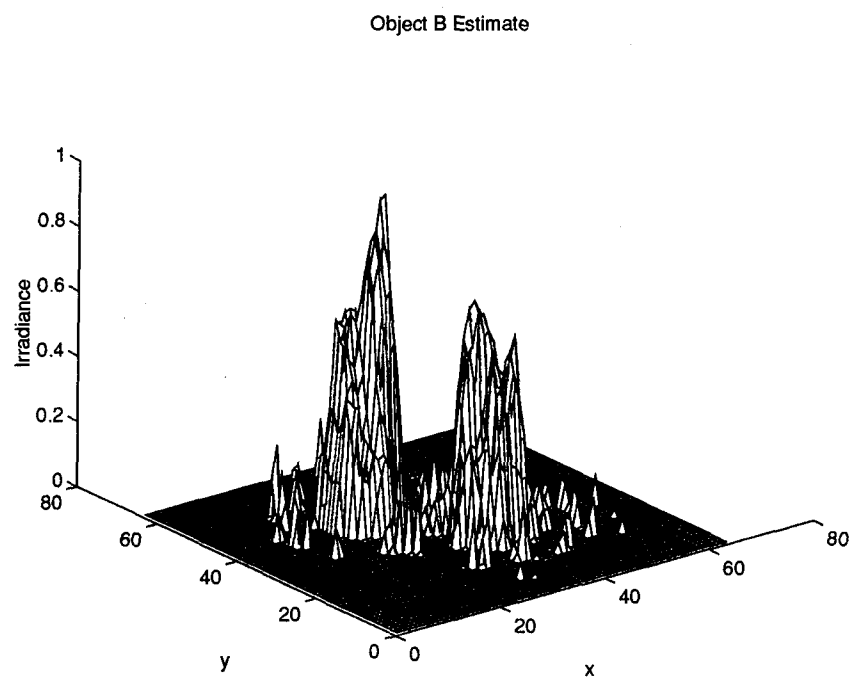


Figure E.6 The object estimate above resulted from Image B ($\bar{K} = 10^4$) using a band-limit error term in the unconstrained minimization technique.

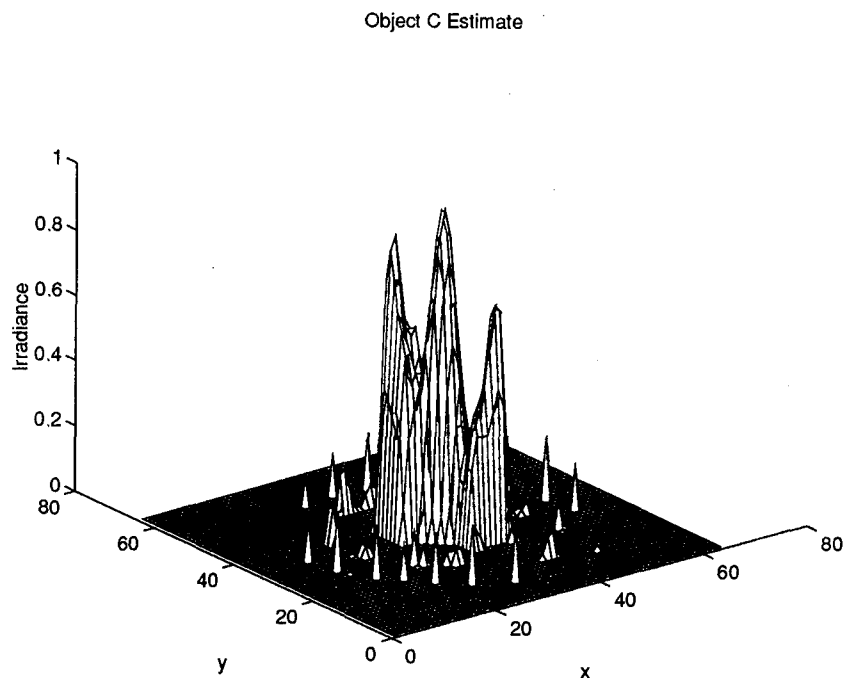


Figure E.7 The object estimate above resulted from Image C (noise-free) using a band-limit error term in the unconstrained minimization technique.

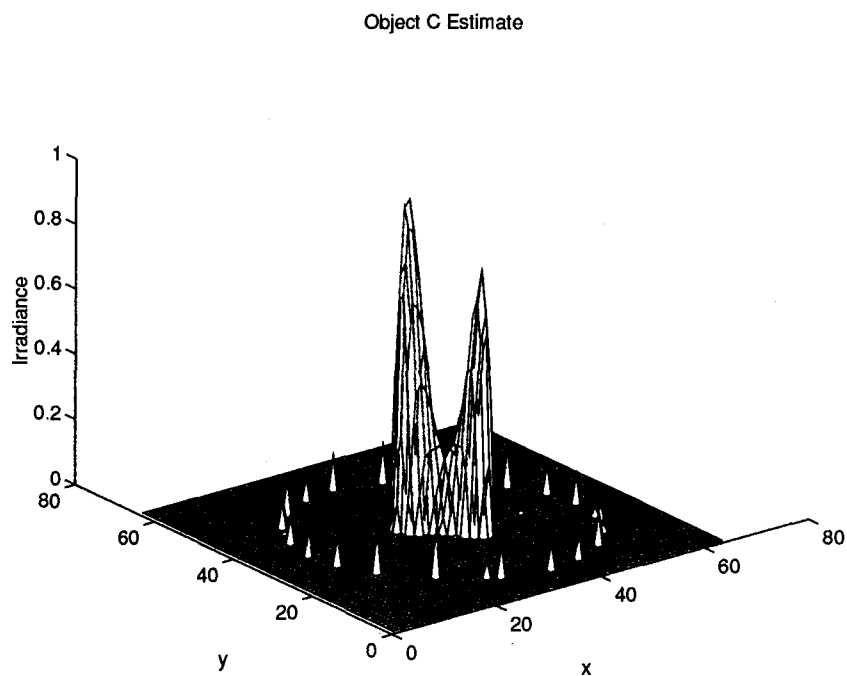


Figure E.8 The object estimate above resulted from Image C ($\bar{K} = 10^5$) using a band-limit error term in the unconstrained minimization technique.

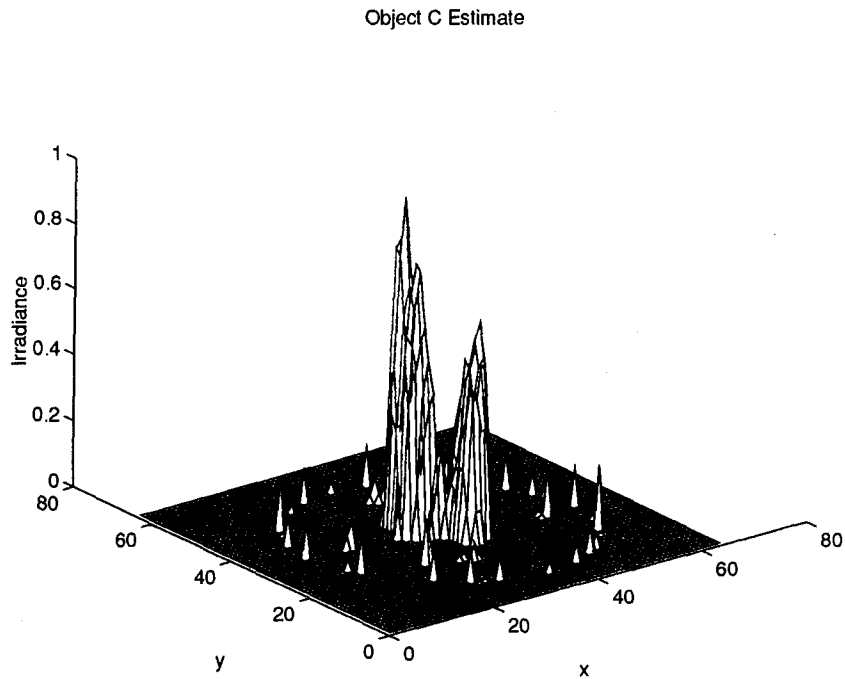


Figure E.9 The object estimate above resulted from Image C ($\bar{K} = 10^4$) using a band-limit error term in the unconstrained minimization technique.

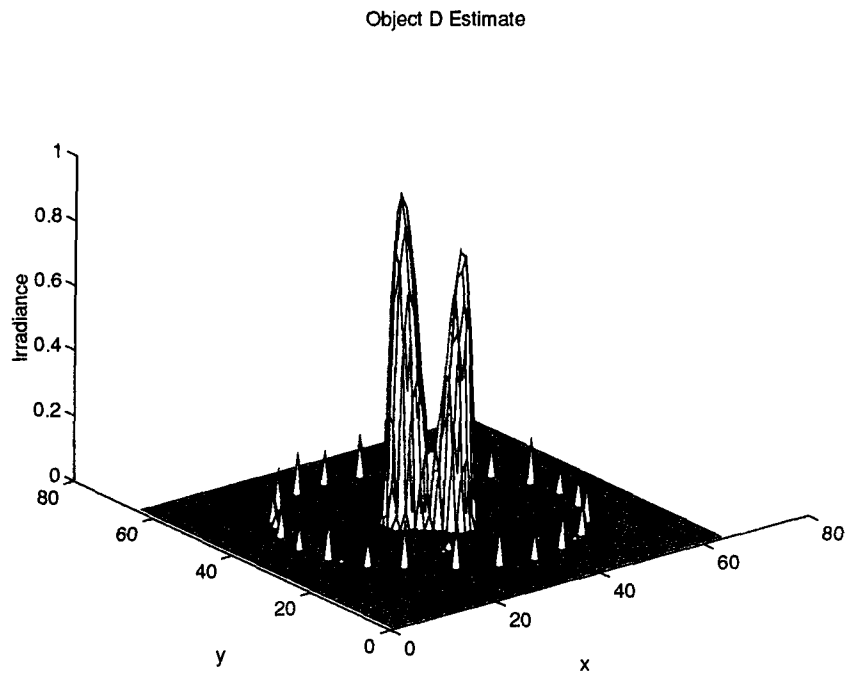


Figure E.10 The object estimate above resulted from Image D (noise-free) using a band-limit error term in the unconstrained minimization technique.

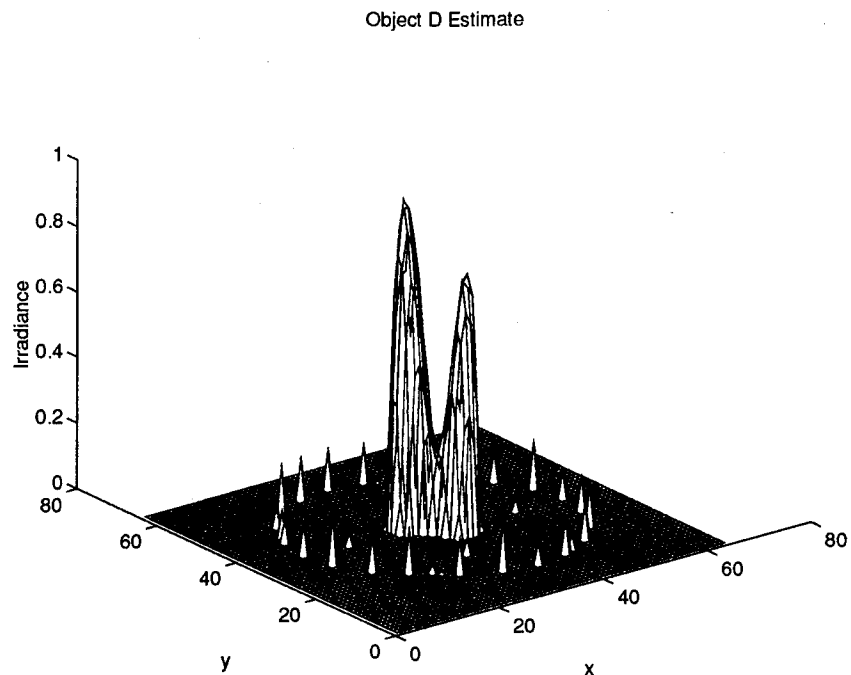


Figure E.11 The object estimate above resulted from Image D ($\bar{K} = 10^5$) using a band-limit error term in the unconstrained minimization technique.

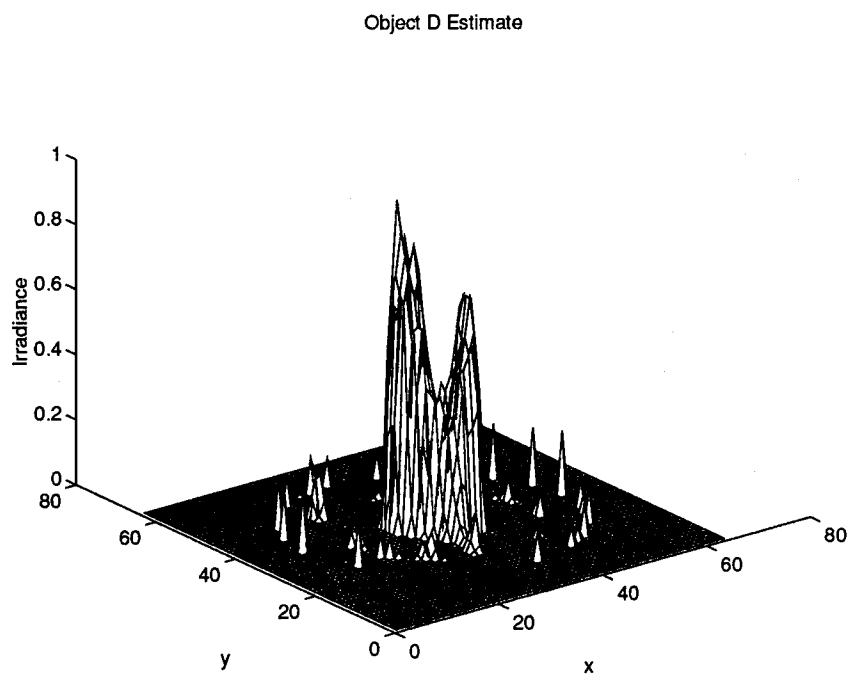


Figure E.12 The object estimate above resulted from Image D ($\bar{K} = 10^4$) using a band-limit error term in the unconstrained minimization technique.

Bibliography

1. Ayers, G. R. and J. C. Dainty. "Iterative blind deconvolution method and its applications," *Optics Letters*, 13(7):547-549 (July 1988).
2. Bates, R. H. and H. Jiang. "Blind Deconvolution - recovering the seemingly irrecoverable." *International Trends in Optics* 423-437, Academic Press, Inc., 1991.
3. Boyd, R. W. *Radiometry and the Detection of Optical Radiation*. New York: John Wiley and Sons, 1983.
4. Davey, B. L. K., R. G. Lane and R. H. Bates. "Blind deconvolution of noisy complex-valued images," *Optics Communications*, 69(5,6):353-356 (January 1989).
5. Fried, D. L. "Statistics of a geometric representation of wavefront distortion," *Journal of the Optical Society of America*, 55(11):1427-1435 (November 1965).
6. Fried, D. L. "Optical resolution through a randomly inhomogeneous medium for very long and very short exposures," *Journal of the Optical Society of America*, 56(10):1372-1379 (October 1966).
7. Goodman, J. W. *Introduction to Fourier Optics*. San Francisco, CA: McGraw-Hill, Inc., 1968.
8. Goodman, J. W. *Statistical Optics*. New York: Wiley-Interscience Publications, 1985.
9. Goodman, J. W. and J. F. Belsher. "Fundamental limitations in linear invariant restoration of atmospherically degraded images," *SPIE - Vol. 75 Imaging through the atmosphere*, 141-154 (1976).
10. Hecht, E. *Optics* (2nd Edition). Reading, MA: Addison-Wesley Publishing Co., 1987.
11. Holmes, T. J. "Blind deconvolution of quantum limited incoherent imagery: maximum-likelihood approach," *Journal of the Optical Society of America*, 9(7):1052-1061 (July 1992).
12. Jefferies, S. M. and J. C. Christou. "Restoration of astronomical images by iterative blind deconvolution," *The Astrophysical Journal*, 415:862-874 (October 1 1993).
13. Lane, R. G. "Blind deconvolution of speckle images," *Journal of the Optical Society of America*, 9(9):1508-1514 (September 1992).
14. Miura, N., S. Kuwamura, N. Baba, S. Isobe and M. Noguchi. "Parallel scheme of the iterative blind deconvolution method for stellar object reconstruction," *Applied Optics*, 32(32):6514-6520 (November 1993).

15. Muolo, M. J. *Space Handbook, A War Fighter's Guide to Space, 1*. Maxwell AFB, AL: Air University Press, 1993.
16. Newton, Isaac. *Opticks*. Dover Publications, Inc., 1952.
17. Ridpath, I. *Universe Guide to Stars and Planets*. New York: Universe Books, 1984.
18. Roddier, F. "The effects of atmospheric turbulence in optical astronomy." *Progress in Optics 19* edited by E. Wolf, North-Holland-Amsterdam, 1981.
19. Roggemann, M. C., D. W. Tyler and M. F. Bilmont. "Linear reconstruction of compensated images: theory and experimental results," *Applied Optics*, 31(35):7429-7441 (December 1992).
20. Ross, S. M. *Introduction to Probability Models* (5th Edition). Academic Press, Inc., 1993.
21. Schulz, T. J. "Multiframe blind deconvolution of astronomical images," *Journal of the Optical Society of America*, 10(5):1064-1073 (May 1993).
22. Stockham, T. G., T. M. Cannon and R. B. Ingebretson. "Blind deconvolution through digital signal processing," *Proceedings IEEE*, 63:678-692 (1975).
23. Stoudt, C. A. *Improved quality of reconstructed images through sifting of data in statistical image reconstruction*. MS thesis, Air Force Institute of Technology, 1993.

Vita

Captain Derek K. Davis was born in Texas City, Texas on December 20, 1966. In 1985, he graduated co-valedictorian of First Colonial High School in Virginia Beach, Virginia, and then attended Rensselaer Polytechnic Institute in Troy, New York from 1985 to 1989. After earning a Bachelor of Science degree in aeronautical engineering, Derek received a commission in the United States Air Force. Second Lieutenant Davis was assigned to the First Space Operations Squadron at Falcon Air Force Base, Colorado where he performed duties as a crew commander, operations training officer and deputy flight commander for Defense Meteorological Satellite Program and Defense Support Program satellites. In 1993, First Lieutenant Davis was selected to attend the Air Force Institute of Technology to pursue a Master of Science Degree in Space Operations, specializing in Optical Surveillance and Imaging. In January 1995, Captain Davis reports to the 5th Space Launch Squadron, Patrick Air Force Base, Florida, where he will serve as a Field Program Manager for Payload Operations.

Captain Davis is married to the former Elizabeth Diane Matteson of Virginia Beach, Virginia. They have two daughters Rebecca Diane and Sarah Elizabeth.

Permanent address: 7424 South Reach Drive
Fairfax Station, Virginia 22039

REPORT DOCUMENTATION PAGE			Form Approved OMB No. 0704-0188	
<small>Public reporting burden for this collection of information is estimated to average 1 hour per response, including the time for reviewing instructions, searching existing data sources, gathering and maintaining the data needed, and completing and reviewing the collection of information. Send comments regarding this burden estimate or any other aspect of this collection of information, including suggestions for reducing this burden, to Washington Headquarters Services, Directorate for Information Operations and Reports, 1215 Jefferson Davis Highway, Suite 1204, Arlington, VA 22202-4302, and to the Office of Management and Budget, Paperwork Reduction Project (0704-0188), Washington, DC 20503.</small>				
1. AGENCY USE ONLY (Leave blank)	2. REPORT DATE December 1994	3. REPORT TYPE AND DATES COVERED Master's Thesis		
4. TITLE AND SUBTITLE Effects of photon noise on unconstrained minimization techniques for iterative blind deconvolution		5. FUNDING NUMBERS		
6. AUTHOR(S) Derek K. Davis, Capt, USAF				
7. PERFORMING ORGANIZATION NAME(S) AND ADDRESS(ES) Air Force Institute of Technology, WPAFB, OH 45433-6583		8. PERFORMING ORGANIZATION REPORT NUMBER AFIT/GSO/ENP/94D-01		
9. SPONSORING/MONITORING AGENCY NAME(S) AND ADDRESS(ES) Capt Andy Suzuki PL/LIMA, 535 Lipoa Pkwy, Suite 200 Kihei, HI 96753		10. SPONSORING/MONITORING AGENCY REPORT NUMBER		
11. SUPPLEMENTARY NOTES				
12a. DISTRIBUTION/AVAILABILITY STATEMENT Approved for Public Release; Distribution Unlimited		12b. DISTRIBUTION CODE		
13. ABSTRACT (Maximum 200 words) <p style="text-align: center;">Abstract</p> <p>In recent years, imaging through atmospheric turbulence has interested military scientists seeking to improve optical surveillance of satellites. Adaptive optics was a step toward achieving diffraction-limited resolution from ground-based telescopes. Unfortunately, adaptive optics only partially compensate for atmospheric blurring, therefore post-processing of images is required. Processing methods in use today require knowledge of the impulse response of the optical system to reconstruct imagery, but this information is seldom known. This thesis looks at a new method of processing compensated imagery, called blind deconvolution, which assumes very little or no <i>a priori</i> information about the impulse response. In particular, this investigation analyzes the performance of Lane's unconstrained minimization method of blind deconvolution. This technique is applied to simulated single and binary star images corrupted by photon noise. Results reveal that prior knowledge of the cutoff frequency of the system greatly enhances the ability of the algorithm to achieve accurate estimates of the object when measurements contain relatively few photo events. Additionally, this study discovered that estimates are highly dependent upon the choice of the support region. Analysis also shows that the algorithm produces estimates containing frequency content above the diffraction-limit which may invalidate this method as a useful means to reconstruct imagery.</p>				
14. SUBJECT TERMS Image reconstruction, blind deconvolution, photon noise		15. NUMBER OF PAGES 136		
		16. PRICE CODE		
17. SECURITY CLASSIFICATION OF REPORT UNCLASSIFIED	18. SECURITY CLASSIFICATION OF THIS PAGE UNCLASSIFIED	19. SECURITY CLASSIFICATION OF ABSTRACT UNCLASSIFIED	20. LIMITATION OF ABSTRACT UL	

GENERAL INSTRUCTIONS FOR COMPLETING SF 298

The Report Documentation Page (RDP) is used in announcing and cataloging reports. It is important that this information be consistent with the rest of the report, particularly the cover and title page. Instructions for filling in each block of the form follow. It is important to *stay within the lines* to meet optical scanning requirements.

Block 1. Agency Use Only (Leave blank).

Block 2. Report Date. Full publication date including day, month, and year, if available (e.g. 1 Jan 88). Must cite at least the year.

Block 3. Type of Report and Dates Covered. State whether report is interim, final, etc. If applicable, enter inclusive report dates (e.g. 10 Jun 87 - 30 Jun 88).

Block 4. Title and Subtitle. A title is taken from the part of the report that provides the most meaningful and complete information. When a report is prepared in more than one volume, repeat the primary title, add volume number, and include subtitle for the specific volume. On classified documents enter the title classification in parentheses.

Block 5. Funding Numbers. To include contract and grant numbers; may include program element number(s), project number(s), task number(s), and work unit number(s). Use the following labels:

C - Contract	PR - Project
G - Grant	TA - Task
PE - Program Element	WU - Work Unit Accession No.

Block 6. Author(s). Name(s) of person(s) responsible for writing the report, performing the research, or credited with the content of the report. If editor or compiler, this should follow the name(s).

Block 7. Performing Organization Name(s) and Address(es). Self-explanatory.

Block 8. Performing Organization Report Number. Enter the unique alphanumeric report number(s) assigned by the organization performing the report.

Block 9. Sponsoring/Monitoring Agency Name(s) and Address(es). Self-explanatory.

Block 10. Sponsoring/Monitoring Agency Report Number. (If known)

Block 11. Supplementary Notes. Enter information not included elsewhere such as: Prepared in cooperation with...; Trans. of...; To be published in... When a report is revised, include a statement whether the new report supersedes or supplements the older report.

Block 12a. Distribution/Availability Statement. Denotes public availability or limitations. Cite any availability to the public. Enter additional limitations or special markings in all capitals (e.g. NOFORN, REL, ITAR).

DOD - See DoDD 5230.24, "Distribution Statements on Technical Documents."

DOE - See authorities.

NASA - See Handbook NHB 2200.2.

NTIS - Leave blank.

Block 12b. Distribution Code.

DOD - Leave blank.

DOE - Enter DOE distribution categories from the Standard Distribution for Unclassified Scientific and Technical Reports.

NASA - Leave blank.

NTIS - Leave blank.

Block 13. Abstract. Include a brief (*Maximum 200 words*) factual summary of the most significant information contained in the report.

Block 14. Subject Terms. Keywords or phrases identifying major subjects in the report.

Block 15. Number of Pages. Enter the total number of pages.

Block 16. Price Code. Enter appropriate price code (*NTIS only*).

Blocks 17. - 19. Security Classifications. Self-explanatory. Enter U.S. Security Classification in accordance with U.S. Security Regulations (i.e., UNCLASSIFIED). If form contains classified information, stamp classification on the top and bottom of the page.

Block 20. Limitation of Abstract. This block must be completed to assign a limitation to the abstract. Enter either UL (unlimited) or SAR (same as report). An entry in this block is necessary if the abstract is to be limited. If blank, the abstract is assumed to be unlimited.